TTMP vol 2 (3), 2025
doi: 10.30511/TTMP.2025.2064964.1056

Transactions in Theoretical
and Mathematical Physics

Numerical Study of a Nanoscale Waveguide with Brillouin Scattering

Maryam Zoghi *

School of Engineering Science, College of Engineering, 16 Azar Street, Tehran, Iran

Received: 07 July 2025 / Accepted: 09 July 2025 / Published: 09 July 2025

Abstract Stimulated Brillouin scattering (SBS) arises from the interaction between light and sound waves. In partially suspended waveguides, reduced substrate contact enhances optical and acoustic confinement, improving SBS efficiency. This study uses two-dimensional finite element simulations to analyze SBS in a silicon waveguide anchored by a silica pillar. Both forward and backward SBS are explored across a broad frequency range. Optimizing the pillar width significantly increases SBS gain, mainly through the photoelastic effect, with minor moving boundary contributions. The results emphasize the importance of structural design in enhancing SBS for high-performance integrated photonic applications.

1 Introduction

Stimulated Brillouin scattering (SBS) is a nonlinear phenomenon in which light coherently interacts with acoustic vibrations within an optically transparent medium [1]. This process was predicted by Brillouin in 1922 [2] and was first experimentally verified shortly after the advent of the laser [3]. While SBS was initially regarded as a detrimental effect in optical fiber systems [4], its applications are increasingly recognized in narrow line-width lasers [5,6], microwave photonics filters [7,8], non-reciprocal components [9,10], light storage [11,12], and optical gyroscopes [13]. At elevated optical intensities, the interference pattern formed between two optical waves (referred to as the 'pump' and the 'Stokes seed', which are initially induced by thermal phonons) produces sound, which in turn creates a travelling index grating that scatters light. This phenomenon induces a back-action drive of the mechanical waves through electrostriction and radiation pressure forces [1]. Such feedback results in the so-called backward Stimulated Brillouin Scattering (SBS) effect (Fig. 1).

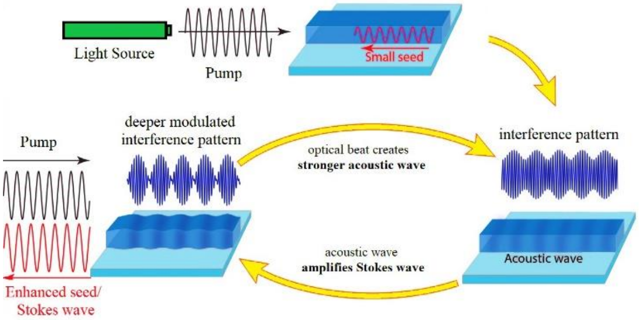

Fig. 1 Stimulated Brillouin scattering.

Over the past decade, thanks to the development and accessibility of sophisticated top-down nanofabrication tools, significant research advances have been made in this field, both in classical [14] and quantum [15] contexts. The progress made on these integrated-photonic structures led to a merging of traditional waveguide-based Brillouin concepts with those of cavity optomechanics. A notable result of this integration was the prediction and later demonstration of Brillouin scattering with giant gain in a Complementary Metal-Oxide-Semiconductor (CMOS)-compatible platform [16]. The suspended rectangular silicon waveguide structure exemplifies a particular kind of waveguide design that is preferred in the field of nanophotonics due to its ability to provide optical confinement and enable low-loss propagation. In this research, we investigate SBS within a rectangular suspended waveguide composed of silicon on an etched silica substrate using numerical modelling.

2 Physics of Brillouin Scattering

---

* e-mail: maryam.zoghi@ut.ac.ir

Given that the refractive index of the waveguide exceeds that of the surrounding material, this configuration will facilitate confined optical modes characterized by a specific angular frequency ω and wave number k. The determination of these modes, along with their corresponding modal fields, can be achieved through various numerical techniques, all of which address Maxwell's equations on the cross-section while applying suitable boundary conditions at the periphery of the computational domain.

2.1 Optical Mode Equations

We begin with Maxwell's equations:

$$\nabla \times \boldsymbol{E} = -\partial_t \boldsymbol{B}, \tag{1}$$

$$\nabla \times \boldsymbol{H} = \partial_t \boldsymbol{D} + \boldsymbol{J}, \tag{2}$$

where $\boldsymbol{D}$ and $\boldsymbol{B}$ are the electric and magnetic induction fields, respectively; $\boldsymbol{E}$ and $\boldsymbol{H}$ denote the electric and magnetic fields, respectively; $\boldsymbol{J}$ signifies the dissipative current resulting from ohmic losses, and ∇ indicates the three-dimensional del operator. The symbol ∂_t represents the partial derivative with respect to time. By introducing the constitutive expansions $\boldsymbol{B} = \mu \boldsymbol{H}$, $\boldsymbol{D} = \varepsilon \boldsymbol{E} + \boldsymbol{P}^{NL}$, and $\boldsymbol{J} = \sigma \boldsymbol{E}$, and $\boldsymbol{P}^{NL}(= \Delta\varepsilon\ \boldsymbol{E}$, assuming no nonlinear magnetic effects, with $\Delta\varepsilon$ as the perturbation), signifies the nonlinear polarization field, and $\varepsilon(= \varepsilon^R - i\sigma\omega)$, σ, and μ denote the permittivity, ohmic conductance, and permeability of the medium, respectively. If we define $|\Psi\rangle = \binom{\boldsymbol{E}}{\boldsymbol{H}}$, with the expansion as

$$|\Psi(x,y,z,t)\rangle = a_n \exp i(k_n z - \omega_n t)\ |\Psi_n(x,y)\rangle + c.c. \tag{3}$$

The transverse optical modes can then be derived from vector Helmholtz equation [17]:

$$(\mathbb{D}^{op} + ik_n \mathbb{P}^{op})|\Psi_n\rangle = i\ \omega_n\ \mathbb{E}^{op}\ |\Psi_n\rangle. \tag{4}$$

With

$$\mathbb{E}^{op} = \begin{pmatrix} \varepsilon^R & 0 \\ 0 & \mu \end{pmatrix}, \tag{5.a}$$

$$\Delta\mathbb{E}^{op} = \begin{pmatrix} \Delta\varepsilon & 0 \\ 0 & 0 \end{pmatrix}, \tag{5.b}$$

$$\mathbb{P}^{op} = \begin{pmatrix} 0 & -\hat{\boldsymbol{z}} \times \\ \hat{\boldsymbol{z}} \times & \mu \end{pmatrix}, \tag{5.c}$$

$$\mathbb{D}^{op} = \begin{pmatrix} 0 & -\nabla_\perp \times \\ \nabla_\perp \times & 0 \end{pmatrix}, \tag{5.d}$$

where $\nabla = \nabla_\perp + \hat{\boldsymbol{z}}\,\partial_z$ and $\hat{\boldsymbol{z}} = (0,0,1)$.

2.2 Acoustic Mode Equation

The mechanical counterpart to Maxwell's equations is represented by the equations of linear elasticity, which encompass the relationship between strain and mechanical displacement, as well as the principle of momentum conservation. Assuming that the acoustic losses are weak, we have:

$$\boldsymbol{S} = \nabla_s \mathbf{U}, \tag{6}$$

$$\rho\ \partial_t^2 \mathbf{U} = \nabla . \mathbf{T}\ , \tag{7}$$

where $\boldsymbol{S}$ represents the linear strain tensor, ∇_s signifies the symmetric gradient operator, $\mathbf{U}$ denotes the infinitesimal mechanical displacement vector, ρ indicates the mass density, and $\mathbf{T}$ refers to the stress tensor (Cauchy stress), which in the absence of loss assumes the following form

$$\mathrm{T}_{ij} = c_{ijkl}\, S_{kl}\ , \quad \text{or} \qquad \boldsymbol{T} = \boldsymbol{c} \!:\! \boldsymbol{S}\ . \tag{8}$$

In this context, we define the fourth-rank sffness tensor c_{ijkl} that characterizes the elastic material properties of the waveguide, and we introduce '**:**' as a shorthand notation for a double index contraction.

Fundamental acoustic equation of (7) can be rewritten as:

$$\rho\ \partial_t^2 \mathrm{U}_i = \sum_{jkl} \partial_j c_{ijkl}\ \partial_k \mathrm{U}_l\ . \tag{9}$$

Here, ∂_j denotes the spatial derivative in the j-th spatial direction along j, where $j \in \{x,y,z\}$.

In a manner similar to the optical scenario, we now present a notation for the acoustic state vector$|\phi\rangle = \binom{\boldsymbol{T}}{\boldsymbol{V}}$, where $\boldsymbol{V} = \partial_t \boldsymbol{U}$ is the local velocity field. We proceed to approximate the acoustic state based on the eigenmodes of the (lossless, devoid of any external forces) acoustic waveguide [17]:

$$(\mathbb{D}^{ac} + iq\mathbb{P}^{ac})|\Phi\rangle = i\ \Omega\ \mathbb{E}^{ac}\ |\Phi\rangle, \tag{10}$$

Where

Table 1 Optical and acoustic properties of the waveguide materials [19]

Material	**Relative permittivity**	**Photoelastic coefficients**			**Stiffness constants**			**Density**
	ε_r	P11	P12	P44	C11[Pa]	C12[Pa]	C44[Pa]	ρ[kgm^{-3}]
Si	12.25	-0.09	0.017	-0.051	2.17×10^{11}	4.83×10^{10}	6.71×10^{10}	2329
SiO$_2$	2.25	0.121	0.27	-0.075	7.85×10^{10}	1.61×10^{10}	3.12×10^{10}	2201

$$\mathbb{E}^{ac} = \begin{pmatrix} \boldsymbol{s}\colon & 0 \\ 0 & \rho \end{pmatrix}, \tag{11.a}$$

$$\mathbb{P}^{ac} = \begin{pmatrix} 0 & -\hat{\boldsymbol{z}}\otimes_s \\ -\hat{\boldsymbol{z}}. & 0 \end{pmatrix}, \tag{11.b}$$

$$\mathbb{D}^{ac} = \begin{pmatrix} 0 & -\boldsymbol{\nabla}_{\perp,s} \\ -\boldsymbol{\nabla}_{\perp}. & 0 \end{pmatrix}. \tag{11.c}$$

Here, we define the symmetrized tensor product $\otimes_s$ by $\hat{\boldsymbol{z}}\otimes_s\boldsymbol{V} = (\hat{\boldsymbol{z}}\otimes\mathbf{V} + \mathbf{V}\otimes\hat{\boldsymbol{z}})/2$. The nonlinear optomechanical processes that dominate Brillouin scattering constitute inelastic scattering processes between two photons and one phonon. As a result, we will include only a single acoustic mode, leading to the following expansion:

$$|\phi(x,y,z,t)\rangle = b(z,t)\exp i(qz-\Omega t)\,|\Phi(x,y)\rangle + c.c. \tag{12}$$

2.3 Gain Calculation

In SBS, a three-wave interaction takes place, resulting in spatially stimulated optical gain. The geometry under consideration is that of a z-invariant waveguide, which can supp ort both optical and acoustic waveguide modes. For the guided opto-mechanical modes, the pump (p) and Stokes (s) waves, as well as the elastic wave, are taken to be of the form [18]:

$$\boldsymbol{E}_p(\boldsymbol{r},t) = a_p(z,t)\boldsymbol{e}_p(x,y)\exp i\big(k_pz-\omega_pt\big) + c.c. \tag{13}$$

$$\boldsymbol{E}_s(\boldsymbol{r},t) = a_s(z,t)\boldsymbol{e}_s(x,y)\exp i(k_sz-\omega_st) + c.c. \tag{14}$$

$$\boldsymbol{U}(\boldsymbol{r},t) = b(z,t)\boldsymbol{u}(x,y)\;exp\;i(qz-\Omega t) + c.c. \tag{15}$$

where optical angular frequency and wave vector, ω_i and k_i $(i = p,s)$ and the acoustic frequency and wave vector, Ω and q, are related in the conventional manner concerning their propagation velocities. As a result of the conservation of energy and momentum, the subsequent relationships between frequency and wave vectors must be fulfilled: $\Omega = \omega_p - \omega_s$ and $q = k_p - k_s$.

Utilizing the slowly varying envelope approximation on the longitudinal aspect of the governing equations results in the subsequent coupled equations for the envelopes [18]:

$$\left(v_p\partial_z + \partial_t + \frac{v_p\alpha_p}{2}\right)a_p = -ig_0a_sb, \tag{16}$$

$$\left(\pm v_s\partial_z + \partial_t + \frac{v_s\alpha_s}{2}\right)a_s = -ig_0{}^*a_pb^*, \tag{17}$$

$$\left(v_m\partial_z + \partial_t + \left(i\Delta_m + \frac{\gamma_m}{2}\right)\right)B = -ig_0{}^*a_s{}^*a_p, \tag{18}$$

where $v_{p,s,m}$ represent the pump, Stokes, and mechanical group velocities, the upper and lower signs in the ± symbols in Eq. (16) account for either *forward* (upper sign) or *backward* (lower sign) SBS, $\alpha_{p,s}$ are the optical power attenuation coefficient, $\Delta_m = \Omega - \Omega_m$ is the frequency mismatch between the pump-Stokes beating and acoustic mode, $\gamma_m = \frac{\Omega_m}{Q_m}$ is the mechanical energy damping rate of a mode with quality factor Q_m. g_0 is the waveguide optomechanical

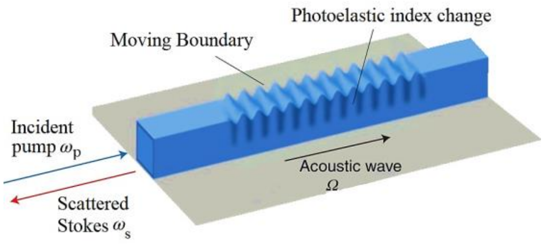

Fig. 2 Schematic of photoelastic and moving boundary effects.

coupling constant, which is calculated by integrating the interaction energy between the optical and mechanical modes over the waveguide's cross-sectional area, taking into account the radiation pressure and electrostriction interaction mechanisms.

The mechanical deformation influences the electromagnetic field in two distinct manners. Firstly, it alters the permittivity value, a phenomenon referred to as the *photoelastic* (PE) effect. Secondly, the displacement of material boundaries exerts work on the fields, an effect that lacks a widely recognized name, which we designate as *moving boundary* (MB) scattering (Fig. 2). In subwavelength waveguides, these two physical parameters are significant in the context of Brillouin gain. The first parameter is Q_{PE}, which can be articulated through a surface integral, whereas the second is Q_{MB}, which serves as a counteraction to radiation pressure [20]:

$$Q_{PE} = -\varepsilon_0 n^4 \boldsymbol{P}:\boldsymbol{S}\ \frac{\int dA\left(\boldsymbol{E}_p{}^* \cdot \boldsymbol{E}_s\right)}{\max(|\boldsymbol{u}|)\, N_p N_s}, \tag{19}$$

$$Q_{MB} = \frac{\int (\boldsymbol{u}^* \cdot \hat{\boldsymbol{n}}) dr\ \left[\delta\varepsilon_{MB}\, \boldsymbol{E}^*{}_{p,\parallel} \cdot \boldsymbol{E}_{s,\parallel} - \delta\varepsilon_{MB}{}^{-1}\, \boldsymbol{D}^*{}_{p,\perp} \cdot \boldsymbol{D}_{s,\perp}\right]}{\max(|\boldsymbol{u}|) N_p N_s}. \tag{20}$$

In the above, $\boldsymbol{P}$ represents the fourth rank photoelastic tensor. The variable n signifies the material refractive index, and $\delta\varepsilon_{MB}$ is defined as $(\varepsilon_{core} - \varepsilon_{clad})$. Additionally, $\delta\varepsilon_{MB}{}^{-1}$ is expressed as $(\frac{1}{\varepsilon_{core}} - \frac{1}{\varepsilon_{clad}})$ in which $\varepsilon_{core} = \varepsilon_0 n_1{}^2$ and $\varepsilon_{clad} = \varepsilon_0 n_2{}^2$ refer to the permittivity of the waveguide's core and clad respectively. $\boldsymbol{u} \cdot \hat{\boldsymbol{n}}$ is the surface-normal component of the displacement vector $\boldsymbol{u}$ (the normal vector $\hat{\boldsymbol{n}}$ is directed from the core towards the clad); the fields $\boldsymbol{E}_{j,\parallel}$ and $\boldsymbol{D}_{j,\perp}$ are material interface tangential electric and normal displacement fields for the pump ($j = p$) or scattered ($j = s$) optical mode. The denominator in Eqs. (18),(19) represents the energy or power normalization integrals $N_i = (2\Re[\int (\boldsymbol{E}_i \times \boldsymbol{H}_i{}^*) \cdot \hat{z}\, dA])^{1/2}$, with i being either p or s. Equation (18) is integrated over the entire transverse cross-section of the waveguide, while Equation (19) requires a line integral to be performed along the waveguide's boundaries. The SBS total gain of a particular combination of pump, Stokes and elastic modes is calculated as follows: [21]:

$$G_B = Q_m\ \frac{2\omega_p}{\overline{\mathrm{m}}_{eff}\ \Omega_m{}^2} |Q_{PE} + Q_{MB}|^2\,, \tag{21}$$

where Q_m is the mechanical energy quality factor, $\overline{\mathrm{m}}_{eff} = \int \frac{\rho|\boldsymbol{u}_m|^2}{max|\boldsymbol{u}_m|^2}\, dA$ is the effective linear mass density of a mechanical mode with displacement profile $\boldsymbol{u}_m$, ρ is the mass density.

3 Results and Discussion

We analyze the under-etched rectangular waveguide illustrated in Fig. 3. The silicon waveguide, which is partially suspended and aligned with a ⟨110⟩ axis, operates at a wavelength of 1550 nm and is supported by a silica pillar anchor with a width of *d*. Table 1 provides a summary of the optical and mechanical properties of silicon and silica (SiO_2). For simplicity, we neglect loss and dispersion in the dielectric parameters. The two-dimensional Finite Element Method (FEM) is employed to determine the optical and elastic modes of a waveguide. The simulation is conducted using COMSOL Multiphysics software, which employs the electromagnetic wave and structural mechanics modules to determine electric and acoustic field modes by solving the corresponding equations of motion outlined in the preceding sections.

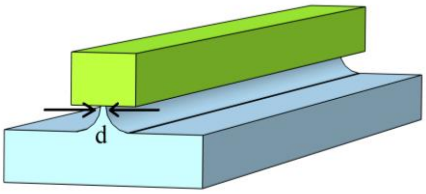

Fig. 3 The structure of the simulated partially suspended silicon waveguide on SiO_2. The cross-section dimensions measure 485 nm in width and 230 nm in height. The thickness of the pillar is represented by the variable *d*.

The distributions of electrical and acoustical fields within an SBS at specified frequencies are depicted in Fig. 4 and Fig. 5 for backward (BSBS) and forward scattering (FSBS), respectively. It is evident that in forward SBS, the electric field pattern exhibits a relatively smooth structure with a directional flow that aligns with the pump, signifying a gradual transfer of momentum. In backward SBS, the scattered electric field generates more pronounced standing-wave-like patterns, which is anticipated due to the interference between waves propagating forward and backward.

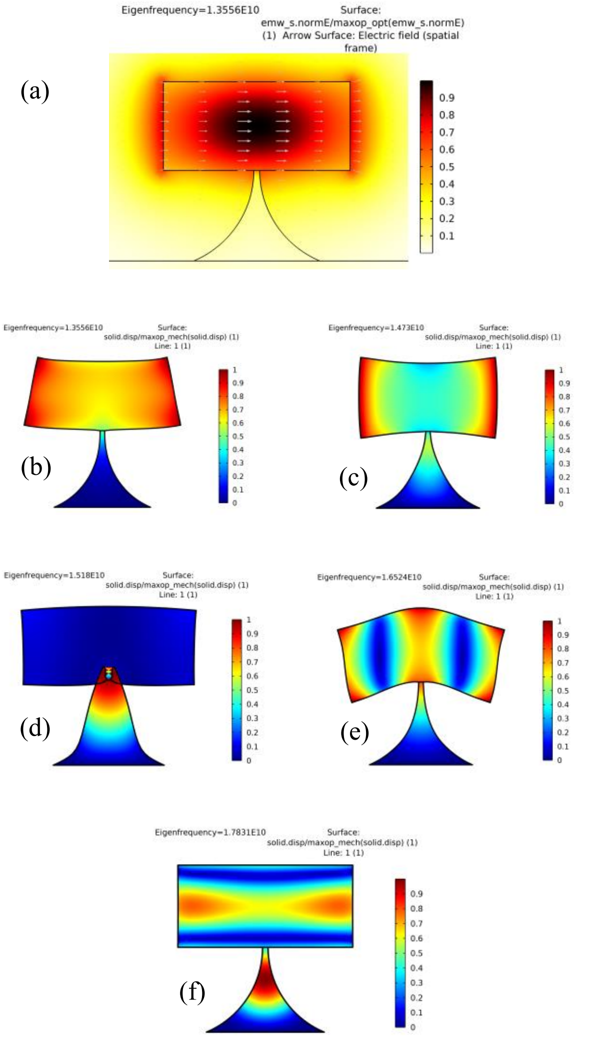

Fig. 4 Numerical simulation outcomes in backward SBS. (a) Normalized distribution of the electric field. The selective acoustic modes at their eigenfrequencies are shown in (b): 13.5 GHz, (c): 14.7 GHz, (d): 15.1 GHz, (e): 16.5 GHz, and (f): 17.8 GHz.

Concerning the acoustic mode shapes, in FSBS, the modes are predominantly transverse and flexural modes that interact with the optical field. Mode (e) at 12 GHz exhibits a pronounced shear-like displacement profile. Conversely, in BSBS, the acoustic modes are mainly longitudinal and hybrid acoustic modes (both axial and radial) at elevated frequencies. Mode (e) at 16.5 GHz exhibits significant field overlap with the optical mode, thereby enhancing the SBS gain. FSBS acoustic modes seem to be advantageous in the lower GHz range. Phonons engage over extended distances as a result of co-propagation. In BSBS, the high acoustic confinement and pronounced modal overlap at elevated GHz frequencies enhance phase matching and coupling strength.

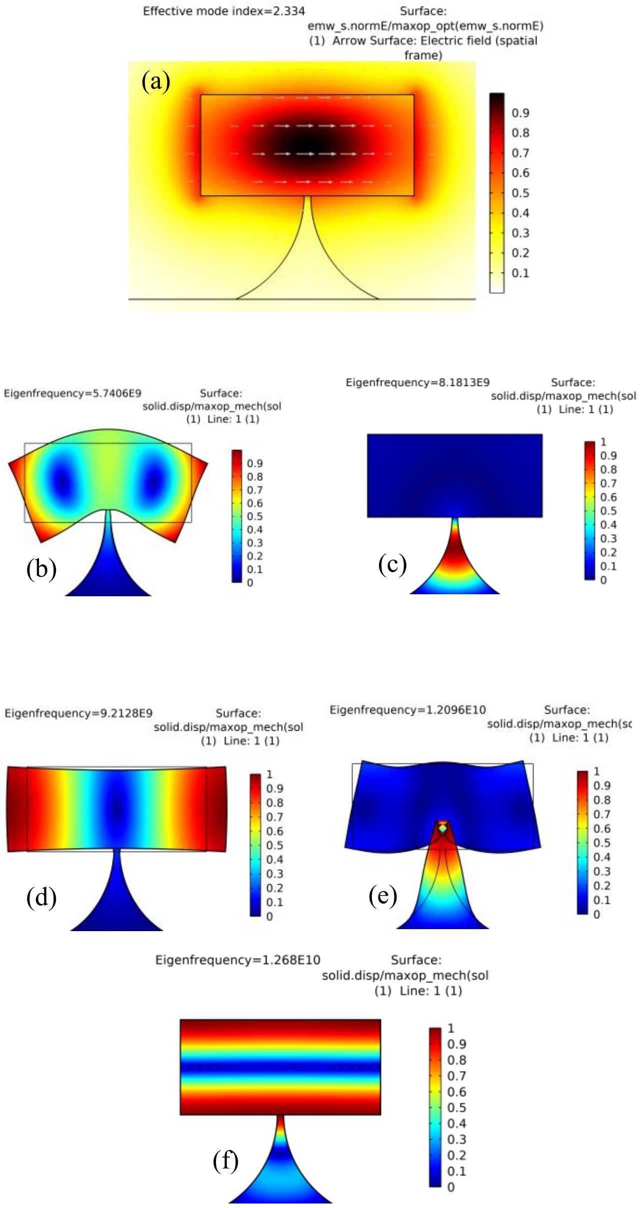

Fig. 5 Numerical simulation outcomes in forward SBS. (a) Normalized distribution of the electric field. The selective acoustic modes at their eigen-frequencies are shown in (b): 5.7 GHz, (c): 8.1 GHz, (d): 9.2 GHz, (e): 12 GHz, and (f): 12.6 GHz.

To conduct a thorough investigation, a gain analysis of BSBS is also performed. The outcomes of the gain concerning variations in frequency for photoelastic and moving boundary effects, along with the impact of the width of the pillar anchor, are depicted in Fig. 6. Sharp peaks in Fig. 6(a) indicate strong phase-matched coupling between the optical and acoustic modes at those frequencies. The PE effect dominates the total gain at two clear resonances: 14.73 GHz and 17.83 GHz. At both peaks, PE contributes the majority of the gain, indicating these are bulk strain-driven interactions. The MB effect arises from modulations of the waveguide boundaries and exhibits a secondary contribution at frequencies similar to those of the PE peaks, but is significantly smaller (~20% or less). The MB effect also slightly contributes near 15.18 GHz, where PE is minimal, suggesting a surface-localized acoustic mode. These peaks in gain correlate well with the optically active acoustic eigenmodes identified in the backward SBS configuration, indicating efficient phase-matching and spatial mode overlap. Figure 6 (b) reveals a clear trend: with an increase in pillar width from 10 nm to 40 nm, the total Brillouin gain/Q_m shows a consistent decrease from 5.48 to 0.68. Increasing the anchor width causes acoustic waves to leak into the substrate, reducing the overlap between acoustic and optical modes. The suspension must be thin enough to minimize acoustic losses but robust enough for mechanical stability. Although the main effect is acoustic, the anchor geometry can indirectly affect optical modes by altering the field distribution, which also influences mode overlap and gain. The waveguide's cross-sectional dimensions are also key factors influencing its performance. Optimized dimensions enhance the confinement of optical and acoustic modes, improving their spatial overlap and Brillouin gain [22].

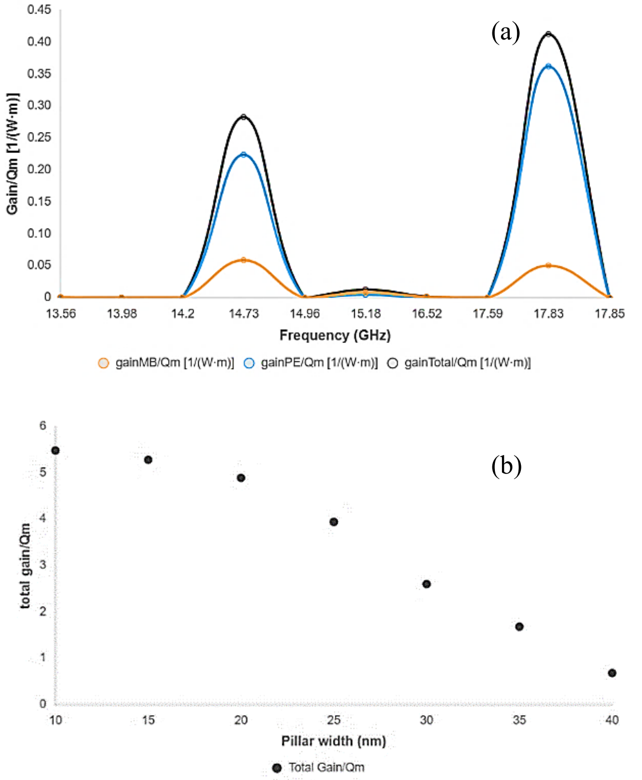

Fig. 6 (a) Total, MB, and PE Brillouin gain as a function of frequency for backward scattering (d=40 nm). (b) Total Brillouin gain as a function of pillar width.

4 Conclusion

We presented a comprehensive numerical investigation of forward and backward stimulated Brillouin scattering (SBS) in a partially suspended, z-invariant silicon rectangular waveguide. Using finite element method, we analyzed the electric field distributions and selectively coupled acoustic eigenmodes over a wide frequency range for both SBS configurations. Numerical results reveal stronger vertical and lateral confinement of the acoustic modes in the range of 13.5–17.8 GHz., further supported by gain analysis. The frequency-dependent SBS gain reveals that the photoelastic PE effect is the dominant coupling mechanism, particularly at the resonant frequencies. The MB effect contributes modestly, adding marginal gain where surface acoustic displacement is significant. The suspended design significantly reduces substrate-induced losses, facilitating effective phonon-photon coupling, which is essential for applications like on-chip optical signal processing and sensing. Our research underscores the necessity of optimizing pillar width in suspended waveguides to enhance Brillouin scattering efficiency, thereby offering a route for the development of advanced photonic devices with superior performance in integrated optoelectronic systems. Future investigations could examine the effects of material variations and structural changes to improve gain at larger widths. In summary, the findings reveal that the partially suspended waveguide configuration not only provides strong acoustic confinement but also allows for customized modal coupling across a broad frequency range.

References

1. R. W. Boyd, *Nonlinear Optics*, 3rd ed. Academic Press, SanDiego, CA, (2008)
2. L. Brillouin, *Ann. Phys.* **17**, (1922)
3. R. Y. Chiao, C. H. Townes, B. P. Stoicheff, *Phys. Rev. Lett.* **12**, (1964)
4. Z. Bai, H. Yuan, Z. Liu, P. Xu, Q. Gao, R.J. Williams, O. Kitzler, R. P. Mildren, Y. Wang, Z. Lu, *Opt. Mater.* **75**, (2018)
5. N. T. Otterstrom, R. O. Behunin, E. A. Kittlaus, Z. Wang, P. T. Rakich, *Science* **360**, (2018)
6. S. Gundavarapu, G. M. Brodnik, M. Puckett, T. Huffman, D. Bose, R. Behunin, J. Wu, T. Qiu, C. Pinho, N. Chauhan, J. Nohava, P. T. Rakich, K. D. Nelson, M. Salit, D. J. Blumenthal, *Nat. Photonics* **13**, (2019)
7. A. Choudhary, I. Aryanfar, S. Shahnia, B. Morrison, K. Vu, S. Madden, B. Luther-Davies, D. Marpaung, B. J. Eggleton, *Opt. Lett.* **41**, (2016)

8. D. Marpaung, B. Morrison, M. Pagani, R. Pant, D.-Y. Choi, B. Luther-Davies, S. J. Madden, B. J. Eggleton, *Optica* **2**, (2015)
9. C. G. Poulton, R. Pant, A. Byrnes, S. Fan, M. Steel, B. J. Eggleton, Opt. Express **20**, (2012)
10. E. A. Kittlaus, N. T. Otterstrom, P. Kharel, S. Gertler, P. T. Rakich, *Nat. Photonics* **12**, (2018)
11. M. Merklein, B. Stiller, K. Vu, S. J. Madden, B. J. Eggleton, *Nat. Commun*. **8**, (2017)
12. M. Merklein, B. Stiller, B.J. Eggleton, *J. Opt.* **20**, (2018)
13. J. Li, M.G. Suh, K. Vahala, *Optica* **4**, (2017)
14. M. Bagheri, M. Poot, L. Fan, F. Marquardt, H. X. Tang, *Phys. Rev. Lett.* **111**, (2013)
15. S. Hong, R. Riedinger, I. Marinkovi´c, A. Wallucks, S. G. Hofer, R. A. Norte, M. Aspelmeyer, S. Gröblacher, *Science* **358**, (2017)
16. R. Van Laer, B. Kuyken, D. Van Thourhout, R. Baets, *Nat. Photonics* **9**, (2015)
17. C. Wolff, M. J. A. Smith, B. Stiller, C. G. Poulton, *J. Opt. Soc. Am. B* **38**, (2021)
18. G. Wiederhecker, P. Dainese, T.P.M. Alegre, *APL Photon.* **4**, (2019)
19. S. R. Mirnaziry, C. Wolff, M. J. Steel, B. J. Eggleton, C. G. Poulton, *Opt. Express* **24**, (2016)
20. C. Wolff, M. Steel, B. Eggleton, C. Poulton, *Phys. Rev. A,* **92**, (2015)
21. J.E. Sipe, M.J.A. Steel, *New J. Phys.* **18**, (2016)
22. K Ramadhan et al, J. Phys.: Conf. Ser. **2866**, (2024)

TTMP vol 2 (3), 2025
doi: 10.30511/TTMP.2025.2065346.1057

Transactions in Theoretical
and Mathematical Physics

Hamiltonian and Diffeomorphism Generators of a Quantum Field in $R \times S^2$ Spacetime

Alireza Shariati Joni[a,1]

[1]Department of Physics, Isfahan University of Technology, Isfahan 84156-83111, Iran

Received: 09 July 2025 / Accepted: 18 August 2025 / Published: 18 August 2025

Abstract Within the ADM formalism, spacetime is foliated by spacelike hypersurfaces, dividing spacetime into space and time. In this formalism, the evolution of fields can be separated into evolution on these hypersurfaces and evolution from one hypersurface to the next. The commutators of these generators form an algebra known as the Dirac Algebra or hypersurface deformation algebra. In this paper, we expand the matter field on the three-dimensional $R \times S^2$ spacetime using the basis of spherical harmonics on S^2. Inspired by the approach of second quantization, we promote the coefficients of this expansion to creation and annihilation operators. We demonstrate that the algebra of the evolution generators, determines the Hamiltonian and diffeomorphism generators on S^2. The tensor character of the matter field is classified based on its Lie derivative with respect to its diffeomorphism generators. This quantization method determines the ordering of creation and annihilation operators in the evolution generators.

1 Introduction

In the ADM formalism, three-dimensional spacetime is foliated into spacelike surfaces. In this paper, we decompose spacetime $\mathscr{M} = R \times S^2$ into spacelike surfaces S^2 and a time axis R. Within this framework, the generators are decomposed into one generator normal to the constant-time surface $\mathscr{H}_\perp$ for evolution in time and two generators parallel to the surface $\mathscr{H}_i$, which are also known as generators of infinitesimal diffeomorphisms [1]. This decomposition leads to the emergence of the Dirac algebra (hypersurface deformation algebra) among the generators [2, 3]:

$$\{\mathscr{H}_\perp(x),\mathscr{H}_\perp(x')\} = \delta_{,i}(x,x')\left(h^{ij}(x)\mathscr{H}_j(x)+h^{ij}(x')\mathscr{H}_j(x')\right), \tag{1}$$

$$\{\mathscr{H}_i(x),\mathscr{H}_\perp(x')\} = \delta_{,i}(x,x')\mathscr{H}_\perp(x), \tag{2}$$

$$\{\mathscr{H}_i(x),\mathscr{H}_j(x')\} = \delta_{,i}(x,x')\mathscr{H}_j(x)+\delta_{,j}(x,x')\mathscr{H}_i(x'). \tag{3}$$

h_{ij} is the spatial part of metric, and its determinant is h. h^{ij} is the inverse of the metric with the condition $h_{ik}h^{kj} = \delta_i^j$. The symbol δ denotes the Dirac delta distribution defined as [4]:

$$\int h^{\frac{1}{2}} d^2x\, F(x)\ \delta(x,x') = F(x'). \tag{4}$$

$\delta_{,j} := \frac{\partial \delta}{\partial x^j}$, and x represents a point in space. $\{,\}$ denotes the Poisson bracket given by

$$\{\phi(x),\pi(x')\} = \delta(x,x'), \tag{5}$$

where ϕ is a matter field and π is its canonical conjugate momentum.

In general relativity, classical trajectories are restricted to a subspace of phase space defined by $\mathscr{H}_\perp = 0$ and $\mathscr{H}_i = 0$. Dirac algebra ensures that generators form first-class constraints. Quantization of the generators is achieved by promoting them to corresponding operators. A classical constraint is implemented in the quantum theory as a restriction on physically allowed wave functions as follows [1, 3]:

$$\hat{\mathscr{H}}_i|\Psi\rangle = 0, \quad \hat{\mathscr{H}}|\Psi\rangle = 0. \tag{6}$$

---

[a] e-mail: ar.shariati.j@gmail.com

The first equation enforces the independence of the wave function $|\Psi\rangle$ under infinitesimal coordinate transformations on the surfaces S^2. The second equation is the Wheeler-DeWitt equation [1]. Solving the Wheeler-DeWitt equation is non-trivial and often requires imposing symmetries on the theory. Additionally, operator ordering ambiguities arise when promoting Hamiltonian constraints to quantum operators [1, 5].

In the Teitelboim approach, diffeomorphism generators are determined *a priori* based on the tensorial properties of the field. For a coordinate transformation $x^\mu \to x^\mu + N^\mu$ consider evolution rule as:

$$\delta F(y) = \int d^2x\, h^{\frac{1}{2}}(x)\{F(y),\, \mathscr{H}_\mu(x)\}N^\mu(x), \tag{7}$$

Where $\mathscr{H}_\mu = (\mathscr{H}_\perp, \mathscr{H}_i)$ and $N_\mu = (N, N_i)$. If F belongs to a class of (weighted) tensor fields, the generators of infinitesimal diffeomorphism can be derived by comparing the result of (7) with its Lie derivative. For example, for a scalar field:

$$\mathscr{H}_i = \phi_{,i}\pi. \tag{8}$$

The Hamiltonian generator $\mathscr{H}_\perp$ is then derived by solving Poisson brackets (1) and (2) as differential equations [6, 7].

This paper proposes a method where all generators, along with the tensorial behavior of quantum fields, are identified through the Dirac algebra. Our approach assumes quantum fields admit an expansion in creation and annihilation operators, analogous to second quantization. We express generators in terms of these operators and demonstrate that this procedure resolves operator ordering ambiguities in generators. Note that we do not perform the second quantization approach. Unlike standard second quantization where one starts with a classical Hamiltonian, here we use Dirac algebra to derive the Hamiltonian directly in the basis of creation and annihilation operators similar to second quantization.

To circumvent mathematical complexities, we analyze the problem in three-dimensional spacetime $R \times S^2$. We expand fields using spherical harmonics $Y_{lm}(\theta, \phi)$ on S^2. This expansion yields a discrete spectrum with countable degrees of freedom. This mathematical simplification is not crucial, in conclusions and discussion we describe how one can extend this method to higher dimensions or different spacetimes.

2 ADM Decomposition

To describe this approach, we first decompose the three-dimensional spacetime with metric $g_{\mu\nu}$ into space plus time. The spacetime is hyperbolic, and on every hyperbolic manifold, there exists a temporal function, such as τ, such that each surface of constant time is a Cauchy surface with metric h_{ij} [8]. Therefore, the manifold can be foliated by these Cauchy surfaces. Every null or timelike curve intersects each Cauchy surface exactly once. Hence, τ can be considered as a representation of time, and the Cauchy surfaces can be regarded as representations of space [9, 10]. The spatial part of the metric, h_{ij}, can be obtained from the ADM metric [11]:

$$g_{\mu\nu} = \begin{pmatrix} -N^2 + N^iN_i & N_j \\ N_k & h_{jk} \end{pmatrix}. \tag{9}$$

N is called the lapse function, and N_i is known as the shift function [1]. The upper index is defined using the relation $N^i = h^{ij}N_j$.

The result of this decomposition is the emergence of Dirac algebra (1)-(3) among the Hamiltonian generators of the theory. This algebra also arises from other ideas such as parametrized systems or the principle of path independence [1–4].

The total Hamiltonian is obtained as a linear combination of these generators using the lapse and shift functions:

$$\mathscr{H} = N\mathscr{H}_\perp + N^i\mathscr{H}_i. \tag{10}$$

2.1 Vacuum solution and matter solution

We assume that there exists a vacuum solution when the matter part vanishes, so the algebra (1)-(3) closes for pure gravity.

The diffeomorphism generators decompose to gravitational and matter parts as:

$$\mathscr{H}_i = \mathscr{H}_i^{\text{matter}} + \mathscr{H}_i^{\text{gravitational}}. \tag{11}$$

If we decompose $\mathscr{H}_\perp$ into gravitational and matter parts:

$$\mathscr{H}_\perp = \mathscr{H}_\perp^{\text{matter}} + \mathscr{H}_\perp^{\text{gravitational}}, \tag{12}$$

the matter part is ultralocal with respect to the metric, meaning that it does not depend on the integral or derivative of the metric field. This result follows from the assumption that the matter part does not include the conjugate momentum of the metric. Another result of this assumption is that in Dirac algebra equations (1) and (3) are closed for matter part [4]:

$$\{\mathscr{H}_\perp^{\text{matter}}(x), \mathscr{H}_\perp^{\text{matter}}(x')\} = \delta_{,i}(x,x')\left(h^{ij}(x)\mathscr{H}_j^{\text{matter}}(x) + h^{ij}(x')\mathscr{H}_j^{\text{matter}}(x')\right), \quad (13)$$

$$\{\mathscr{H}_i^{\text{matter}}(x), \mathscr{H}_j^{\text{matter}}(x')\} = \delta_{,i}(x,x')\mathscr{H}_j^{\text{matter}}(x) + \delta_{,j}(x,x')\mathscr{H}_i^{\text{matter}}(x'). \quad (14)$$

But the remaining part of the algebra, i.e. equation (2), is not closed for matter part. From equation (13) it is obvious that $\mathscr{H}_\perp^{\text{matter}}$ depends on the metric, so for acting diffeomorphism generator on it we need the gravitational diffeomorphism generators as:

$$\{\mathscr{H}_i^{\text{matter}}(x) + \mathscr{H}_i^{\text{gravitational}}(x), \mathscr{H}_\perp^{\text{matter}}(x')\} = \delta_{,i}(x,x')\mathscr{H}_\perp^{\text{matter}}(x). \quad (15)$$

2.2 Tensorial character of the generators

Lie derivative of a function of canonical degrees of freedom like F could be calculated by using diffeomorphism generators:

$$\mathscr{L}_N F(y) = \int d^3x\, N^i(x)\{F(y),\ \mathscr{H}_i(x)\}. \quad (16)$$

Using equations (2) and (3) and by calculating Lie derivative of generators we find out $\mathscr{H}_\perp$ is a scalar density and $\mathscr{H}_i$ is a vector density of weight one under spatial coordinate transformations:

$$x^i \to x^i + N^i(x). \quad (17)$$

The scalar density field is defined by its properties under a general coordinate transformation:

$$\phi(x') = \phi(x)\left|\frac{\partial x}{\partial x'}\right|^\lambda. \quad (18)$$

In this expression, $\left|\frac{\partial x}{\partial x'}\right|$ denotes the Jacobi determinant of the transformation. We regard the parameter λ as the weight of the scalar density field. For example, the determinant of the metric h is a scalar density with weight 2. Vector density is also defined by its properties under a general coordinate transformation:

$$V_i'(x') = V_j(x)\left|\frac{\partial x}{\partial x'}\right|^\lambda \frac{\partial x^j}{\partial x'^i}. \quad (19)$$

3 Finding generators in the bases of spherical harmonics Y_{lm}

In this paper, we restrict our study to computing the generators of ϕ while neglecting the gravitational sector. For the remainder of this paper, the superscript "matter" for generators will be dropped unless stated otherwise. Consider a field like ϕ, on the S^2 we can expand this field in the basis of spherical harmonics as:

$$\phi(x) = F(x) + F^\dagger(x), \quad (20)$$

Where $F(x) := f^{lm}Y_{lm}(x)$ and $F^\dagger(x) := f^{\dagger lm}Y^*_{lm}(x)$. Summation on the repeated indexes is assumed. We assume all generators ($\mathscr{H}_\perp$, $\mathscr{H}_i$) and field operators (ϕ, π) to be Hermitian in the quantum theory, implying f^{lm} and $f^{\dagger lm}$ are Hermitian conjugates of each other. The canonical momentum conjugate to this field must also be expanded in the spherical harmonic basis. Applying Dirac quantization, replacing Poisson brackets with commutators of quantum operators, Equation (5) takes the following form:

$$[\phi(x), \pi(y)] = \mathrm{i}\delta(\mathrm{x},\mathrm{y}). \quad (21)$$

If we impose the algebra of creation and annihilation operators as:

$$[f^{lm}, f^{\dagger l'm'}] = \delta^{ll'}\delta^{mm'}, \quad (22a)$$

$$[f^{lm}, f^{l'm'}] = 0, \quad [f^{\dagger lm}, f^{\dagger l'm'}] = 0, \quad (22b)$$

where $\delta^{ll'}$ is the Kronecker delta, the canonical momentum field becomes the following Hermitian operator:

$$\pi = \frac{1}{2\mathrm{i}}(F - F^\dagger). \quad (23)$$

Similar to second quantization, by promoting the coefficients f^{lm} and $f^{\dagger lm}$ to creation and annihilation operators, we define the vacuum state $|\Omega\rangle$ via the annihilation operators:

$$f^{lm}|\Omega\rangle = 0, \quad (24)$$

while excited one-particle states are obtained by acting the creation operators on the vacuum state [12, 13]:

$$f^{\dagger lm}|\Omega\rangle = |l,m\rangle. \tag{25}$$

The Hamiltonian $\mathscr{H}_\perp$ must depend on spatial derivatives of F and $F^\dagger$ to satisfy equations (1)-(2). If we assume no derivative of fields appear in $\mathscr{H}_\perp$, from equation (1) diffeomorphism generators must be zero. then from (15), $\mathscr{H}_\perp$ vanishes.

The only fundamental elements in this theory are:

- Creation and annihilation operators $F, F^\dagger$,
- Spatial derivatives of Creation and annihilation operators like $F_{,i}$ and $F^\dagger_{,ij}$,
- The spatial metric h_{ij} and its inverse h^{ij}.

Recall that equation (15) implies that $\mathscr{H}_\perp$ must be a scalar density [4]. Consequently, terms in $\mathscr{H}_\perp$ containing only single partial derivatives of the degrees of freedom (like $F_{,i}$) are prohibited. The only admissible terms must contain Two partial derivatives contracted with the metric like $h^{ij}F_{,i}F^\dagger_{,j}$.

We exclude second-order derivative dependencies in $\mathscr{H}_\perp$ like $F^\dagger_{,ij}$ because, as shown in [7], they lead to results incompatible with Teitelboim's assumptions [4].

These constraints force the most general least-order derivative dependence to take the form:

$$\begin{aligned}\mathscr{H}_\perp =& \big(AF_{,i}F_{,j} + A^\dagger F^\dagger_{,i}F^\dagger_{,j} + BF^\dagger_{,i}F_{,j} + B^\dagger F_{,i}F^\dagger_{,j}\big)h^{ij} \\ &+E(\text{non-derivative terms}).\end{aligned} \tag{26}$$

$$[f^{lm}, f^{\dagger l'm'}] = \delta^{ll'}\delta^{mm'}, \tag{27a}$$

$$[f^{lm}, f^{l'm'}] = 0, \quad [f^{\dagger lm}, f^{\dagger l'm'}] = 0. \tag{27b}$$

The coefficients A and B are independent of creation and annihilation operators. E is a Hermitian polynomial of F and $F^\dagger$ that does not depend on their derivatives. As we will show, these coefficients will be determined by the algebra (13) and (14).

By substituting (26) into equation (13), we find:

$$AA^\dagger = B^2 = (B^\dagger)^2. \tag{28}$$

Also we obtain an expression for the diffeomorphism generator. These generators must also satisfy the closed diffeomorphism generators algebra (14). By imposing this condition, we find that the following expressions must commute with the creation and annihilation operators:

$$[f^{\dagger lm}, [f^{\dagger l'm'}, E]], \quad [f^{lm}, [f^{l'm'}, E]], \quad [f^{lm}, [f^{\dagger l'm'}, E]]. \tag{29}$$

We therefore conclude that E takes the following form:

$$E = aF^\dagger F + b(F^\dagger)^2 + b^\dagger F^2 + \mathrm{iy}(\mathrm{F}^\dagger - \mathrm{F}) + \mathrm{G}. \tag{30}$$

In this equation, the coefficients a and y are Hermitian and independent of creation or annihilation operators. G can only depend on F and $F^\dagger$ if it commutes with all derivative-dependent terms in the time evolution generator (26).

By fully computing equation (15), we obtain the following constraints:

$$a = \frac{1}{8A}, \quad b = b^\dagger = \frac{1}{16A}, \tag{31}$$

which shows that A must be Hermitian. The calculation for the quantum field theory generators can be summarized as follows:

$$\begin{aligned}\mathscr{H}_\perp =& \left(\big(A(F_{,i}F_{,j} + F^\dagger_{,i}F_{,j})h^{ij} + \frac{1}{16A}(F^\dagger F - FF)\big) + h.c.\right) \\ &+ \mathrm{iy}(\mathrm{F}^\dagger - \mathrm{F}) + \mathrm{G},\end{aligned} \tag{32}$$

$$\mathscr{H}_j = \frac{1}{4\mathrm{i}}\left(\big((FF)_{,j} + (FF^\dagger_{,j} + F^\dagger_{,j}F)\big) - h.c.\right), \tag{33}$$

where $h.c.$ denotes the Hermitian conjugate. Note that A, y, G can be depended on gravitational degrees of freedom. These results can be rewritten in terms of ϕ and π as:

$$\mathscr{H}_\perp = \frac{1}{4A}\pi^2 + A\phi_{,i}\phi_{,j}h^{ij} + 2y\pi + G, \tag{34}$$

$$\mathscr{H}_i = \frac{1}{2}\pi\phi_{,i} + \frac{1}{2}\phi_{,i}\pi. \tag{35}$$

These results demonstrate that the operator ordering is not arbitrary but emerges systematically from the theoretical calculations.

The Lie derivative of the field is computed using the diffeomorphism generators as:

$$\begin{aligned}\mathscr{L}_N\phi(x) =& \int \frac{h^{\frac{1}{2}}}{\mathrm{i}} d^2x' N^j(x')\left[\phi(x), \mathscr{H}_j(x')\right] \\ =& \phi_{,j}(x)N^j(x),\end{aligned} \tag{36}$$

which describes the field's behavior under infinitesimal coordinate transformations $x^i \to x^i + N^i(x)$. This confirms that ϕ is a scalar field. Similarly, we find its conjugate momentum π transforms as a scalar density of weight 1:

$$\begin{aligned}\mathscr{L}_N \pi(x) &= \int \frac{h^{\frac{1}{2}}}{\mathrm{i}} d^2x' N^j(x') \left[\pi(x), \mathscr{H}_j(x')\right] \\ &= \left(\pi(x) N^j(x)\right)_{,j}.\end{aligned} \tag{37}$$

4 Conclusions and Discussion

In this paper, inspired by the second quantization approach, we expanded the matter field ϕ and its conjugate momen-tum on the three-dimensional spacetime $R \times S^2$ using the spherical harmonic basis on S^2, promoting the expansion co-efficients to creation and annihilation operators. We demon-strated that the Dirac algebra under certain assumptions such as Hermiticity, determines the Hamiltonian $\mathscr{H}_\perp$ and the dif-feomorphism generators of the theory. By analyzing the dif-feomorphism generators, we established that these assump-tions lead to ϕ being a scalar field. Crucially, this algebra *automatically* fixes the operator ordering in equations (34) and (35) or equivalently, in equations (32) and (33).

The model generalizes to higher dimensions via an analogous procedure. To include the gravitational generators, one first derives the gravitational diffeomorphism generators from:

$$\begin{aligned}&[\mathscr{H}_j^{\text{matter}}(x) + \mathscr{H}_j^{\text{gravitational}}(x), \mathscr{H}_\perp^{\text{matter}}(x')] \\ &\qquad = \mathrm{i}\delta_{,\mathrm{j}}(\mathrm{x},\mathrm{x}')\mathscr{H}_\perp^{\text{matter}}(\mathrm{x}).\end{aligned} \tag{38}$$

The Hamiltonian and diffeomorphism generators are then fully determined by requiring closure of the Dirac algebra (1)-(3) for the gravitational part.

Since our quantization relies only on two key properties of spherical harmonics—orthonormality and completeness—we expect this method to generalize to other spacetimes with suitable complete basis functions.

Acknowledgements This paper is based on the author's master's thesis, supervised by Prof. Farhang Loran at Isfahan University of Technology.

References

1. C. Kiefer, *Quantum Gravity*, 3rd ed., OUP Oxford, (2012).
2. K. Kuchar, Canonical quantization of gravity. In Relativity, astrophysics and cosmology (ed. W. Israel), **238-245**. Reidel, Dordrecht, (1973).
3. P. A. M. Dirac, *lectures on quantum mechanics*, Belfer Graduate School of Science, Yeshiva University, New York, (1964).
4. C. Teitelboim, *The Hamiltonian structure of spacetime*, Princeton University, PhD dissertation, (1973).
5. M. Kenmoku, H. Kubotani, E. Takasugi, Y. Yamazaki, “Analytic Solutions of The Wheeler-Dewitt Equation in Spherically Symmetric Spacetime”, Phys. Rev. D **59**, (1999).
6. C. Teitelboim, The Hamiltonian Structure of Space-Time, *General relativity and gravitation*, vol. I, **195-225**, (1980).
7. A. Shariati Joni, "Hamiltonian Formulation of Scalar Density Field Theory," Transactions in Theoretical and Mathematical Physics, 2 1 **30-36**, (2025).
8. S. W. Hawking, and G. F. R. Ellis, *The Large Scale Structure of Space-Time*, Cambridge University Press, Cambridge, (1973).
9. R. Jha, Introduction to Hamiltonian formulation of general relativity, SciPost Phys. Lect. Notes **73**, (2023).
10. R. M. Wald, *General Relativity*, The University of Chicago Press, (1984).
11. C. W. Misner, K. S. Thorne, and J. A. Wheeler, *Gravitation*, Freeman W. H. and Company, San Francisco, (1973).
12. M. E. Peskin, D. V. Schroeder, An Introduction to Quantum Field Theory, CRC Press, (1995).
13. N. D. Birrell, P. C. W. Davies, Quantum Fields in Curved Space. Cambridge University Press (1982).

TTMP vol 2 (3), 2025
doi: 10.30511/TTMP.2025.2065547.1058

Transactions in Theoretical
and Mathematical Physics

Comparison of Proton Structure Functions in Classical and Quantum Viewpoints

Sozha Sohaily,[a,1]

[1]Department of Physics, Shahid Bahonar University of Kerman, Kerman, Iran

Received: 11 July 2025 / Accepted: 18 August 2025 / Published: 18 August 2025

Abstract A comparison between quantum statistical parton distributions and the classical perspective in the proton is presented. The structure functions and parton distributions are only provided by the entropy maximization principle and proton sum rules. In both the classical and quantum approaches, the equations for the number of proton valence quarks, conservation of momentum, and the first and second laws of thermodynamics are satisfied. However, if we use the Maxwell-Boltzmann distribution function to describe the partons in the proton structure function, the results show a clear deviation from the experimental results, while the Fermi-Dirac and Bose-Einstein distributions are in good agreement with the measurements from accelerators.

1 Introduction

The main goals of Deep Inelastic Scattering (DIS) of leptons on hadrons were to elucidate the internal hadron structure in terms of parton distributions. In the absence of a theory for the parton distributions experimentally, the distributions are approximated by different polynomials, which require numerous meaningless parameters [1, 2]. Cleymans and Thews [3], as pioneers, explored a statistical way to generate compatible Parton Distribution Functions (PDFs). Afterwards, the statistical viewpoint was applied by the other research groups [4–6]. According to the parton model, the proton is composed of a number of point-like constituents, named partons (quarks, anti-quarks and gluons). In the impulse approximation, the deep inelastic lepton–proton scattering can be viewed as a sum of elastic lepton–parton scattering, in which the incident leptons are scattered off partons instantaneously and incoherently. In the statistical approach, the proton is assumed to be a thermal system in equilibrium made up of free partons. The impulse approximation fails in the nucleon Rest Frame (RF), but works well in the Infinite Momentum Frame (IMF) [7]. In this paper, instant-form statistical expressions in the nucleon rest frame are transformed in terms of light-front kinematic variables. The longitudinal classical and quantum statistical parton distribution functions are expressed as a function of temperature, accessible volume and chemical potential for quarks, antiquarks, and gluons [8]. Antiparticles are primarily a Quantum Field Theory (QFT) construct, arising from the Dirac equation and the interpretation of negative energy solutions. In statistical mechanics or quantum thermodynamics, if antiparticles are considered in a grand canonical ensemble, their chemical potential could be taken as negative relative to their corresponding particles. The chemical potential is a measure of the change in free energy with a change in the number of particles. In classical physics, the idea of an anti-particle does not exist intrinsically. Antiparticles are a quan-tum concept with negative chemical potential due to the fact that antiparticles and particles can annihilate each other and be converted into energy. However, in modeling the classi-cal systems with antiparticles (e.g., particles with opposite charges), as a mathematical analogy, we consider them to have a negative chemical potential. The parameters are specified just by the proton sum rules and the momentum entropy optimization principle in both cases of classical and quantum statistics. Eventually, we investigate the agreement of the nucleon structure functions and parton distributions with the corresponding experimental results, based on quantum statistics compared to the classical case.

2 Theoretical Analysis

A nucleon is assumed to be a thermal system in equilibrium composed of quarks, antiquarks, and gluons in equilibrium, at a given temperature in a definite size. In the quan-

---

[a] e-mail: sohaily@uk.ac.ir

tum ap-proach, quarks and antiquarks obey the Fermi-Dirac (FD) statistics.

$$q_Q = \frac{1}{e^{\left(\frac{1}{2}Mx-\mu\right)/T}+1}, \quad q_{\bar{Q}} = \frac{1}{e^{\left(\frac{1}{2}Mx+\mu\right)/T}+1}, \tag{1}$$

where M is the nucleon mass, μ is the chemical potential, and for the antiquark $\mu_{\bar{q}} = -\mu_q$. The transverse dis-tribution of partons is neglected as a reasonable approxima-tion without decreasing the worthiness of the framework. It is due to the independence of parton motion along and perpendicular to the nucleon axis in momentum space [9–11]. Concerning the gluon, the Bose-Einstein (BE) expres-sion is as follows:

$$g_Q = \frac{1}{e^{\left(\frac{1}{2}Mx\right)/T}-1}, \tag{2}$$

with a zero potential originated from gluon emission of fermionic partons at an intermediate value of Q^2due to evolution in the quantum chromodynamic (QCD) perturbative regime. It is in consistent with the fact that hadrons behave as black body cavities for the chromodynamical radiation [12]. On the other hand, in the classic approach, parton distributions are expressed by Maxwell Boltzmann (MB) statistic:

$$q_C = e^{-\left(\frac{1}{2}Mx-\mu\right)/T}, \tag{3a}$$

$$\bar{q}_C = e^{-\left(\frac{1}{2}Mx+\mu\right)/T}, \tag{3b}$$

$$g_C = e^{-\left(\frac{1}{2}Mx\right)/T}. \tag{3c}$$

Therefore, the momentum entropy of the partons inside a nucleon, in the momentum space for the both cases QSD and CSD are given by:

$$\begin{aligned} S_Q = &-\sum_{q,\bar{q}} \left[xq(x)\ln q(x) + (1-xq(x))\ln(1-xq(x))\right] \\ &-\left[g(x)\ln g(x) - (1-g(x))\ln(1-g(x))\right], \end{aligned} \tag{4}$$

$$S_C = -\sum_{q,\bar{q},g} \left[xf(x)\ln(xf(x)) - xf(x)\right]. \tag{5}$$

The momentum distribution is used for the sake of the fact that the structure function measured by experimentalists involves momentum distributions. Furthermore, the momentum distribution is applied to introduce the concept of parton that refers to QCD. The goal is to obtain the statistical variables T, V, μ in the proton for both the quantum and classical cases. In the proposed approach, thermodynamic parameters determining statistical parton distributions of the proton are given by momentum entropy maximization under proton sum rule conditions. In fact, the proton satisfies the entropy optimum principle:

$$\frac{MV}{2(2\pi)^3}\int_0^1 S(x)\,dx \longrightarrow \text{Max}, \tag{6}$$

with proton sum rule constraints, simultaneously:

$$\frac{MV}{2(2\pi)^3}\int_0^1 \left[u(x)-\bar{u}(x)\right]dx = 2, \tag{7a}$$

$$\frac{MV}{2(2\pi)^3}\int_0^1 \left[d(x)-\bar{d}(x)\right]dx = 1, \tag{7b}$$

$$\begin{aligned} \frac{MV}{2(2\pi)^3}\int_0^1 x\left[u(x)+\bar{u}(x)+d(x)+\bar{d}(x)+g(x)\right]dx \\ = 1. \end{aligned} \tag{7c}$$

It is worth noting that in the expressed model, all parameters are statistical quantities. There is no arbitrary variable fixed by hand or fitted with the experimental data, which weakens the stringency of the approach.

3 Results and Discussion

In computing parameters, the mass of the proton, $M = 938\,\text{MeV}$, is taken as given and partons are assumed massless. Evaluated numerical values of statistical variables based on the maximum entropy method in the quantum case are $T_Q = 51.5\,\text{MeV}$, $V_Q = 0.60\,\text{MeV}^{-1}$, $\mu_u^Q = 136\,\text{MeV}$, $\mu_d^Q = 68\,\text{MeV}$.

On the other hand, for the classical case, computed statistical variables are $T_C = 97.6\,\text{MeV}$, $V_C = 1.88\,\text{MeV}^{-1}$, $\mu_u^C = 108\,\text{MeV}$, $\mu_d^C = 62\,\text{MeV}$. The composition of proton structure functions as a function of $\bar{u}$ and $\bar{d}$ is given by:

The composition of proton structure functions as a function of $\bar{u}$ and $\bar{d}$ is given by

$$F_2^p(x) = \tfrac{4}{9}\left(u(x)+\bar{u}(x)\right) + \tfrac{1}{9}\left(d(x)+\bar{d}(x)\right). \tag{8}$$

Whereas $F_2^n(x)$ is achieved from isospin symmetry approximation of the corresponding proton structure function:

$$F_2^n(x) = \tfrac{1}{9}\left(u(x)+\bar{u}(x)\right)+\tfrac{4}{9}\left(d(x)+\bar{d}(x)\right). \qquad (9)$$

It is notable that the asymptotic behavior of the structure function ratio $F_2^n(x)/F_2^p(x)$ tends to $\frac{3}{7}$ as $x \to 1$, from the precise analysis of experimental data in favor of the perturbative QCD [13]. As illustrated in Fig. 1, the quantum statistical distribution (QSD) is in good accordance with the experimental data, rather than the classical statistical distribution (CSD).

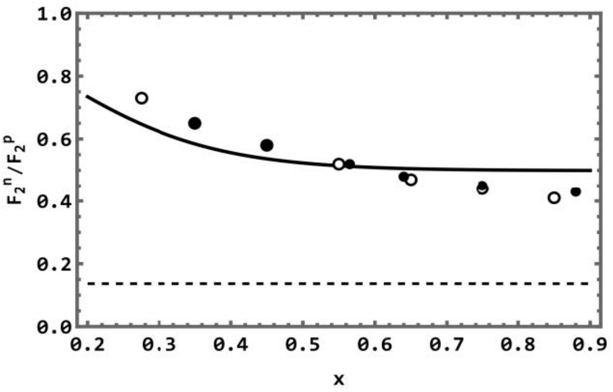

Fig. 1 Top: Comparison of our result for F_2^n/F_2^p (solid line QSD and dashed line CSD) with MST (hollow circles) and SLAC (filled circles) [13]. Bottom: Distribution of $\bar{d}-\bar{u}$ in our model (solid line QSD and dashed line CSD) compared to CTEQ6M (dash-dot line) [14].

In addition in Fig.1 Right, QSD shows a better agreement with accelerator observations which is originated from the nature of its statistic. The gluon distribution and its momen-tum distribution for the both cases of BE and MB distribu-tions are exhibited in Fig. 2. (a) and (b), respectively.

Comparison of the gluon distribution functions with the ex-perimental data in Fig. 2 shows a better agreement of the quantum gluonic distribution with the results of experiments. This fact stems from the bosonic nature of gluons. As it is clear from the obtained results, the QSDs give a fairly good description of structure functions of proton and its constituent parton distributions.

4 Conclusions

The partonic distribution functions describing the proton structure must obey quantum statistics to match experimental data.

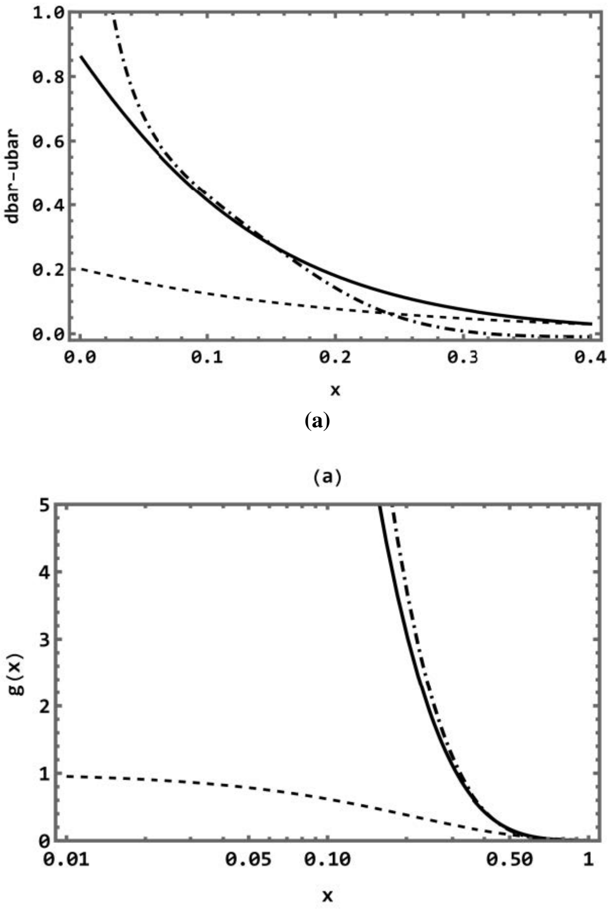

(a)

(a)

(b)

Fig. 2 Distribution of $g(x)$ and $xg(x)$ in our model (solid line QSD and dashed line CSD) in comparison to Ref. [15] (dash-dot line).

References

1. H. Abramowicz et al., Eur. Phys. J. C 75, 580 (2015).
2. R.D. Ball et al., Eur. Phys. J. C 76, 647 (2016).
3. J. Cleymans, R.L. Thews, Z. Phys. C 37, 315 (1988).
4. R.S. Bhalerao, Phys. Lett. B 380, 1–6 (1996).
5. C. Bourrely, F. Buccella, J. Soffer, Eur. Phys. J. C 23, 487 (2002).
6. Y. Zhang, L. Shao, B. Ma, Phys. Lett. B 671, 30 (2009).
7. B.Q. Ma, J. Sun, Int. J. Mod. Phys. A 6, 345 (1991).
8. B.Q. Ma, J. Sun, J. Phys. G 16, 823 (1990).
9. S. Sohaily, M. Vaziri (Khamedi), Phys. Lett. B 775, 172 (2017).
10. C. Bourrely, F. Buccella, J. Soffer, Int. J. Mod. Phys. A 28, 1350026 (2013).
11. J. Cleymans, G.I. Lykasov, A.S. Sorin, O.V. Teryaev, Phys. At. Nucl. 75, 725 (2012).
12. F. Buccella, S. Sohaily, Mod. Phys. Lett. A 30, 1550203 (2015).

13. J. Arrington, J.G. Rubin, W. Melnitchouk, Phys. Rev. Lett. 108, 252001 (2012).
14. J. Pumplin et al., J. High Energy Phys. 0207, 012 (2002).
15. R.D. Ball et al., NNPDF Collaboration, J. High Energy Phys. 1504, 040 (2015).

TTMP vol 2 (3), 2025
doi: 10.30511/TTMP.2025.2061851.1055

Transactions in Theoretical
and Mathematical Physics

Advancing numerical solutions to analytical form through the hybrid analytical and numerical method

Ali Ahmadi Azar [1, a]

[a] Department of Mechanical Engineering, NT.C., Islamic Azad University, Tehran, Iran

Received: 26 May 2025 / Accepted: 25 August 2025 / Published: 26 August 2025

Abstract Analytical solutions of differential equations provide exact representations of physical phenomena, enhance computational efficiency, and offer deeper theoretical insights than purely numerical approaches. In mathematical physics, such solutions are essential for uncovering fundamental laws, accurately predicting system behavior, and developing closed-form expressions that drive further theoretical advancements and physical interpretations. However, the complexity of real-world differential equations—with their inherent nonlinearities, variable coefficients, and intricate boundary conditions—often precludes the attainment of exact analytical solutions, resulting in the predominance of numerical methods that offer computational feasibility albeit at the cost of precision. This study aims to overcome these limitations by employing the hybrid analytical and numerical method (HAN method) to derive an analytical solution for the nonlinear differential equation (NDE) governing Jeffery–Hamel flow. Initially, numerical solutions of the governing equations are obtained to construct a comprehensive dataset, which, together with the boundary conditions, facilitates the extraction and formulation of an exact analytical solution. This HAN method effectively upgrades numerical approximations into analytical forms, thereby bridging the gap between computational practicality and theoretical rigor in the analysis of complex NDEs.

1 Introduction

1.1 Significance of the HAN method

Realistic modelling of natural phenomena often leads to highly nonlinear differential equations characterized by coplex nonlinearities, variable coefficients, and challenging boundary conditions. Although numerical methods are prevalently used to approximate solutions for these equations, their outputs are typically approximate and may lack the precise theoretical insights offered by analytical solutions. The HAN method addresses this gap by initially employing numerical techniques to obtain approximate solutions and subsequently converting these results into closed-form analytical expressions. This approach leverages the computational efficiency of numerical methods while ultimately providing the exactness and interpretability of analytical solutions, thereby offering a unique and effective framework for solving complex NDEs.

1.2 Literature review

A growing body of literature has focused on the HAN method as a novel approach to overcoming the challenges posed by NDEs. Several recent studies have demonstrated that the HAN method not only enhances computational efficiency by leveraging numerical approximations but also facilitates the extraction of precise analytical solutions that offer deeper theoretical insights. These investigations collectively underscore the potential of the HAN method to bridge the gap between conventional numerical techniques and exact analytical formulations in mathematical physics. A pioneering study [1] introduces the HAN method that converts numerical approximations of the NDEs into closed-form analytical solutions. The study investigates complex physical phenomena such as heat and mass transfer, momentum transport, and electromagnetic effects in fluid systems, where intricate nonlinearities and challenging boundary conditions often hinder direct analytical treatment. By leveraging numerical data to systematically extract analytical expressions, the HAN method overcomes these difficulties while delivering enhanced computational efficiency and precision. This approach bridges the gap between the practical benefits of numerical techniques and the deep theoretical insights offered by analytical solutions, thereby advancing the understanding of the underlying physics in mathematical modeling. In another study [2], the combined effects of thermo-diffusion, electric fields, and nonlinear thermal radiation on the steady flow of an incompressible non-Darcy Casson fluid over a vertical permeable stretchable plate were examined. The researchers employed the HAN method

---

[1] E-mail: aliahmadiazar.mech@gmail.com, a.ahmadi.azar@iau-tnb.ac.ir

to simplify the governing nonlinear partial differential equations (PDEs) into the ordinary differential equations (ODEs) through the similarity transformations (STs), demonstrating significant influences of Casson's parameter, magnetic fields, and electric fields on velocity, temperature, and concentration distributions. Additionally, the study analyzed the roles of thermal buoyancy, porous permeability, Eckert and Prandtl numbers, and chemical reactions, offering valuable insights for industrial applications involving heat transfer in non-Newtonian fluids. Another research [3] demonstrates that the HAN Method is employed to analyze the steady magnetohydrodynamic (MHD) flow of a non-Newtonian Reiner-Rivlin viscoelastic fluid confined between two parallel plates. The governing PDEs are converted into the ODEs using Von Kármán STs, and the HAN Method is applied to solve these equations analytically, with results validated against Homotopy Perturbation Method (HPM) and Runge-Kutta numerical solutions. The research further presents new quantitative findings derived from the HAN solutions, contributing to the understanding of MHD viscoelastic fluid dynamics in constrained geometries. In another study [4], researchers investigated the transient three-dimensional flow of nanomaterial thin films over a rotating angled plate by transforming the governing PDEs into nonlinear ODEs using similarity variables. The study employed modified Akbari-Ganji Method (AGM) and HAN method to solve the equations, with results validated against numerical Runge-Kutta solutions. The analysis examined key dimensionless parameters across four distinct cases, demonstrating the effectiveness of these semi-analytical approaches for complex rotating flow systems. In another study [5], researchers analysed the steady two-dimensional flow of micropolar fluids between permeable porous walls using two analytical methods to solve the nonlinear governing equations. The study revealed that key dimensionless parameters, such as coupling and spin gradient viscosity, significantly influence flow characteristics, while micro-inertia density and Peclet numbers selectively affect microrotation, temperature, and concentration profiles. The work provides novel physical insights into micropolar fluid dynamics, particularly the distinct responses of dimensionless parameters to varying flow conditions. In another study [6], researchers developed an analytical solution for the Emden-Chandrasekhar equation (ECE) in the stellar structures theory (SST). Using the HAN method, addressing a longstanding challenge in modelling polytropic stellar structures. The HAN-method provided explicit solutions for density, mass, and pressure across all regions of a star, unlike prior approaches limited to the stellar core, and introduced a dimensionless fundamental constant ($\alpha = 0.1719381834$) critical to the SST. The results, validated against experimental models, accurately predicted properties of the Sun, including its average temperature ($1.0305 \times 107\mathrm{K}$), demonstrating the method's robustness for astrophysical applications. In another study [7], researchers analysed the unsteady, two-dimensional flow of a temperature-dependent non-Newtonian (Casson) MHD fluid through an expandable/contractible channel with permeable plates. Using similarity transformations and the HAN method, the governing nonlinear PDEs were reduced to ODEs, revealing how key parameters (R and A) influence velocity profiles ($F(\xi)$, $F'(\xi)$) and temperature ($\theta(\xi)$), with suction/injection effects quantified. The study's novelty lies in its 3D/2D contour visualization of parameter variations and analysis of local skin friction and Nusselt number, validated against prior work. In another theoretical study [8], magnetohydrodynamic flow of a conducting micropolar fluid between two stretching disks was examined, with particular focus on how structural modifications (disk spacing and stretching rate) influence fluid dynamics. The analysis employed similarity transformation- ns and the HAN-method to redefine five key dimensionless parameters, connecting mathematical solutions with physical behaviour; results showed increased stretching rates sharply elevate temperature and Nusselt number, while greater disk spacing reduces microrotation and wall stress. Validation against previous work confirmed direct correlations between structural adjustments and changes in velocity profiles, thermal properties, and micro-rotation characteristics, yielding practical insights for engineering applications. In another theoretical study [9], steady laminar flow of an incompressible micropolar fluid between a porous upper disk and a solid lower disk was investigated, with governing equations reduced to ODEs via Von-Karman transformations. The study employed the Modified AGM and HAN method—novel analytical approaches for this unsolved problem—to examine how slip coefficients, Reynolds number, and micropolar parameters (vortex viscosity, spin gradient viscosity, microinertia density) affect velocity and microrotation profiles. Results, validated against existing data, revealed consistent outcomes between both methods while providing new physical insights into the system's behaviour under varying parametric conditions. In another theoretical study [10], an exact solution was derived for von Kármán swirling flow induced by an infinite-radius rotating disk with uniform suction, examining two scenarios: co-directional and opposing far-field swirl. Using similarity transformations and the HAN method, the study analysed three cases-(1) swirl without suction, (2) suction without swirl, and (3) combined effects—revealing that skin friction peaks when far-field angular velocity is negligible (Case 1) and increases with suction intensity (Case 2). The results further demonstrated that pressure reduces to a distance-dependent function when key parameters ($s = a = 0$) vanish, providing new insights into viscous flow dynamics under rotational and suction boundary conditions. Another study [11] applied the HAN method to analyse MHD hyperbolic tangent nanofluid flow over a permeable wedge, converting governing equations into ODEs containing critical dimensionless parameters. Results demonstrated that while fluid velocity showed strong dependence on Weissenberg number and magnetic effects, heat and mass transfer rates (Nusselt/Sherwood numbers) remained largely unaffected by most parameters except local Reynolds number. The research provided new understanding of parameter interactions in wedge flows, particularly regarding skin friction variations and the relative insensitivity of thermal and concentration boundary layers to many controlling factors. In another study [12], three analytical methods were employed to analyse time-dependent MHD oscillatory flow and heat transfer in an asymmetric wavy porous channel, with the pressure gradient treated as a complex function generating both real and imaginary solutions. The results demonstrated that while parameters like the Hartmann number and porous medium shape factor strongly influenced real fluid velocity, only radiation affected both real velocity and temperature profiles, with imaginary components responding uniquely to frequency and Peclet number variations. This work's significance lies in its novel approach to solving complex differential equations, validated by the remarkable agreement between all three methods' solutions, offering new precision in modelling wavy-channel flow dynamics. In another study [13], a novel analytical approach was developed to investigate flow and heat transfer in planar Taylor–Couette systems, where a rotating inner cylinder interacts with a hotter stationary outer cylinder. By transforming nonlinear PDEs into ODEs using simplifying assumptions and a penalty function replacement for pressure, the study revealed key dynamics—including a pronounced tangential velocity gradient, efficient inward heat transfer ($Nu = 1.58$ inner/-0.58 outer cylinder), and entropy generation adhering to thermodynamic laws. The work's significance lies in its quantitative validation of Taylor-Couette flow at $Re = 900$ and $Pr = 6.9$, coupled with insights into skin friction coefficients and entropy distribution, advancing the understanding of such systems beyond traditional numerical methods. In another theoretical study [14], the Klein-Gordon equation with a $\lambda\varphi^4$ interaction and symmetry-breaking term was analysed in the context of a generalized uncertainty principle incorporating minimal length scales, addressing quantum gravity predictions. The HAN method was employed to solve the resulting Euler-Lagrange equation (ELE), providing a framework to quantify corrections to scalar field systems under these modified physical assumptions. This work bridges quantum gravity phenomenology with practical computational techniques, offering insights into how Planck-scale effects might manifest in field-theoretic systems. In another study [15], the unsteady flow of a temperature-dependent Casson fluid through an expandable/contractible porous channel was analyzed using the HAN method. The results demonstrated that wall expansion increased maximum fluid velocity by 19.07% while raising average temperature by 100.92%, with the Casson parameter and Prandtl number showing significant but contrasting effects on velocity (4.7% increase) and temperature (51.5% decrease) profiles respectively. This work provides novel quantitative insights into non-Newtonian fluid behavior in deformable porous media, offering practical guidance for thermal-fluid system design in engineering applications. In another study [16], the century-old Von Kármán swirling flow problem was revisited using the innovative HAN method to derive highly accurate semi-analytical solutions. This approach uniquely combines numerical computations with analytical formulations, enabling precise calculation of key physical parameters like boundary layer thickness, shear stress, and moment coefficients that were previously challenging to determine. The work demonstrates both mathematical innovation in solving nonlinear differential equations and practical advancements in fluid mechanics analysis, particularly for rotating disk systems. In another study [17], boundary layer flow and heat transfer of a dusty hyperbolic tangent fluid over a stretching sheet were analyzed, with particular focus on thermal radiation and magnetic field effects. Using the HAN-method to solve transformed nonlinear ODEs, the research revealed that radiation significantly increases both fluid and dust-phase temperatures (e.g., fluid temperature rose 180% without magnetic field, 190% with field) while leaving velocities unaffected, with magnetic fields amplifying these thermal effects. These findings provide critical insights for industrial thermal management systems, especially in nuclear cooling and high-temperature processes where precise control of non-Newtonian fluid behavior is essential.

1.3 Problem statement

Building upon the justification for using the HAN method in Section 1.1 and the literature review in Section 1.2, this study investigates the steady, unidirectional flow of an incompressible viscous fluid emanating from a source or sink at the intersection of two rigid plane walls with an included angle of 2α where α is the angle of the channel which is in term of degree. For the divergent channel, α is considered positive ($\alpha > 0$) and for the convergent channel, α is considered negative ($\alpha < 0$). The governing equations for this physical system are derived in Section 2, while Section 3 details the application of the HAN method to solve these equations. Parametric analysis of the flow characteristics including the investigation of the different Reynolds numbers in both divergent and convergent channels is presented in Section 4, with key findings and conclusions summarized in Section 5.

2 Governing equation

2.1 Problem overview

The analysis considers the steady, incompressible flow of a viscous fluid emanating from (or converging toward) a source (or sink) situated at the junction of two rigid plane walls. These walls form a wedge characterized by a total angle of 2α. A cylindrical polar coordinate system is employed here, wherein the coordinates (r,θ,z) are defined; however, because the flow is assumed to be two-dimensional and confined to a plane, the z-direction is not considered. In this system, r denotes the radial distance from the origin, and θ represents the angular position. The flow is assumed to be purely radial, meaning that the tangential velocity component u_θ is zero ($u_\theta = 0$) and the radial component u_r is the dominant contributor. Variations in u_r depends on both the variables r and θ, that is: $u_r = u_r(r, \theta)$. This formulation is applicable to engineering applications where the fluid behavior in nonparallel channels must be accurately modeled. The two-dimensional convergent channel configuration (see Figure 1) illustrates a case where the channel contracts, thereby intensifying the flow toward the vertex. Conversely, the divergent channel configuration (see Figure 2) repre- sents an expanding channel where the flow disperses outward from the source.

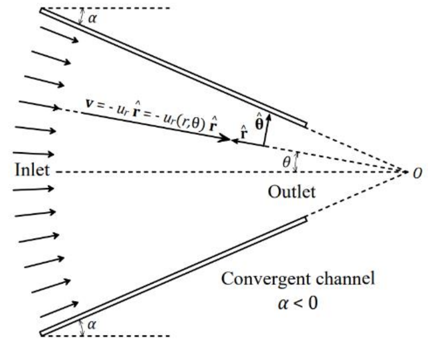

Fig. 1 Two-dimensional schematic diagram illustrating a convergent channel where the flow is directed inward toward a narrowing region, typical of a fluid sink configuration.

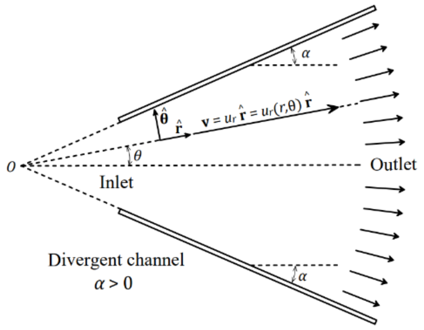

Fig. 2 Two-dimensional schematic diagram depicting a divergent channel where the flow originates from a common vertex and expands outward, typical of a fluid source configuration.

2.2 Derivation of Jeffery-Hamel flow governing equations

The Jeffery-Hamel flow describes the steady, incompressible, laminar flow of a viscous fluid between two nonparallel plane walls meeting at an angle 2α (the angle of both convergent and divergent channel is twice the angle of each wall with respect to r-axis). This flow is characterized by a purely radial velocity field, where fluid emanates from or converges toward the apex of the wedge-shaped channel. The derivation of its governing equations involves simplifying the Navier-Stokes equations under symmetry assumptions and eliminating the pressure field through mathematical consistency. In the current Section, a detailed derivation presentation tailored for readers new to this Jeffery-Hamel flow. As illustrated in Figures 1 and 2, the Jeffery–Hamel flow is governed by the steady, incompressible Navier-Stokes equations. Given the nature of the flow, the cylindrical coordinate system is the most suitable framework for its mathematical representation. Before stating the simplifications assumptions, let us demonstrate the more general form of the equations as below [18, 19]:

$$\frac{\mathrm{D}\rho}{\mathrm{D}t} + \rho\boldsymbol{\nabla}\cdot\mathbf{v} = 0, \tag{1}$$

$$\rho\frac{\mathrm{D}\mathbf{u}}{\mathrm{D}t} = -\nabla p + \mu\nabla^2\mathbf{u} + \mathbf{F}, \tag{2}$$

where $\mathrm{D}/\mathrm{D}t$ is total derivative of with respect to time, $\mathbf{u} = u_r\hat{\mathbf{r}} + u_\theta\hat{\boldsymbol{\theta}}$ is the velocity vector of the fluid, ρ is density of fluid, μ is the dynamic viscosity of the fluid, p is the pressure distribution, u_r is the radial velocity of fluid, u_θ is the azimuthal velocity of fluid, and $\mathbf{F}$ is the body force per unit volume. The Jeffery–Hamel flow in this study is considered steady, incompressible, constant viscosity, two-dimensional, and without any body forces per unit volume such as gravity or magnetic field. In addition to these assumptions, the azimuthal velocity of fluid is ignored $(u_\theta = u_\theta(r,\theta) = 0)$ in this study and the flow is purely along radial axis $(u_r = u_r(r,\theta) \neq 0)$. Therefore, Eqs. (1) and (2) reduced to the following forms:

$$\frac{1}{r}\frac{\partial}{\partial r}(ru_r) = \frac{u_r}{r} + \frac{\partial u_r}{\partial r} = 0, \tag{3}$$

$$\rho u_r\frac{\partial u_r}{\partial r} = -\frac{\partial p}{\partial r} + \mu\left(\frac{\partial^2 u_r}{\partial r^2} + \frac{1}{r}\frac{\partial u_r}{\partial r} - \frac{u_r}{r^2} + \frac{1}{r^2}\frac{\partial^2 u_r}{\partial\theta^2}\right), \tag{4}$$

$$\frac{\partial p}{\partial\theta} = \frac{2\mu}{r}\frac{\partial u_r}{\partial\theta}, \tag{5}$$

where PDEs (3)-(5) are the governing equations of the Jeffery–Hamel flow and the boundary conditions of this flow is as follows:

$$u_r(r,\pm\alpha) = 0, \tag{6}$$

$$u_r(r,\theta)|_{\theta=0} = \frac{L_{\text{char}}U_{\max}}{r}, \tag{7}$$

$$\left.\frac{\partial u_r(r,\theta)}{\partial\theta}\right|_{\theta=0} = 0. \tag{8}$$

The pressure distribution in this problem is not constant and it is function both r and θ $(p = p(r,\theta) \neq 0)$. The pressure $p(r,\theta)$ appears in both Eqs. 4-5, but it is not a primary variable of interest. To simplify the Jeffery-Hamel PDEs

(3)-(5), the pressure by enforcing consistency between the radial and angular momentum equations through cross-differentiation should be eliminated. By doing so, the first step is to start with the radial momentum equation and differentiate both sides of Eq. (4) with respect to the variable θ:

$$\rho\left(\frac{\partial u_r}{\partial\theta}\frac{\partial u_r}{\partial r}+u_r\frac{\partial^2 u_r}{\partial\theta\partial r}\right)=-\frac{\partial^2 p}{\partial\theta\partial r} +\mu\left(\frac{\partial^3 u_r}{\partial\theta\partial r^2}+\frac{1}{r}\frac{\partial^2 u_r}{\partial\theta\partial r}-\frac{1}{r^2}\frac{\partial u_r}{\partial\theta}+\frac{1}{r^2}\frac{\partial^3 u_r}{\partial\theta^3}\right), \tag{9}$$

where $\partial^2 p/\partial\theta\partial r$ can simply determine from Eq. (9) as below:

$$\frac{\partial^2 p}{\partial\theta\partial r}=\mu\left(\frac{\partial^3 u_r}{\partial\theta\partial r^2}+\frac{1}{r}\frac{\partial^2 u_r}{\partial\theta\partial r}-\frac{1}{r^2}\frac{\partial u_r}{\partial\theta}+\frac{1}{r^2}\frac{\partial^3 u_r}{\partial\theta^3}\right) -\rho\left(\frac{\partial u_r}{\partial\theta}\frac{\partial u_r}{\partial r}+u_r\frac{\partial^2 u_r}{\partial\theta\partial r}\right). \tag{10}$$

The second step is to start with the angular momentum result and differentiate both sides of Eq. (5) with respect to the variable r:

$$\frac{\partial^2 p}{\partial r\partial\theta}=-\frac{2\mu}{r^2}\frac{\partial u_r}{\partial\theta}+\frac{2\mu}{r}\frac{\partial^2 u_r}{\partial r\partial\theta}. \tag{11}$$

For a smooth pressure field, mixed partial derivatives must be equal:

$$\frac{\partial^2 p}{\partial\theta\partial r}=\frac{\partial^2 p}{\partial r\partial\theta}. \tag{12}$$

So, by substituting the Eqs. (10) and (11) into Eq. (12), yields the following equation:

$$\underbrace{\mu\left(\frac{\partial^3 u_r}{\partial\theta\partial r^2}+\frac{1}{r}\frac{\partial^2 u_r}{\partial\theta\partial r}+\frac{1}{r^2}\frac{\partial u_r}{\partial\theta}+\frac{1}{r^2}\frac{\partial^3 u_r}{\partial\theta^3}\right)}_{\text{Viscous terms}} =\underbrace{\rho\left(\frac{\partial u_r}{\partial\theta}\frac{\partial u_r}{\partial r}+u_r\frac{\partial^2 u_r}{\partial\theta\partial r}\right)}_{\text{Inertial terms}}. \tag{13}$$

The continuity equation (3) and momentum equations (4) and (5), along with their corresponding boundary conditions (6)-(8), have been simplified but remain analytically challenging to solve. One effective approach to facilitate their solution is to reduce the number of independent variables. By introducing a similarity variable, η, in place of the original variables r and θ, the partial differential equations (PDEs) governing Jeffery-Hamel flow can be transformed into a single nonlinear ordinary differential equation (ODE). This simplification significantly enhances the tractability of the problem while preserving its physical essence.

The similarity variables that can do that, are as below [20-31]:

$$F(\eta):=\frac{f(\theta)}{L_{\text{char}}U_{\max}}=\frac{ru_r(r,\theta)}{L_{\text{char}}U_{\max}},\quad \eta:=\frac{\theta}{\alpha}, \tag{14}$$

where in Eq. (14), $U_{\max}=U_{\text{char}}$ and also the similarity variable in Eq. (14) is satisfied in the continuity equation (3), which is showed in Eq. (15):

$$\frac{1}{r}\frac{\partial}{\partial r}\left(r\frac{f(\theta)}{r}\right)=\frac{1}{r}\cdot 0=0. \tag{15}$$

Applying the similarity variables of Eq. (14) in Eq. (13), will results the ODE form of Eq. (13). Thus, the both viscous and inertial terms changed as follows, respectively:

$$\begin{aligned}&\mu\left(\frac{\partial^3 u_r}{\partial\theta\partial r^2}+\frac{1}{r}\frac{\partial^2 u_r}{\partial\theta\partial r}+\frac{1}{r^2}\frac{\partial u_r}{\partial\theta}+\frac{1}{r^2}\frac{\partial^3 u_r}{\partial\theta^3}\right)\\ &=\mu\left(\frac{2L_{\text{char}}U_{\max}}{r^3\alpha}\frac{\mathrm{d}F(\eta)}{\mathrm{d}\eta}+\frac{L_{\text{char}}U_{\max}}{r^3\alpha}\frac{\mathrm{d}F(\eta)}{\mathrm{d}\eta}+\frac{L_{\text{char}}U_{\max}}{r^3\alpha}\frac{\mathrm{d}F(\eta)}{\mathrm{d}\eta}+\frac{L_{\text{char}}U_{\max}}{r^3\alpha^3}\frac{\mathrm{d}^3F(\eta)}{\mathrm{d}\eta^3}\right)\\ &=\frac{\mu L_{\text{char}}U_{\max}}{r^3}\left(\frac{4}{\alpha}\frac{\mathrm{d}F(\eta)}{\mathrm{d}\eta}+\frac{1}{\alpha^3}\frac{\mathrm{d}^3F(\eta)}{\mathrm{d}\eta^3}\right).\end{aligned} \tag{16}$$

$$\begin{aligned}&\rho\left(\frac{\partial u_r}{\partial\theta}\frac{\partial u_r}{\partial r}+u_r\frac{\partial^2 u_r}{\partial r\partial\theta}\right)\\ &=\rho\left\{\left[\frac{L_{\text{char}}U_{\max}}{r\alpha}\frac{\mathrm{d}F(\eta)}{\mathrm{d}\eta}\right]\left[-\frac{L_{\text{char}}U_{\max}}{r^2}F(\eta)\right]+\left[\frac{L_{\text{char}}U_{\max}}{r}F(\eta)\right]\left[-\frac{L_{\text{char}}U_{\max}}{r^2\alpha}\frac{\mathrm{d}F(\eta)}{\mathrm{d}\eta}\right]\right\}\\ &=-\frac{\rho(L_{\text{char}}U_{\max})^2}{r^3\alpha}\left[F(\eta)\frac{\mathrm{d}F(\eta)}{\mathrm{d}\eta}+F(\eta)\frac{\mathrm{d}F(\eta)}{\mathrm{d}\eta}\right]\\ &=-\frac{2\rho(L_{\text{char}}U_{\max})^2}{r^3\alpha}F(\eta)\frac{\mathrm{d}F(\eta)}{\mathrm{d}\eta}.\end{aligned} \tag{17}$$

Thus, the results of substituting the similarity variable (14) into momentum equation (13) is showed in Eqs. (16) and (17). By substituting them, the following dimensional ODE will be determined:

$$\frac{\mu L_{\text{char}}U_{\max}}{r^3}\left(\frac{4}{\alpha}\frac{\mathrm{d}F(\eta)}{\mathrm{d}\eta}+\frac{1}{\alpha^3}\frac{\mathrm{d}^3F(\eta)}{\mathrm{d}\eta^3}\right) =-\frac{2\rho(L_{\text{char}}U_{\max})^2}{r^3\alpha}F(\eta)\frac{\mathrm{d}F(\eta)}{\mathrm{d}\eta}, \tag{18}$$

where Eq. (18) is the simpler form of Eq. (13). By multiply the $r^3/\mu L_{\text{char}}U_{\max}$ in Eq. (18), will make this ODE, dimensionless as below:

$$\frac{4}{\alpha}\frac{\mathrm{d}F(\eta)}{\mathrm{d}\eta}+\frac{1}{\alpha^3}\frac{\mathrm{d}^3F(\eta)}{\mathrm{d}\eta^3} = -\frac{2\rho L_{\text{char}}U_{\max}}{\mu\alpha}F(\eta)\frac{\mathrm{d}F(\eta)}{\mathrm{d}\eta}, \tag{19}$$

where multiplying the α^3 in both sides of Eq. (19), the following dimensionless ODE will be achieved:

$$\frac{\mathrm{d}^3F(\eta)}{\mathrm{d}\eta^3}+2\alpha ReF(\eta)\frac{\mathrm{d}F(\eta)}{\mathrm{d}\eta}+4\alpha^2\frac{\mathrm{d}F(\eta)}{\mathrm{d}\eta}=0, \tag{20}$$

where Re in Eq. (20) is the Reynolds number is defined in Eq. (21):

$$Re=\frac{\alpha\rho L_{\text{char}}U_{\max}}{\mu}. \tag{21}$$

In many published studies [20-31], the similarity variable of Eq. (14) is used by them and they derived the dimensionless ODE of the Jeffery-Hamel flow exactly like Eq. (20). Again, by applying the similarity variables (14) on boundary conditions (BCs) of the PDEs (6)-(8) and making them dimensionless, the following boundary conditions are derived:

$$F(\eta)|_{\eta=0}=1,\quad \left.\frac{\mathrm{d}F(\eta)}{\mathrm{d}\eta}\right|_{\eta=0}=0,\ \ F(\eta)|_{\eta=1}=0. \tag{22}$$

Now the BCs (22) are appropriate for the Jeffery–Hamel equation (which is showed in Eq. (20)).

3 The application of HAN method

The HAN method represents a groundbreaking approach in computational mathematics, first introduced by A. Ahmadi Azar [16, 17]. It is distinguished as the first technique capable of transforming numerical solutions into analytical forms, thereby resolving convergence issues and mitigating the unwieldy increase in the number of terms typical of many analytical solutions. In essence, the HAN method achieves an analytical solution with a remarkably concise representation.

A further strength of this method is its inherent flexibility. When a nonlinear differential equation defies solution by a specific numerical method, the HAN method can seamlessly incorporate an alternative numerical approach to generate the desired solution. At its core, the method unfolds in five systematic steps. First, an analytical solution is postulated in the form of a power series or polynomial featuring constant yet undetermined coefficients. These coefficients are then determined by solving a system of algebraic equations that arise from the BCs of the differential equations—a procedure encapsulated in the second step.

Typically, the number of unknown coefficients needs the number of equations derivable directly from the given boundary conditions. To bridge this gap, additional approximated boundary conditions are introduced in the third step based on numerical solutions. This practical adaptation highlights the method's versatility, as it is not restricted to any specific numerical technique. In the fourth step, these approximated conditions are employed to formulate sufficient algebraic equations, and finally, the resulting linear system is solved to obtain the semi-analytical solution of the differential equation.

By successfully combining numerical and analytical techniques, the HAN method liberates researchers from the constraints of conventional analytical methods, offering a robust framework for deriving concise analytical solutions from numerical data.

In steps three and five, the method inherently assumes the validity of the results, so explicit validation is not initially addressed. Nevertheless, to rigorously confirm correctness, one can demonstrate the convergence of the numerical solution between steps three and four. Furthermore, substituting the derived analytical solution back into the differential equation enables an evaluation of the residual error—which, if the solution is accurate, remains negligible.

In our study, we implemented the Runge-Kutta method in Python to solve the differential equation, and we verified the convergence of the computed results to support the accuracy of our approach. Ultimately, executing all five steps and reinserting the analytical solution into the original equation conclusively substantiates the validity of the results.

This comprehensive verification framework not only bolsters the reliability of the HAN method but also underscores its potential for yielding precise solutions in complex computational scenarios.

According to the five steps that HAN method has, let us assume an analytical solution (ansatz) with constant but unknown coefficients for the Jeffery-Hamel equation (20) as follows:

$$F(\eta)=\sum_{i=0}^{11}a_i\eta^i, \tag{23}$$

where a_i in Eq. (23) represents 12 unknown coefficients the unknown. These unknown coefficients can be determined only when a system of consisting 12 algebraic equations constructed. The analytical solution that is already defined in the Eq. (23) is the first step of HAN method. The second step is to use the boundary conditions of the Jeffery-Hamel equation (20) which they are existed in Eq. (22) to make algebraic equations as follows:

$$F(\eta)|_{\eta=0}=\left.\sum_{i=0}^{11}a_i\eta^i\right|_{\eta=0}=1, \tag{24}$$

$$\left.\frac{\mathrm{d}F(\eta)}{\mathrm{d}\eta}\right|_{\eta=0}=\sum_{i=1}^{11} i a_i \eta^{i-1}\Big|_{\eta=0}=0, \tag{25}$$

$$F(\eta)|_{\eta=1}=\sum_{i=0}^{11} a_i \eta^{i}\Big|_{\eta=1}=0. \tag{26}$$

It is obvious that the number of Eqs. (24)-(26) are not enough to construct a system of algebraic equations. In order to construct additional algebraic equations, the numerical solution of the Jeffery-Hamel equation (۲۰) with its boundary conditions (۲۲) should be calculated which is the third step in the HAN method. The numerical solving of Eq. (۲۰) with its boundary conditions (۲۲) is successfully done via "*Fourth-order Implicit Runge-Kutta Collocation Method (Lobatto IIIA Formula) with Adaptive Mesh Refinement*". Why the name this numerical method is like this? The answer is written in the following reasons:

- Implicit Runge-Kutta Framework: The method is based on an implicit Runge-Kutta formulation. Unlike explicit methods, it solves for the solution at multiple, interdependent collocation points simultaneously. This inherent implicitness grants excellent stability properties, particularly in stiff or complex boundary value problems like the one in your code.
- Collocation Approach: In a collocation method, the solution is approximated by a polynomial that is forced to satisfy the differential equation at a set of predefined points (the collocation points). This guarantees that the residual (error in satisfying the ODE) is nearly zero at those points, leading to a highly accurate overall solution.
- Lobatto IIIA Formula: The Lobatto IIIA variant is a specific choice for the collocation points and weights. A distinguishing feature is that this formula includes the endpoints of the integration interval, making it ideally suited for boundary value problems. It also confers additional symmetry and stability properties to the scheme.
- Fourth-order Accuracy: The method achieves fourth-order accuracy, meaning the local error decreases in proportion to the step size raised to the fourth power ($O(h^4)$). This level of accuracy strikes a balance between computational effort and precision, making it robust for many practical problems.
- Adaptive Mesh Refinement: The solver doesn't rely on a fixed grid; it adapts the mesh based on error estimates. Regions where the solution changes rapidly get more refined mesh points, whereas smoother areas use fewer points. This adaptive approach enhances both efficiency and accuracy by focusing computational power where it's needed most.

Each part of the name highlights a key element of the solver's design, and together they describe a method that is stable, accurate, and efficient for solving boundary value problems. The shorter name of this numerical method is "*Fourth-order Lobatto IIIA Collocation Method with Adaptive Mesh Refinement*". Thus, according to this code, the approximated boundary conditions or the numerical solution of the Jeffery-Hamel equation (۲۰) with its boundary conditions (۲۲) are calculated as follows:

Table 1 The numerical solution of the Jeffery-Hamel equation via Python for the scenario that $\alpha = 30°$ and $Re = 10$.

η	$F(\eta)$	$\mathrm{d}F(\eta)/\mathrm{d}\eta$	$\mathrm{d}^2F(\eta)/\mathrm{d}\eta^2$
0.0	1.000000	0.000000	-4.308476
0.1	0.978666	-0.422594	-4.063804
0.2	**0.917061**	**-0.798136**	-3.384597
0.3	0.821856	-1.089728	-2.413316
0.4	**0.702610**	**-1.277112**	-1.330752
0.5	0.570009	-1.357724	-0.301810
0.6	**0.434249**	**-1.343074**	0.560922
0.7	0.303917	-1.252785	1.207615
0.8	**0.185483**	**-1.108688**	1.641027
0.9	0.083311	-0.930512	1.896907
1.0	0.000000	**-0.733586**	2.024627

The Figures 3-5 shows the plots of $F(\eta)$, $\mathrm{d}F(\eta)/\mathrm{d}\eta$, and $\mathrm{d}^2F(\eta)/\mathrm{d}\eta^2$ respectively. However, the validity of the current numerical solution is showed by the residual of the numerical solution in Figure 6.

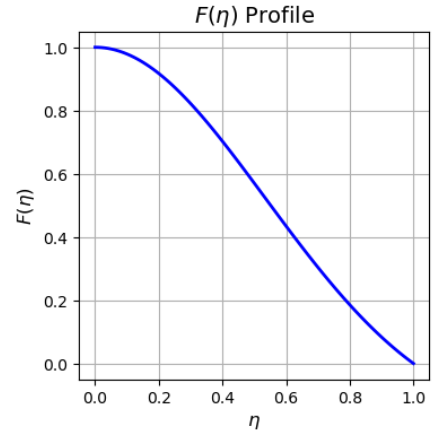

Fig. 3 The numerical solution of $F(\eta)$ by Python.

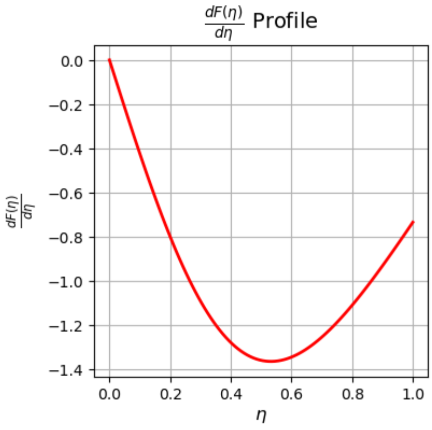

Fig. 4 The numerical solution of $\mathrm{d}F(\eta)/\mathrm{d}\eta$ by Python.

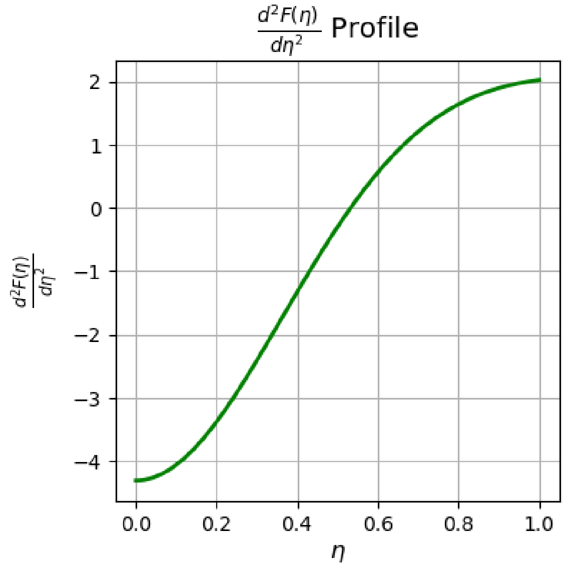

Fig. 5 The numerical solution of $\mathrm{d}^2F(\eta)/\mathrm{d}\eta^2$ by Python.

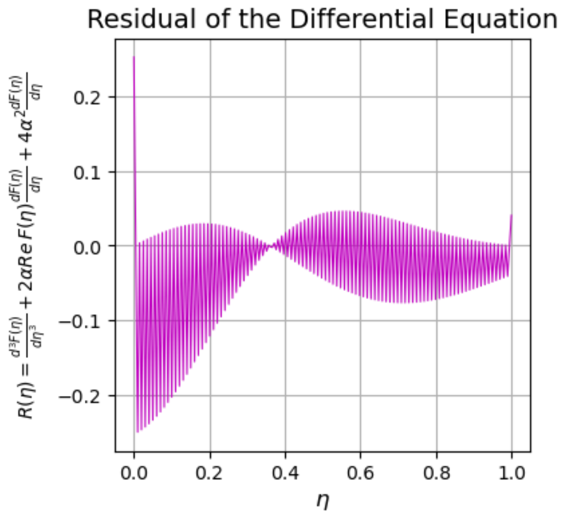

Fig. 6 The residual of numerical solution by Python.

The bold values in Table 1 are the approximated boundary conditions that are used in step four to make the rest of remaining algebraic equations as follows:

$$F(\eta)|_{\eta=0.2}=\sum_{i=0}^{11}a_i\eta^i\Big|_{\eta=0.2}=0.917061, \tag{27}$$

$$\left.\frac{\mathrm{d}F(\eta)}{\mathrm{d}\eta}\right|_{\eta=0.2}=\sum_{i=1}^{11}ia_i\eta^{i-1}\Big|_{\eta=0.2}=-0.798136, \tag{28}$$

$$F(\eta)|_{\eta=0.4}=\sum_{i=0}^{11}a_i\eta^i\Big|_{\eta=0.4}=0.702610, \tag{29}$$

$$\left.\frac{\mathrm{d}F(\eta)}{\mathrm{d}\eta}\right|_{\eta=0.4}=\sum_{i=1}^{11}ia_i\eta^{i-1}\Big|_{\eta=0.4}=-1.277112, \tag{30}$$

$$F(\eta)|_{\eta=0.6}=\sum_{i=0}^{11}a_i\eta^i\Big|_{\eta=0.6}=0.434249, \tag{31}$$

$$\left.\frac{\mathrm{d}F(\eta)}{\mathrm{d}\eta}\right|_{\eta=0.6}=\sum_{i=1}^{11}ia_i\eta^{i-1}\Big|_{\eta=0.6}=-1.343074, \tag{32}$$

$$F(\eta)|_{\eta=0.8}=\sum_{i=0}^{11}a_i\eta^i\Big|_{\eta=0.8}=0.185483, \tag{33}$$

$$\left.\frac{\mathrm{d}F(\eta)}{\mathrm{d}\eta}\right|_{\eta=0.8}=\sum_{i=1}^{11}ia_i\eta^{i-1}\Big|_{\eta=0.8}=-1.108688, \tag{34}$$

$$\left.\frac{\mathrm{d}F(\eta)}{\mathrm{d}\eta}\right|_{\eta=1}=\sum_{i=1}^{11}ia_i\eta^{i-1}\Big|_{\eta=1}=-0.733586, \tag{35}$$

where Eqs. (24)-(26) with addition to the Eqs. (27)-(35) are constructing a system of linear algebraic equation with 12 algebraic equations and 12 unknowns. By solving this system of linear algebraic equations in fifth step, the unknown coefficients in Eq. (36) will be determined as below:

$$\begin{array}{ll} a_0=+1.000000, & a_1=+\,0.000000,\\ a_2=-\,2.153993, & a_3=-\,0.001129,\\ a_4=+2.091526, & a_5=-\,0.107366,\\ a_6=-\,1.135709, & a_7=-\,1.364453,\\ a_8=\ +3.745790, & a_9=-\,3.081673,\\ a_{10}=+1.194394, & a_{11}=-0.187388, \end{array} \tag{36}$$

with substituting the known coefficients in Eq. (36), the following polynomial solution will be achieved for the Jeffery-Hamel equation (20) with its boundary conditions (22):

$$\begin{aligned} F(\eta)=\ &-0.187388\,\eta^{11}+\ 1.194394\eta^{10}\\ &-3.081673\,\eta^9+3.745790\,\eta^8\\ &-1.364453\,\eta^7-\ 1.135709\,\eta^6\\ &-0.107366\,\eta^5+\ 2.09152\ 6\eta^4\\ &-0.001129\,\eta^3-\ 2.153993\,\eta^2\\ &+1.000000\,. \end{aligned} \tag{37}$$

The Figures 7-9 shows the plots of $F(\eta)$, $\mathrm{d}F(\eta)/\mathrm{d}\eta$, and $\mathrm{d}^2F(\eta)/\mathrm{d}\eta^2$ from HAN solution (37), respectively.

However, the validity of the current analytical solution is showed by the residual of the HAN solution in Figure 10.

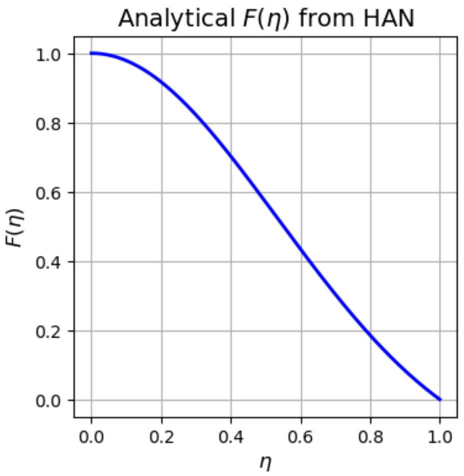

Fig. 7 The HAN solution of $F(\eta)$ by Python.

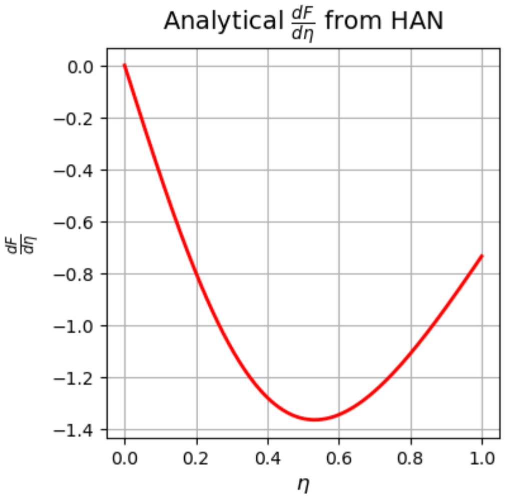

Fig. 8 The HAN solution of $dF(\eta)/d\eta$ by Python.

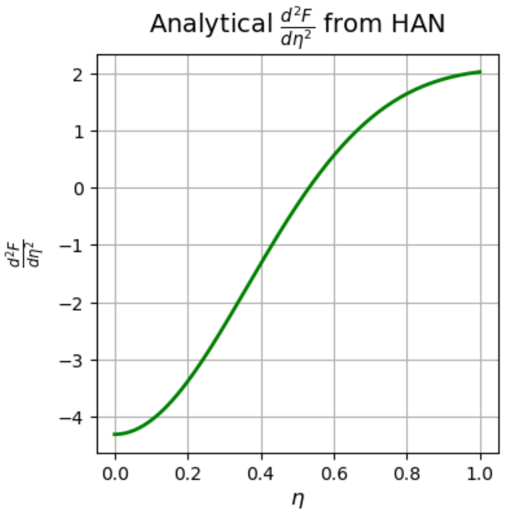

Fig. 9 The HAN solution of $d^2F(\eta)/d\eta^2$ by Python.

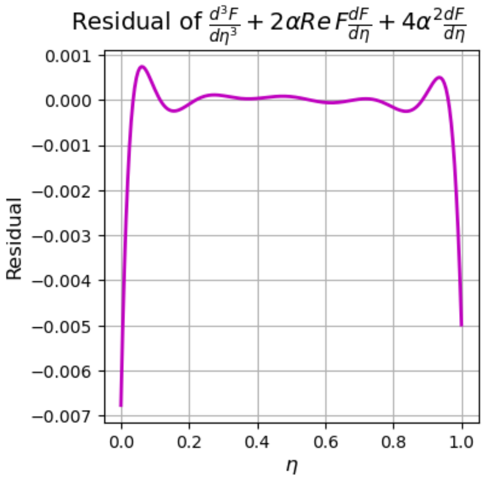

Fig. 10 The residual of HAN solution.

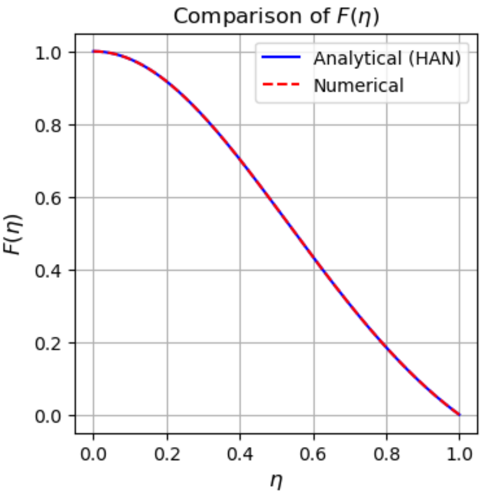

Fig. 11 The comparison between the HAN and numerical solutions of $F(\eta)$.

The validity of results is proved two times when the residuals of the both numerical and analytical solutions are showed in Figures 6 and 10. However, it is obvious that the graphs of HAN solution are significantly same as each other. Thus, the Figures 11-13 are showing the comparison of these two methods and finally Figures 14-16 shows how much is the error between HAN and the numerical solution is. Also, the calculated errors in Figures 14-16 are achieved with the help of the following relation:

$$PE = \left(\frac{|\text{Analytical} - \text{Numerical}|}{|\text{Numerical}|}\right) \times 100\%, \tag{38}$$

where PE is Percentage Error and the formula in Eq. (38) calculates percentage error relative to the maximum magnitude of the numerical solution to avoid division-by-zero issues and contextualize errors across the domain. By taking the absolute difference between analytical (HAN) and numerical values (|Analytical - Numerical|), it captures the raw deviation. Dividing by the absolute value of the numerical solution (|Numerical|) normalizes the error relative to the scale of the problem, ensuring stability even near zero-crossings. Multiplying by 100 converts this ratio into a percentage, providing an intuitive measure of how large the error is compared to the solution's peak magnitude. This approach balances sensitivity to local errors with robustness against numerical instabilities.

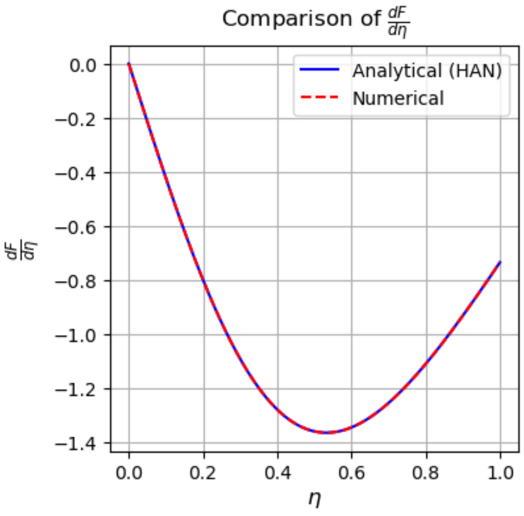

Fig. 12 The comparison between the HAN and numerical solutions of $\mathrm{d}F(\eta)/\mathrm{d}\eta$.

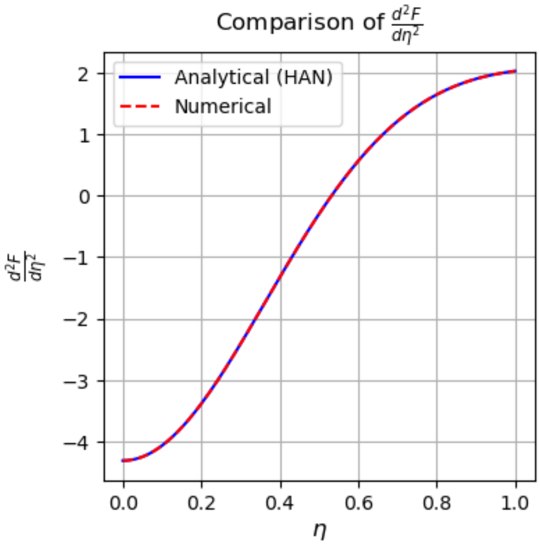

Fig. 13 The comparison between the HAN and numerical solutions of $\mathrm{d}^2F(\eta)/\mathrm{d}\eta^2$.

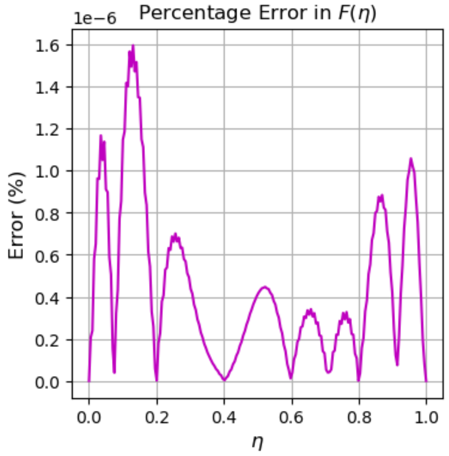

Fig. 14 The error between the HAN and numerical solutions for $F(\eta)$.

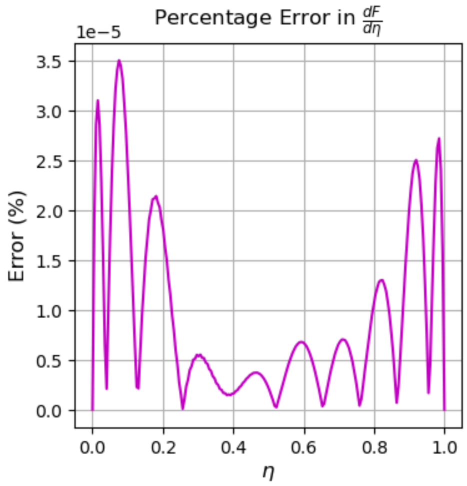

Fig. 15 The error between the HAN and numerical solutions for $\mathrm{d}F(\eta)/\mathrm{d}\eta$.

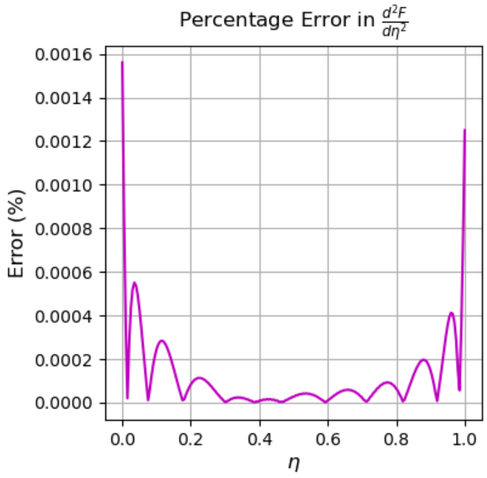

Fig. 16 The error between the HAN and numerical solutions for $\mathrm{d}^2F(\eta)/\mathrm{d}\eta^2$.

4 Results and discussion

4.1 Constitutive equations for the average value and percentage change

Before presenting the results and discussion, the average value of $F(\eta)$—representing the HAN solution for the Jeffery–Hamel flow described in Eq. (20)—along with its variation relative to a reference value is displayed as follows:

$$F_{\text{avg}} = \int_0^1 F(\eta)\mathrm{d}\eta. \tag{39}$$

$$\%\text{Change} = \frac{\text{Average}_{\text{new}} - \text{Average}_{\text{old}}}{\text{Average}_{\text{old}}} \times 100. \tag{40}$$

In Eq. (39), F_{avg} denotes the average value of $F(\eta)$ and %Change in Eq. (40), represents the percentage variation corresponding to a specific change.

4.2 Impact of Reynolds number and angle of wall in a divergent channel

4.2.1 Plot comparison of $\boldsymbol{F(\eta)}$ for different positive angles at fixed $\boldsymbol{Re}$

In the present subsection, a specific flow configuration is examined by analysing an incompressible fluid with constant velocity—which results in a constant Reynolds number—as the wall angle in a divergent channel increase. Quantitative results are presented in Tables 2–4. These tables indicate that as the channel's wall angle increases, the average fluid velocity decreases. This trend is consistent across all Reynolds numbers; however, Figures 17–19 and Tables 2–4 reveal that the decrease in velocity is more pronounced at higher Reynolds numbers. In other words, higher Reynolds numbers exhibit greater sensitivity to variations in the channel wall angles. Alternatively, when the wall angles decrease—approaching a configuration resembling a channel with flat walls—the average fluid velocity increases, with the effect being markedly stronger at high Reynolds numbers. Thus, for a given Reynolds number in a diverging channel, larger wall angles lead to lower average fluid velocities, while smaller angles result in higher average velocities. From an engineering perspective, among a range of positive channel angles, the largest angle produces the lowest velocity, and the smallest positive angle produces the highest velocity. It is important to note that differential equation (Eq. 20) is applicable only for channels that are either convergent ($\alpha < 0$) or divergent ($\alpha > 0$). At angles of 0°, 90°, 180°, or 360°, the channel is neither convergent nor divergent, and consequently, Jeffery–Hamel's equation (Eq. 20) cannot be applied.

Table 2 The quantitative results for for different positive angles when $Re = 5$.

α (deg)	F_{avg} (Average $F(\eta)$)	% Change (vs α = 5°)
5	0.659	0.0%
15	0.641	-2.7%
30	0.606	-8.1%

Table 3 The quantitative results for for different positive angles when $Re = 10$.

α (deg)	F_{avg} (Average $F(\eta)$)	% Change (vs α = 5°)
5	0.652	0.0%
15	0.617	-5.3%
30	0.550	-15.6%

Table 4 The quantitative results for for different positive angles when $Re = 20$.

α (deg)	F_{avg} (Average $F(\eta)$)	% Change (vs α = 5°)
5	0.637	0.0%
15	0.564	-11.4%
30	0.431	-32.3%

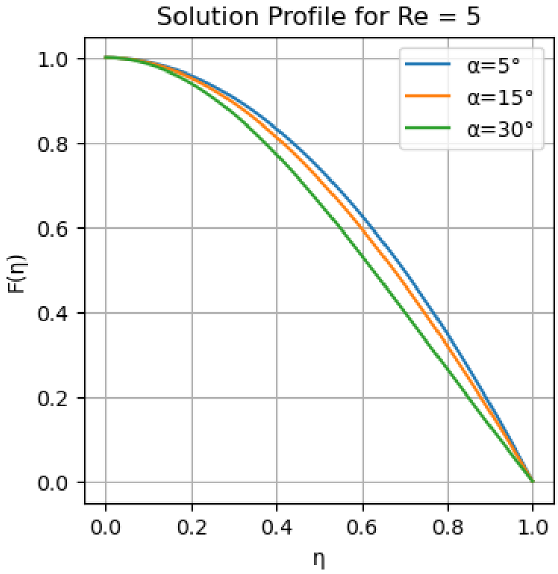

Fig. 17 Plot comparison of $F(\eta)$ for different positive angles when $Re = 5$.

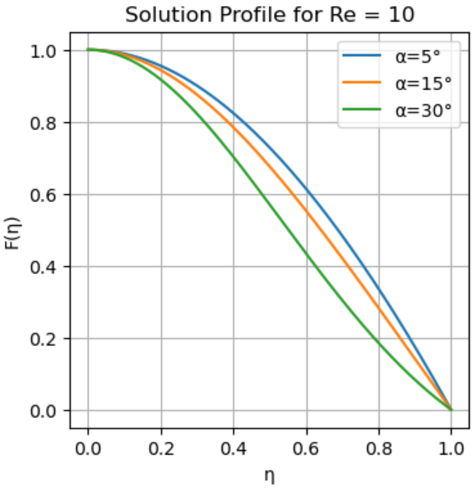

Fig. 18 Plot comparison of $F(\eta)$ for different positive angles when $Re = 10$.

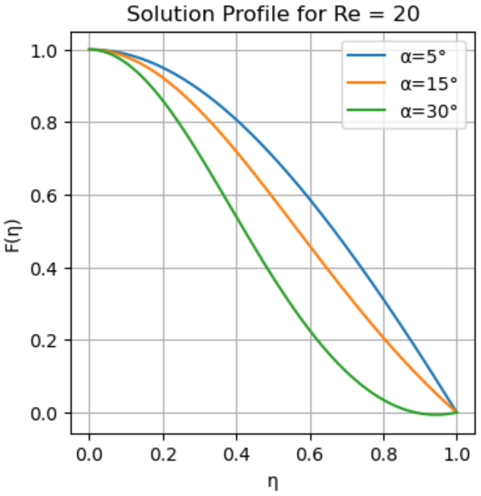

Fig. 19 Plot comparison of $F(\eta)$ for different positive angles when $Re = 20$.

4.2.2 Plot comparison of $\boldsymbol{F(\eta)}$ for different $\boldsymbol{Re}$ at fixed angles

This subsection examines the effect of increasing the Reynolds number on the average fluid velocity at a fixed angle. Contrary to initial expectations, in a divergent channel with fixed wall angles, a higher Reynolds number results in a decrease in the average fluid velocity. Furthermore, Figures 20–22 indicate that an increase in the channel's wall angle leads to a more pronounced reduction in velocity. In summary, at a specific wall angle, a higher Reynolds number corresponds to a lower average velocity, while within a fixed Reynolds number range, a larger wall angle further reduces the average velocity. These trends are quantitatively presented in Tables 5–7.

Table 5 The quantitative results for different Reynolds numbers when $\alpha = 5°$.

Re	F_{avg} (Average $F(\eta)$)	% Change (vs $Re = 5$)
5	0.659	0.0%
1·	0.652	-1.1%
20	0.637	-3.4%

Table 6 The quantitative results for different Reynolds numbers when $\alpha = 15°$.

Re	F_{avg} (Average $F(\eta)$)	% Change (vs $Re = 5$)
5	0.641	0.0%
1·	0.617	-3.7%
20	0.564	-12.0%

Table 7 The quantitative results for different Reynolds numbers when $\alpha = 30°$.

Re	F_{avg} (Average $F(\eta)$)	% Change (vs $Re = 5$)
5	0.606	0.0%
1·	0.550	-9.1%
20	0.431	-28.8%

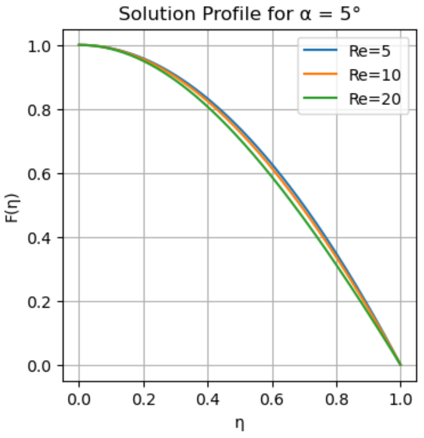

Fig. 20 Plot comparison of $F(\eta)$ for different Reynolds numbers when $\alpha = 5°$.

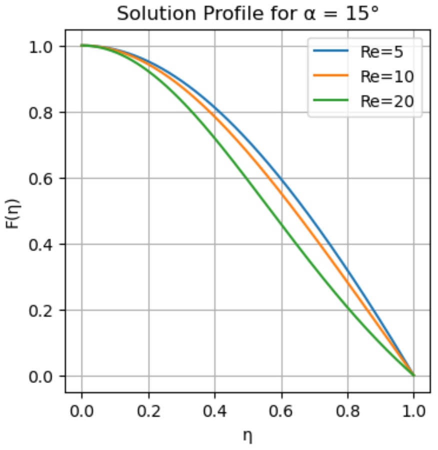

Fig. 22 Plot comparison of $F(\eta)$ for different Reynolds numbers when $\alpha = 15°$.

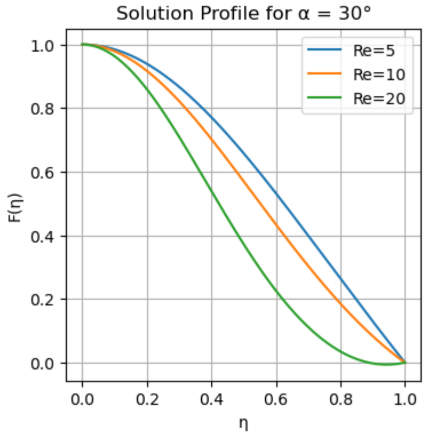

Fig. 22 Plot comparison of $F(\eta)$ for different Reynolds numbers when $\alpha = 30°$.

4.3 Impact of Reynolds number and angle of wall in a convergent channel

4.3.1 Plot comparison of $\boldsymbol{F(\eta)}$ for different negative angles at fixed $\boldsymbol{Re}$

In this subsection, a convergent channel configuration is examined. For a given Reynolds number, increasing the wall angle (i.e., increasing the magnitude of the negative angle) results in an increase in the average fluid velocity. Conversely, at a fixed Reynolds number, decreasing the wall angle leads to a reduction in the average velocity. This behavior is clearly illustrated in Figures 23–25, with corresponding quantitative results presented in Tables 8–10. Furthermore, the data indicate that the sensitivity of the average velocity to changes in the wall angle is more pronounced at higher Reynolds numbers. In other words, for a fixed channel angle, higher Reynolds numbers yield higher average fluid velocities, and the enhancement of velocity with increasing convergence becomes even more significant as the Reynolds number increases.

Table 8 The quantitative results for for different negative angles when $Re = 5$.

α (deg)	F_{avg} (Average $F(\eta)$)	% Change (vs $\alpha = -5°$)
-5	0.673	0.0%
-15	0.684	1.6%
-30	0.694	3.2%

Table 9 The quantitative results for for different negative angles when $Re = 10$.

α (deg)	F_{avg} (Average $F(\eta)$)	% Change (vs $\alpha = -5°$)
-5	0.680	0.0%
-15	0.702	3.3%
-30	0.727	7.0%

Table 10 The quantitative results for for different negative angles when $Re = 20$.

α (deg)	F_{avg} (Average $F(\eta)$)	% Change (vs $\alpha = -5°$)
-5	0.692	0.0%
-15	0.733	5.9%
-30	0.776	12.0%

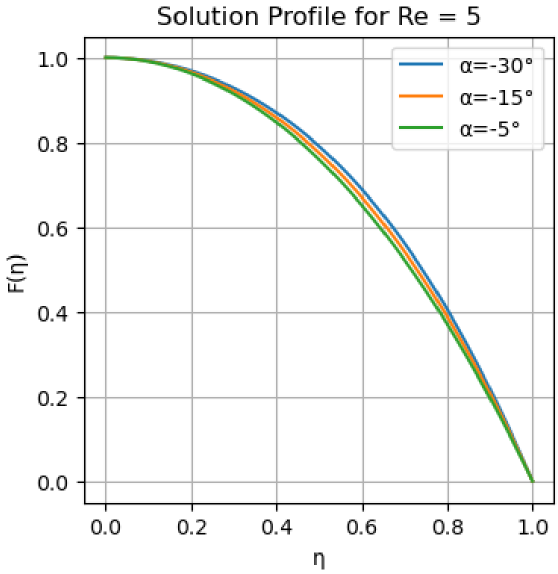

Fig. 23 Plot comparison of $F(\eta)$ for different negative angles when $Re = 5$.

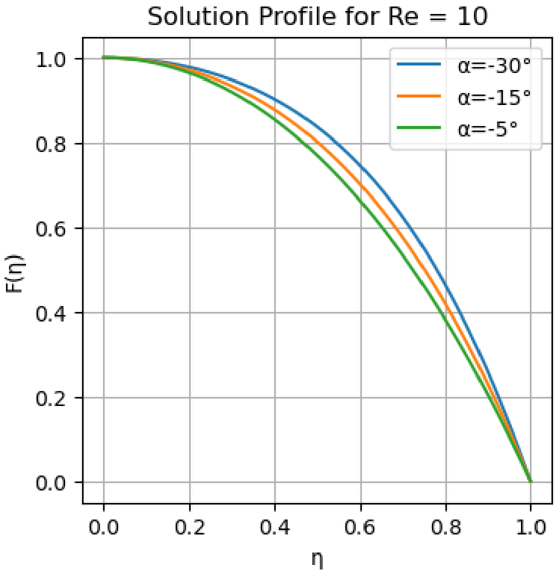

Fig. 24 Plot comparison of $F(\eta)$ for different negative angles when $Re = 10$.

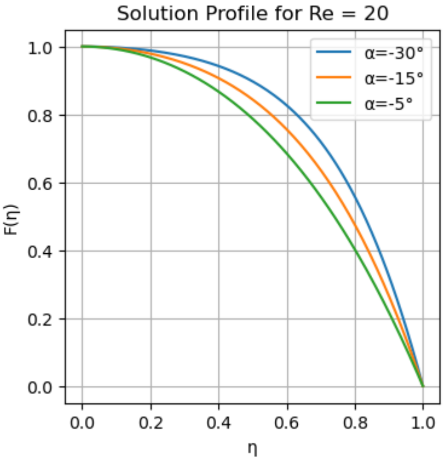

Fig. 25 Plot comparison of $F(\eta)$ for different negative angles when $Re = 20$.

4.3.2 Plot comparison of $\boldsymbol{F(\eta)}$ for different $\boldsymbol{Re}$ at fixed angles

Figures 26–28 and Tables 11–13 indicate that, in a convergent channel at a given angle, an increase in Reynolds number results in a higher velocity, in contrast to a divergent channel. Moreover, as the convergence angle (or the wall angle) increases, the average fluid velocity also increases. In summary, for a converging channel, both a larger convergence angle and a higher Reynolds number lead to an increase in the average velocity. Quantitative details of these results are provided in Tables 11–13.

Table 11 The quantitative results for different Reynolds numbers when $\alpha = -5°$.

Re	F_{avg} (Average $F(\eta)$)	% Change (vs $Re = 5$)
5	0.673	0.0%
1٠	0.680	1.0%
20	0.692	2.9%

Table 12 The quantitative results for different Reynolds numbers when $\alpha = -15°$.

Re	F_{avg} (Average $F(\eta)$)	% Change (vs $Re = 5$)
5	0.684	0.0%
1٠	0.702	2.7%
20	0.733	7.3%

Table 13 The quantitative results for different Reynolds numbers when $\alpha = -30°$.

Re	F_{avg} (Average $F(\eta)$)	% Change (vs $Re = 5$)
5	0.694	0.0%
1٠	0.727	4.7%
20	0.776	11.7%

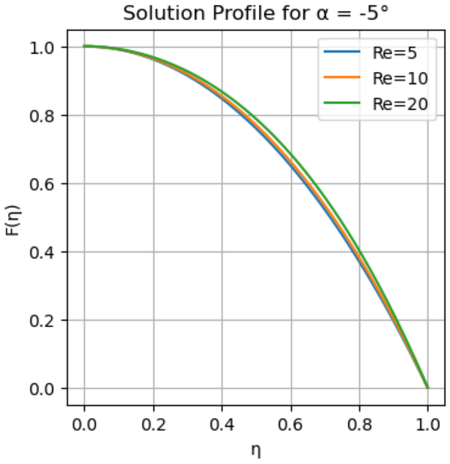

Fig. ۲26 Plot comparison of $F(\eta)$ for different Reynolds numbers when $\alpha = -5°$.

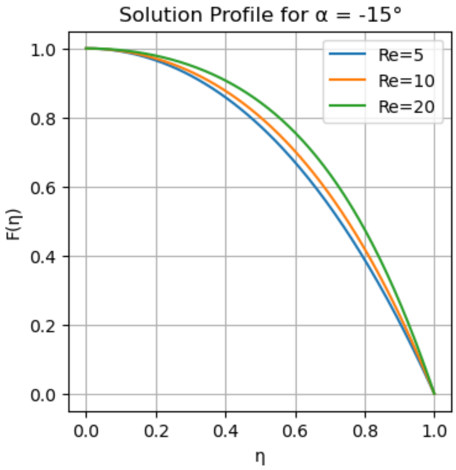

Fig. 27 Plot comparison of $F(\eta)$ for different Reynolds numbers when $\alpha = -15°$.

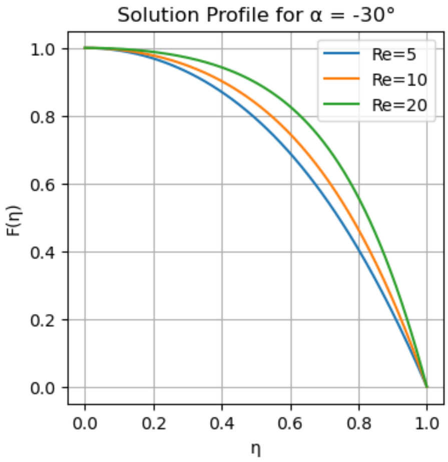

Fig. 28 Plot comparison of $F(\eta)$ for different Reynolds numbers when $\alpha = -30°$.

5 Conclusion

This study demonstrates how numerical solutions to differential equations can be refined and systematically transformed into analytical expressions through a five-step methodology of HAN method. The nonlinear ordinary differential equation (ODE) employed in this study is the Jeffery-Hamel equation, which serves as a mathematical model for fluid flow within divergent and convergent channels. The derivation of this ODE is presented in Section 2.2. To summarize the key findings of this research, the following bullet points outline the mathematical and physical conclusions derived from this study.

- Innovative Hybrid Approach: The HAN method uniquely transforms numerical solutions into analytical forms, addressing convergence issues and avoiding excessive terms in existing semi-analytical solutions.
- Flexibility in Numerical Integration: It adapts to different numerical methods when standard approaches fail, ensuring robust solutions for nonlinear differential equations.
- Systematic Five-Step Process:
    - Step 1: Propose an analytical solution (e.g., polynomial) with undetermined coefficients.
    - Step 2: Derive algebraic equations from boundary conditions (BCs).
    - Step 3: Supplement BCs with approximated conditions from numerical solutions.
    - Step 4: Derive the remaining algebraic equations from approximated BCs.
    - Step 5: Solve the system of linear algebraic equations and obtain a semi-analytical solution.
- Adaptive Boundary Conditions: Uses numerical solutions to generate additional constraints when BCs are insufficient, ensuring solvability.
- Implicit Validation: Assumes solution validity during steps 3–5 but supports accuracy via:
    - Numerical convergence checks.
    - Residual error analysis by substituting the HAN solution back into the original equation.
- Implementation & Verification:
    - Employed Runge-Kutta in Python for numerical solutions.
    - Confirmed convergence and negligible residuals to validate results.
- Reliability and Precision: Combines numerical and analytical strengths, offering concise, accurate solutions for complex problems.
- Increasing wall angles in a divergent channel leads to a decrease in average fluid velocity.
- In a divergent channel, the reduction in velocity is more pronounced at higher Reynolds numbers.
- Conversely, in a divergent channel, decreasing wall angles or approaching a configuration with approximately flat walls, increases the average fluid velocity.
- Jeffery–Hamel's equation (Eq. 20) is applicable only for convergent ($\alpha < 0$) or divergent ($\alpha > 0$) channels—not at angles of 0°, 90°, 180°, or 360°.
- At a fixed wall angle in a divergent channel, increasing the Reynolds number results in a lower average fluid velocity.
- In a divergent channel, a larger wall angle further intensifies the reduction in velocity within a given Reynolds number range.
- For a given Reynolds number, in the convergent channels, increasing the wall angle (i.e., increasing the magnitude of the negative angle) results in a higher average fluid velocity.
- Conversely, decreasing the wall angle in the convergent channels leads to a reduction in average velocity.
- In the convergent channels, the sensitivity of average velocity to wall angle variations is more pronounced at higher Reynolds numbers.
- Both a larger convergence angle and an increased Reynolds number in a convergent channel, lead to a higher average fluid velocity.

Nomenclature

Non-Greek letters

$\hat{\mathbf{r}}$	Unit vector along r-axis, (-)
r	Radial coordinate, (m)
z	Axial coordinate, (m)
$\mathbf{u}$	Velocity vector of the fluid, (m/s)
$\mathbf{F}$	Body force per unit volume, $(\mathrm{N/m^3})$
$u_r, u_r(r,\theta)$	Radial velocity component, (m/s)
$u_\theta, u_\theta(r,\theta)$	Angular velocity component, (m/s)
$p, p(r,\theta)$	Pressure distribution, (Pa)
$f(\theta)$	Dimensional function in terms of θ, ($\mathrm{m^2/s}$)
$F(\eta)$	Dimensionless form of $f(\theta)$, (-)
Re	Reynolds number, (-)
U_{char}	Characteristic velocity, (m/s)
$U_{\max}$	Maximum velocity of the fluid, (m/s)
L_{char}	Characteristic length, (m)

Greek letters

$\hat{\boldsymbol{\theta}}$	Unit vector along θ-axis, (-)
θ	Angular coordinate, (m)
ρ	Fluid density, ($\mathrm{kg/m^3}$)
μ	Dynamic viscosity, ($\mathrm{kg/m\cdot s}$)
ν	Kinematic viscosity, ($\mathrm{m^2/s}$)
α	Half-angle or angle of each wall with r-axis, (Degree or Radian)
η	Independent dimensionless similarity variable, (-)

Mathematics

$\boldsymbol{\nabla}$	Gradient operator, (unit per meter)
$\boldsymbol{\nabla}\cdot$	Divergence operator, (unit per square meter)
∇^2	Laplace operator, (unit per square meter)
$\mathrm{D}/\mathrm{D}t$	Total derivative with respect to time, (unit per second)

References

1. P. Jalili, A. Ahmadi Azar, B. Jalili, Z. Asadi, D. D. Ganji, *Case Studies in Thermal Engineering* **40** (2022)
2. P. Jalili, A. Ahmadi Azar, B. Jalili, D. Domiri Ganji, *Results Phys.* **48**, 106371 (2023)
3. P. Jalili, A. Ahmadi Azar, B. Jalili, D. Domiri Ganji, *Heliyon* **9**, e17535 (2023)
4. P. Jalili, A. Ahmadi Azar, B. Jalili, D. Domiri Ganji, *Scientific Reports* **13**, 13241 (2023)
5. B. Jalili, A. Ahmadi Azar, P. Jalili, D. Domiri Ganji, *Alex. Eng. J.* **79**, 196-226 (2023)
6. E. Ahmadi Azar, B. Jalili, A. Ahmadi Azar, M. Atazadeh, D. Domiri Ganji, *Phys. Dark Universe* **42,** 101309 (2023)
7. B. Jalili A. Ahmadi Azar, P. Jalili, D. Domiri Ganji, *Case Studies in Thermal Engineering* **52**, 103672 (2023)
8. A. Ahmadi Azar, B. Jalili, P. Jalili, D. Domiri Ganji, *Scientific Reports* **13**, 21833 (2023)
9. B. Jalili, A. Ahmadi Azar, K. Esmaeili, D. Liu, P. Jalili, D. Domiri Ganji, *Chinese Journal of Physics* **87**, 118-137 (2024)
10. P. Jalili, A. Ahmadi Azar, B. Jalili, D. Domiri Ganji, *Arab. J. Sci. Eng.* **49**, 10453-10469 (2024)
11. A. Ahmadi Azar P. Jalili, Z. P. Moziraji, B. Jalili, D. Domiri Ganji, *Heliyon* **10**, e34888 (2024)
12. B. Jalili A. Ahmadi Azar, P. Jalili, D. Liu, M. A. H.-Abdelmohimen, D. Domiri Ganji, *Case Studies in Thermal Engineering* **61**, 104859 (2024)
13. B. Jalili, A. Ahmadi Azar, D. Liu, P. Jalili, C. Kang, D. Domiri Ganji, *Phys. Fluids* **36**, 113129 (2024)
14. N. Heidari, M. de Montigny, A. Ahmadi Azar, T. Sathiyaraj, H. Hassanabadi, *Nucl. Phys. B* **1009**, 116750 (2024)
15. A. Ahmadi Azar, P. Jalili, B. Jalili, D. Domiri Ganji, *Multidiscipline Modeling in Materials and Structures* **21**, 68-97 (2025)
16. A. Ahmadi Azar, *Mechanical Engineering Advances* **3**, 2878-2878 (2025)
17. A. Ahmadi Azar, *Int. Commun. Heat Mass Transf.* **165**, Part A, 109040 (2025)
18. A. Bejan, Convection heat transfer, John wiley & sons, (2013)
19. H. Schlichting, K. Gersten, Boundary-layer theory, New York: McGraw-Hill, (2000)
20. A. A. Joneidi, G. Domairry, M. Babaelahi. *Commun. Nonlinear Sci. Numer. Simul.* **15**, 3423-3434 (2010)
21. H. S. Patel, R. Meher. *Ain Shams Eng. J.* **9**, 599-606 (2018)
22. A. Dib, A. Haiahem, B. Bou-Said, *Comput. Fluids* **102**, 111-115 (2014)
23. D. Domiri Ganji, M. Sheikholeslami, H. R. ejad., *International Scholarly Research Notices* **1**, 937830 (2011)
24. J. Singh, Y. S. Shishodia. *J. Assoc. Arab Univ.* **16**, 11-15 (2014)
25. Z. Asghar, R. S. Saif, N. Ali, *Alex. Eng. J.* **61,** 4479-4490 (2022)
26. L. Lu, J. Duan, L Fan, *Adv. Appl. Math. Mech.* **7**, 675-686 (2015)
27. L. Bougoffa., S. Mziou, R. C. Rach, *Mathematical Modelling and Analysis*, **21,** 174-187 (2016)
28. Q. Esmaili, A. Ramiar, E. Alizadeh, D. Domiri Ganji, *Phys. Lett. A* **372**, 3434-3439 (2008)
29. A. Mahmood, M. F. Md Basir, U. Ali, M. S. Mohd Kasihmuddin, M. A. Mansor, *Processes* **7**, 626 (2019)
30. U. Khan, W. Sikandar, N. Ahmed, S. T. Mohyud-Din., *Int. J. Comput. Math.* **2**, 469-483 (2016)
31. R. Meher, N. D. Patel. *SN Appl. Sci.* **1**, 656 (2019)

TTMP vol 2 (3), 2025
doi: 10.30511/TTMP.2025.2065578.1059

Transactions in Theoretical
and Mathematical Physics

On nonperturbative and relativistic corrections to the highly resonant hadronic bound states

Arezu Jahanshir[a,1]

[1] Department of Physics and Engineering Sciences, Buein Zahra Technical University, Iran

Received: 12 July 2025 / Accepted: 28 August 2025 / Published: 28 August 2025

Abstract In this article, we suggest a method for calculating the mass spectrum of a bound state with relativistic corrections. In standard calculations of mass spectra that consider the nonperturbative nature of interactions, researchers typically consider only the lowest-order term in v/c, the ratio of a particle's velocity inside the bound state to the speed of light. Using a theoretical framework based on specific mathematical techniques, we go beyond the lowest-order term in v/c approximation and define the structure of relativistic nonperturbative interaction potential by summing an infinite series in powers of v/c. Furthermore, we introduce and characterize a relativistic mass correction formulated through the current–current correlated tensor associated with two charged scalar particles in an external gauge field, where the fields obey Gaussian statistics. This two-point correlation function describes the correlation of polarization function components of the current across different spacetime points in a 4D Euclidean spacetime coordinate frame. Under relativistic conditions, this correlation structure contributes to the formation of bound states, which provide a basis for defining the constituent or relativistic mass of the particle in the bound state. Our analysis is carried out within the frameworks of quantum field theory and quantum mechanics.

1 Introduction

The relativistic and nonperturbative effects in nuclear and hadronic interactions are important and interesting subjects that, from the past to the present, have been actively studied [1–5]. Traditionally, nuclear and particle physics focus on the structure and interactions of relativistic systems composed of protons, neutrons, and hadrons [6–9]. These fermionic particles consist of quarks bound together by the strong force, and such systems are described by quantum chromodynamics (QCD). As experimental and theoretical tools have developed, the field has progressed toward hadronic physics, which studies the properties and dynamics of quarks bound and interacting with gluons, including heavy bottomonium [10]. Hadronic physics attempts to determine and understand how quarks and gluons form and bind in bound states, how confinement arises, how relativistic and ultra-relativistic velocities affect a system, and how mass and spin describe the behavior of heavy, highly hadronic resonant states from QCD dynamics. It is generally accepted that traditional potential models focus on nonrelativistic approximations and first-order perturbative expansions in v/c. These models are useful for describing nuclear physics and light hadronic bound states [10]. However, the heavy, highly resonant states and long-range gluonic interactions of bottomonium bound states require corrections beyond the leading order to capture the fine structure and decay behavior that occur when the system is under strong coupling and relativistic dynamics. Bottomonium can be modelled as systems of point-like quarks interacting in a gauge field governed by QCD, according to the framework of quantum field theory (QFT). While potential models have proven successful in describing many properties and characteristics of heavy quarkonium spectra, most approaches are fundamentally limited by their nonrelativistic conventions and neglect of dynamical gluon and relativistic potential effects [11]. Early studies of relativistic corrections in light and heavy hadronic bound states used relativistic potential models such as Dirac-based or Bethe–Salpeter approaches, as well as effective field theories like nonrelativistic quantum chromodynamics (NRQCD) [12, 13], which describe heavy quark–antiquark systems by expanding QCD in the lowest order of v/c, assuming that the particle mass is much larger than the QCD scale (Λ_{QCD}). Researchers have included relativistic corrections and color contributions in the bound states, and sometimes derived bound-state behaviors from potential NRQCD models (pNRQCD), which lead to Schrödinger-like

---

[a] e-mail: jahanshir@bzte.ac.ir

equations with the potential derived from QCD, representing both perturbative and nonperturbative effects. In addition, systems using lattice QCD to capture nonperturbative effects have been studied. Therefore, based on recent results and theoretical suggestions for future experiments at the LHC, Super KEKB (Belle II), ALICE, LHCb, CMS, and ATLAS, the proposed relativistic corrections on properties of the exotic highly resonant states of heavy bottomonium (HRSB) can be very important and useful [14–16]. Bottomonium systems have a large mass and might not seem to require investigation of relativistic effects, although their highly resonant behavior makes them an interesting subject for studying relativistic corrections and their effects on the mass and the relativistic nonperturbative interaction potential. Different from the spin interaction potentials, and at high energies, relativistic corrections to the potential and mass must also be taken into account. The presented theoretical approach on the relativistic corrections in understanding nonperturbative relativistic terms of Hamiltonian interactions in strong interactions and defining quark dynamics, decay rates, and properties can be useful. This model for analyzing interaction mechanisms in extreme temperature environments, such as quark–gluon environments, neutron stars, and compact stars, can also be considered. According to the clarification above, we will use combined methods to identify the relativistic corrections on the HRSB bound states. First, the mass spectrum of the HRSB of the bottom–antibottom bound state in the framework of QFT and analogous to quantum mechanics (QM) based on the Green function (GF) in the form of the Feynman functional integral (FPI) and path integral methods [17–19], with a given interaction potential, will be presented. The mass spectrum of the bottom–antibottom bound state within relativistic corrections, based on the long-range behavior of the current–current correlation tensor (polarization function (PF) or polarization tensor) for scalar charged bottom–antibottom quarks in the excited state with a specified orbital quantum number ℓ in a background gauge field $A(x)$, is completely described and explained. The relativistic correction to the interaction behaviors under a given potential was analytically determined. Additionally, the relativistic correction to the mass, which is interpreted as the constituent masses of the bottom–antibottom charged quarks, will be logically calculated, taking into account a specified orbital quantum number ℓ. We can also introduce the effects of the full spin interactions, including spin–spin, spin–orbit, and tensor spin Hamiltonians.

$$H_{\text{int}} = H_0 + H_{\text{pert}} + H_{\text{nonpert}} + H_{SS} + H_{LS} + H_{TT}. \tag{1}$$

Into the bound state mass spectrum equation, one would typically add the Breit–Fermi Hamiltonian. However, since the goal of this paper is to describe the relativistic corrections on mass and the nonperturbative relativistic interaction potential, the Breit–Fermi Hamiltonian has been omitted. Hence, we present an alternative method to describe the properties of HRSB. In this article, equations are written in natural units with $\hbar = c = 1$, and the mass spectrum is calculated in units of GeV. We used computational coding in MATLAB R2021a software, and HRSB $10s$: $\Upsilon(11020)$ mass spectrum calculations were performed in Microsoft Office Excel 2021 software. This paper is organized as follows. In Sect. 2, the determination of the mass spectrum and constituent mass of bottom–antibottom quarks of the HRSB under relativistic corrections within QM and QFT principles is defined. In Sect. 3, the details of the relativistic nonperturbative term of the interaction potential, along with the definition and calculation method based on mathematical physics principles for the HRSB, are described.

2 The mass spectrum including relativistic correction

We present the asymptotic properties of the interaction of two scalar charged particles through the polarization function (PF) and then evaluate functional integrals under a variational technique to analyze the bound state system of these particles [20]. A four-dimensional Euclidean spacetime coordinate frame $x = (\bar{x}, x_0)$ with imaginary time defined as $x_0 = it$, based on field conditions to define the PF and Green function (GF), is considered. We assume that the annihilation channel is neglected, i.e., no particle–antiparticle annihilation channels can be created. Then, we define the solutions using the functional integral formalism and average over the external Gaussian gauge field $A(x)$. The averaging over the field with the polarization function $\Pi(x; y)$ is indicated. To extract the PF in the asymptotic limit, we employ the variational approach, which allows us to describe the effects of relativistic behaviors in the interaction of two charged scalar particles within an external gauge field. The results of these mathematical definitions provide a representation of the nonperturbative interaction term under relativistic conditions in high-energy physics. Now, we obtain formulae that give the mass spectrum of an HRSB of bottom–antibottom as charged scalar particles interacting in an external gauge field $A(x)$. We focus on the mechanism of HRSB formation and the estimation of the contributions from potential and nonpotential interactions. In the standard form, the interaction of a quark in an external gauge field is written with the spinor field equation (Dirac equation).

$$\left[(i\gamma^{\alpha}\partial_{\alpha} - g\gamma^{\alpha}A_{\alpha}(x)) - m\right]\Psi(x) = 0. \tag{2}$$

Owing to the importance of spin effects, g is the coupling constant [18, 20]. As mentioned in the introduction, in this paper, our focus is on nonperturbative relativistic corrections (NRC) of the potential and mass; therefore, the spin interaction is not considered, and we describe the quark behavior as a scalar particle and investigate the constrained interaction with the Klein–Gordon equation.

$$\left[(i\partial_\alpha + gA_\alpha)^2 + m^2\right]\phi(x) = 0. \tag{3}$$

Now, we consider the interaction between the bottom quark with mass m_1 and the antibottom quark with mass m_2, which together form a localized bottomonium bound state in the external gauge field $A(x)$. Considering the concept of a localized and nonlocalized interaction, included in $W(x; y)$, the Green's function (GF) for this system can be written as

$$\begin{aligned}\Big[\big(i\partial_\alpha + gA_\alpha(x)\big)^2 + m_1^2 \\ + \big(i\partial_\alpha + gA_\alpha(y)\big)^2 + m_2^2 + V(x; y)\Big]\, G(x; y) \\ = \delta^{(4)}(x-y).\end{aligned} \tag{4}$$

It is widely recognized that the Green's function (GF) is a special solution to a differential equation characterized by the Dirac delta function $\delta^{(4)}(x-y)$, and it describes how the bottom and antibottom quarks respond to a localized disturbance in the gauge field within the interaction potential $W(x; y)$ [18, 21]. Depending on the localization of the interaction, the local density of scalar The local density of scalar particles can be expressed by a "current" in a nonrelativistic $4D$ Euclidean spacetime coordinate frame $x = (\vec{x}, x_0)$ with imaginary time $x_0 = it$. Euclidean formulations are particularly convenient when the annihilation channel is neglected, i.e. no particle–antiparticle annihilation is included. For the two-point correlator, especially when studying the correlation Green's function, it is advantageous to use scalar densities to construct observables, probe local scalar gauge-field behavior, and simplify bound-state calculations in the absence of annihilation. Hence, one can define the current in correlators and effective sources of bottom–antibottom charged quarks in the form [20, 23]

$$J(x, y) = \Phi^-(x)\,\Phi^+(y). \tag{5}$$

Here $\Phi^+(y)$ is the creation operator and $\Phi^-(x)$ is the annihilation operator. This current $J(x)$ can act as an effective source in the bottomonium bound state and yields the two-point correlation function

$$\begin{aligned}&\langle 0|\widehat{T}(J(x)\,J(y))\,|0\rangle \\ &\quad = \langle 0|\widehat{T}\big(\Phi^-(x_1)\Phi^+(y_1)\,\Phi^-(x_2)\Phi^+(y_2)\big)\,|0\rangle.\end{aligned} \tag{6}$$

Here x_i denotes the point where the particle is annihilated and y_i the point where the bottom–antibottom quarks are created, while τ represents the proper time. The operator $\widehat{T}$ is the time–ordering operator, and we write $x = (\vec{x}, x_0)$, $y = (\vec{y}, y_0)$. In QFT and QM, the transformed propagator function (quantum amplitude) of the initial and final states of the bound state in the background gauge field A is connected by the Hamiltonian according to

$$G(x; y\,|\,A) = \langle x|e^{-i\widehat{H}t}|y\rangle. \tag{7}$$

That is, the amplitude for a particle to evolve from position y to position x in time t, governed by the Hamiltonian $\widehat{H}$. Therefore, the Green's function (GF) based on the two-point correlation function for the bottom–antibottom bound state is written as

$$G(x; y) = \langle 0|T\big(\Phi^-(x_1)\Phi^+(y_1)\,\Phi^-(x_2)\Phi^+(y_2)\big)\,|0\rangle. \tag{8}$$

The GF defines the amplitude for bottom–antibottom quarks through a four-point function that propagates from y_i to x_i in the bottomonium bound state [20]. The interaction of bottom–antibottom quarks in the external gauge field A is described by averaging all transformed propagators over the external field using the polarization-function (PF) formalism as follows:

$$\begin{aligned}\Pi(x; y) &= \langle J(x_1; y_1)\, J(x_2; y_2)\rangle \\ &= \langle \Phi^-(x_1)\Phi^+(y_1)\,\Phi^-(x_2)\Phi^+(y_2)\rangle \\ &= \big\langle G_1(x_1; y_1\,|\,A_\alpha)\, G_2(x_2; y_2\,|\,A)\big\rangle_A.\end{aligned} \tag{9}$$

As is commonly known in QFT and QM, one determines the properties of a particle of mass m under all possible configurations of interaction by evaluating the propagator.

$$D(x; y) = \int \left(\frac{dk}{2\pi}\right)^4 \widetilde{D}(k^2)\, e^{ik\cdot(x-y)}. \tag{10}$$

This formalism allows us to define the amplitude for the bottom–antibottom bound state to propagate from a relative separation y and the center-of-mass position x in the form

$$D(x; y) = \int \left(\frac{dp}{2\pi}\right)^4 \left(\frac{dk}{2\pi}\right)^4 \widetilde{D}(p, k)\, e^{ip\cdot x}\, e^{ik\cdot y}. \tag{11}$$

Here x is the center-of-mass coordinate, y is the relative coordinate, and $\widetilde{D}(p,k)$ is the propagator of the bottom–antibottom bound state with total momentum p and internal momentum k. The function $D(x;y)$ can be used to determine the bottomonium bound-state mass M. In QFT, the polarization function decays exponentially based on the spectral representation formalism in Euclidean space, given by

$$\begin{aligned}\Pi(x;y) &= |\langle 0|J(x;y)|n\rangle|^2 \; e^{-xE_n} \\ &= |\langle 0|J(x;y)|n\rangle|^2 \; e^{-xM_n}. \end{aligned} \tag{12}$$

where $\langle 0|$ denotes the vacuum state, $|n\rangle$ is the nth state, E_n is the energy of the nth state (E_n being the energy eigenvalue of the Schrödinger equation, as will be explained in Section 3), and M_n is the corresponding mass. This representation of the polarization function leads to the calculation of the mass spectrum of the bottom–antibottom bound state [20]. Hence, if we consider that both bottom–antibottom quarks are created at the same spacetime point (the origin) and propagate to $y = y_1 - y_2$, and are annihilated at x_1 and x_2 respectively, then the polarization function at final positions, depending on their relative separation $x = x_1 - x_2$, with a normalization constant $C = |\langle 0|J(x)|n\rangle|^2$ reads

$$\Pi(x) = \int \left(\frac{dp}{2\pi}\right)^4 \frac{e^{\,ip\cdot x}}{p^2 - M^2 + i\varepsilon} = C\, e^{-M|x|}\,. \tag{13}$$

Now, we consider the path integral formalism because of its powerful theoretical benefits in QM and QFT. The Feynman path integral (FPI) representation provides a useful method for describing bound states by averaging over all possible ways to create a bound state, i.e., both classical and quantum paths. It has become one of the most essential formalisms in which operator methods are rendered practical for quantizing gauge theories under QCD [16, 17]. We consider the interaction between a bottom quark with mass m_1 and an antibottom quark with mass m_2. These states form a localized bottomonium bound state in the external gauge field $A(x)$. The bottomonium bound state contains both localized and nonlocalized interactions $V(x;y)$. To better understand the mathematical formulation of the FPI, we begin by formulating it for a single charged particle in an external gauge field. This property of localized and nonlocalized behavior illustrates the roles of proper time, gauge coupling, and quantum fluctuations. In this section, we extend the formalism to the case of two interacting particles, incorporating both individual gauge interactions and the mutual interaction potential. Therefore we first represent the GF in a $4D$ Euclidean spacetime coordinate frame for a charged bottom quark in an external gauge field $A(x)$ in the form of the FPI formalism. Let us consider GF satisfies

$$\left[(i\partial_\alpha + A)^2 + m^2\right] G(x;y\,|\,A) = \delta^{(4)}(x;y). \tag{14}$$

And then, introducing variables s and τ, one can represent the GF in the form of the FPI as

$$\begin{aligned} G(x;y\,|\,A) &= \int_0^\infty ds\; e^{-sm^2}\,\widehat{T}_\tau \\ &\quad \times \exp\left[-s\int_0^1 d\tau \left(\tfrac{\partial}{\partial x(\tau)} + A(x(\tau))\right)^2\right] \\ &\quad \times \delta^{(4)}(x-y) \\ &= \int_0^\infty ds\; e^{-sm^2} \int d\varphi(\tau) \\ &\quad \times \exp\left[-\int_0^1 d\tau\, \varphi^2(\tau)\right. \\ &\qquad\qquad \left. + \,2i\sqrt{s}\int_0^1 d\tau\, \varphi(\tau)A(z')\right] \\ &\quad \times \delta^{(4)}(z). \end{aligned} \tag{15}$$

where

$$z' = x - 2\sqrt{s}\int_0^1 d\tau'\, \varphi(\tau'), \tag{16a}$$

$$z = x - y - 2\sqrt{s}\int_0^1 d\tau\, \varphi(\tau). \tag{16b}$$

where $\varphi(\tau)$ is the path or trajectory of the quark and is a functional integration variable over paths, $x(\tau)$ is the physical trajectory, $\widehat{T}_\tau$ is the proper-time ordering or time-ordering operator, the variable $s : 0 \preceq s < \infty$ is an auxiliary parameter introduced by Schwinger's proper time to define the propagator $1/(p^2 - M^2)$ and it controls the damping factor e^{-sm^2}, while τ, τ' are proper times describing the relative motion of the two particles at different spacetime points with $\tau = \tau_1 - \tau_2$. The proper time is the time interval measured by a clock moving with the particle and it remains invariant in all inertial frames, while the fourth component of spacetime x_0 provides the direction in spacetime in which the particle is moving. In functional integral notation, the parameter s is a computational tool to write path integrals more conveniently; it is not a physical real time in spacetime coordinates and is not an observable. The dimensionless parameters τ and τ' with $0 \preceq (\tau, \tau') \preceq 1$ are the proper times along the given path and parameterize the position along the quark's trajectory $x(\tau)$, and the normalization parameter reads [20, 22].

$$C = \int d\varphi(\tau)\, \exp\left[-\int_0^1 d\tau\, \varphi^2(\tau)\right]\, \delta^{(4)}(z')$$
$$= \int \left(\frac{dk}{2\pi}\right)^4 \exp\left[-ikx - sk^2\right]$$
$$= \left(\frac{1}{4\pi s}\right)^2 \exp\left(-\frac{x^2}{4s}\right). \qquad (17)$$

And then, introducing variables s and τ, one can represent GF in the form of FPI by way of

$$G(x;y\,|\,A) = \int_0^\infty \left(\frac{ds}{4\pi s}\right)^2 \exp\left(-sm^2\right)$$
$$\times \exp\left(-\tfrac{(x-y)^2}{4s}\right)\, \mathcal{R}(x;y\,|\,A), \qquad (18)$$

And the kinetic term of the given path is included in

$$\mathcal{R}(x;y\,|\,A) = \int d\sigma\, J(x;y\,|\,A)$$
$$= \int d\sigma\, \exp\left[i \int_0^1 d\tau\, N(\tau)\, A\big(N'(\tau)\big)\right]. \qquad (19)$$

where $x(\tau)$ is the fluctuation of the trajectory in the spacetime coordinate of the bottom quark, defined as a function of the proper time τ under Dirichlet boundary conditions $x(0) = x(s) = 0$, which describe fixed start and end points. The derivative $\dot{x}(\tau)$ denotes the velocity of the fluctuating path along the trajectory of the bottom quark. The auxiliary functions $N(\tau) = x - y - 2\sqrt{s}\,\theta(\tau)$ and $N'(\tau) = x\tau + y(1-\tau) + 2\sqrt{s}\,\theta'(\tau)$ describe the full path of the bottom quark, i.e. the position of the quark at proper time τ along its worldline between the spacetime points x and y [22]. The relation $\int d\sigma = 1$ plays the same role as the normalization of a probability distribution $\int dP = 1$, ensuring that the total measure of integration is normalized to unity. Now, using the Green's function in the form of Eq. (18) together with these new variables, and after some algebra, we consider averaging over the field restricted to two Gaussian correlators.

$$\left\langle \exp\left[i \int dx\, A(x)\, J(x)\right]\right\rangle_A$$
$$= \exp\left[-\tfrac{1}{2} \int dx \int dy\; J(x)\, D(x;y)\, J(y)\right], \qquad (20)$$

where the propagator of the gauge field $D(x;y)$ reads

$$D(x;y) = \langle A(y)A(x)\rangle_A = \partial^2 \mathcal{D}_1(x;y) + \delta\, \check{\mathcal{D}}(x;y). \qquad (21)$$

Hence, if we consider that both bottom–antibottom quarks are created at the same spacetime point (the origin) and propagate to $y = y_1 - y_2$, and are annihilated at x_1 and x_2 respectively, then the polarization function at the final positions depends on their difference $x = x_1 - x_2$. We can then define the asymptotic behavior ($|x| \to \infty$) of the polarization operator $\Pi(x) = \langle G_1\, G_2\rangle_A$, which describes the interaction between bottom–antibottom charged quarks of masses m_1 and m_2 that form a localized bottomonium bound state in the external gauge field $A(x)$ and interact through a nonlocal potential $V(\mu_1,\mu_2)$, as follows:

$$\Pi(x|A) = \int_0^\infty \int_0^\infty \frac{d\mu_1\, d\mu_2}{(8\pi^2 x)^2}$$
$$\times \exp\left[-\tfrac{|x|}{2} \sum_{i=1}^{2} \left(\tfrac{m_i^2}{\mu_i} + \mu_i\right)\right] V(\mu_1,\mu_2). \qquad (22)$$

The function $V(\mu_1,\mu_2)$ resembles the Feynman path integral (FPI) in $4D$ nonrelativistic quantum mechanics for particles with masses μ_1 and μ_2 moving with velocities v_1 and v_2 within nonlocal and local interaction potentials [20, 23]. The total interaction is therefore expressed as $V(\mu_1,\mu_2)$. Thus, based on QFT, m_1 and m_2 are the current masses of these particles, while μ_1 and μ_2 denote the constituent masses, and the corresponding Schrödinger equation takes the form

$$\left(\frac{\hat{p}_1^2}{2\mu_1} + \frac{\hat{p}_2^2}{2\mu_2} + V(\mu_1,\mu_2)\right)\Psi = E(\mu_1,\mu_2)\,\Psi. \qquad (23)$$

We will describe this equation in detail at the end of this section and in the next section, where we will derive the relativistic nonperturbative potential term from it. Thus, with the nonrelativistic formulation of the FPI in $4D$ nonrelativistic quantum mechanics, by comparing the functional $V(\mu_1,\mu_2)$ obtained from the relativistic Green's function in Eq. (22), we establish the definition of the variational parameters μ_1 and μ_2 [20, 23, 24]. In this formalism, μ_1 and μ_2 represent the constituent masses of quarks in the bound state, i.e. the relativistic mass of the moving charged quarks. The functional in Eq. (22), based on Eq. (13) in the asymptotic limit, reads

$$M = \lim_{|x|\to\infty} \left(-\frac{1}{|x|}\, \ln(\Pi(x|A))\right). \qquad (24)$$

Thus, the functional integral $\Pi(x|A)$ is determined by a saddle-point technique [20, 22, 25] in the FPI representation and gives the lightest intermediate bound-state mass spectrum of bottom–antibottom charged quarks with $m_1 = m_2 = m_b$ and $\mu_1 = \mu_2 = \mu_b$ at the large-distance decay $|x| \to \infty$, within the interaction potential $V(\mu_b, \mu_{\bar{b}})$ in the form of.

$$M = \min_{\mu_b}\Big[\frac{m_b^2}{\mu_b} + \mu_b + E(\mu_b)\Big], \tag{25}$$

where the constituent mass of the bottom quark in the bound state, i.e. the relativistic mass of the quark inside the bottomonium bound state within the interaction potential, is determined by minimizing Eq. (25) as follows:

$$2\mu_b^2\,\frac{\mathrm{d}E(\mu_b)}{\mathrm{d}\mu_b} + \mu_b^2 - m_b^2 = 0. \tag{26}$$

m_b is the mass of the free bottom quark, the reduced mass of the system is $\mu = \frac{\mu_1\mu_2}{\mu_1+\mu_2} = \frac{\mu_b}{2}$, and $E(\mu)$ is the relativistic energy of the bottom–antibottom bound state within the interaction potential under the external gauge field. Using the reduced mass μ of bottomonium, we can define the mass spectrum M and the constituent mass μ_b of HRSB in the form of

$$M = \left(4m_b^2 - 8\mu\,\frac{dE(\mu)}{d\mu}\right)^{1/2} + \mu\,\frac{dE(\mu)}{d\mu} + E(\mu), \tag{27}$$

and

$$\mu_b = \left(m_b^2 - 2\mu\,\frac{dE(\mu)}{d\mu}\right)^{1/2}. \tag{28}$$

If we represent the Schrödinger equation of two particles with masses μ_1 and μ_2 in the nonrelativistic form, these constituent masses of particles in the bound state represent the relativistic correction on mass in the $4D$ Euclidean spacetime coordinate with the reduced mass defined as $\frac{1}{\mu} = \frac{1}{\mu_1} + \frac{1}{\mu_2}$, and then the term $E(\mu)$ can be considered as the eigenenergy of the equation $H\Psi = E(\mu)\Psi$ that determines the mass spectrum of the bound state under the relativistic correction on mass.

3 Relativistic nonperturbative interaction potential

In the study of highly resonant states of heavy quarkonia, to describe their structure and dynamics, especially HRSB states such as $\Upsilon(10860)$, $\Upsilon(11020)$, and $\Upsilon(10750)$. These states are formed under a strong coupling constant g that becomes large and perturbative QCD breaks down, and hence, including nonperturbative terms of the interaction Hamiltonian is necessary [21]. The interaction between bottom–antibottom quarks is dominated by long-range nonperturbative effects rather than short-range gluon exchange with a string tension constant σ. These effects include vacuum structure, symmetry-breaking signature, nonzero vacuum expectation value of quarks and gluons (quark condensate and gluon condensate in QCD theory), spontaneous chiral symmetry breaking, coupled channel dynamics, gluon condensations, field couplers, and power-suppressed corrections. Thus, the interactions of Hamiltonian terms in HRSB cannot be described by the perturbative behavior of the potential model $H = H_0 + \lambda H_p$. Owing to the importance of explaining the mass displacement, decay width, and resonance structures of hadronic states in experimental data, the usual quark potential models often do not take these phenomena into account. This break requires the use of nonperturbative formalism such as QCD pair-creation mechanism, screened potentials, effective field theories, or the transition matrix (T–Matrix) of a scattering process. These frameworks allow us to describe the mass spectrum, energy eigenvalues, and decay properties of HRSB states, which are completely under the relativistic effects. Therefore, nonperturbative relativistic corrections under nonperturbative potential and mass in the Hamiltonian are necessary to understand the HRSB behaviors. The relativistic mass correction was introduced in the previous section. In this section, we extract the relativistic nonperturbative Hamiltonian of the interaction potential from the functional $V(\mu_b, \mu_{\bar{b}})$ in Eq. (22) of the bottom–antibottom quark bound state polarization function. Eq. (22) presents a GF in the form of FPI when bottom–antibottom quarks with the constituent masses μ_b and $\mu_{\bar{b}}$ interact via a local and nonlocal potential, including inside function.

$$V(\mu_b, \mu_{\bar{b}}) = V_{bb} + V_{\bar{b}\bar{b}} - V_{b\bar{b}} - V_{\bar{b}b}, \tag{29}$$

in a $4D$ Euclidean spacetime coordinate frame with imaginary time $x_0 = it$, where $m_b, m_{\bar{b}}$ are the current masses of bottom–antibottom quarks. The functions $V_{bb}, V_{\bar{b}\bar{b}}$ contain the self-energy diagram interaction potential of the bottom–antibottom quarks with themselves under constituent masses $\mu_b, \mu_{\bar{b}}$. Functions $-V_{b\bar{b}}, -V_{\bar{b}b}$ describe the interaction potential via a dynamical internal gauge field mediating the interaction between the bottom–antibottom quarks of the constituent masses μ_1 and μ_2. Therefore, based on the interaction potential formalism, functions $V_{bb}, V_{\bar{b}\bar{b}}$ correspond to non-potential interactions, while functions $-V_{b\bar{b}}, -V_{\bar{b}b}$ determine the contribution to the mass renormalization of the bottom–antibottom quarks, and correspond to the potential interaction. Thus, we can consider that the functional $V(\mu_1, \mu_2)$ contains all imaginable and achievable types of scattering diagrams or virtual particle exchange diagrams. At this stage, we use the interaction potential relation in the asymptotic behavior of the polarization function, Eq. (22), which depends on the energy eigenvalue in QFT under the spectral representation formalism in the Euclidean space, which is defined as follows

$$\begin{aligned}\lim_{|x|\to\infty} V(\mu_b,\mu_{\bar b}) &= C\,\exp\big[-x\,E(\mu_b,\mu_{\bar b})\big]\\ &= C\,\exp\big[-x\,E(\mu)\big],\end{aligned}\tag{30}$$

where $E(\mu)$ is the energy eigenvalue of the Schrödinger equation, which depends on μ_b, $\mu_{\bar b}$, m_b, $m_{\bar b}$, and also on the interaction constant g of the HRSB bound state. Now, we start from the total interaction potential in Eq. (22). The functional $V(\mu_b,\mu_{\bar b})$ in the FPI form is

$$\begin{aligned}V(\mu_b,\mu_{\bar b}) = &\iint N\,dx_{0b}\,dx_{0\bar b}\\ &\times \exp\left[-\int d\tau \sum_{i=b,\bar b}\frac{\mu_i}{2}\,\dot z_i(\tau)^2\right]\\ &\times \exp\Big[V_{bb}+V_{\bar b\bar b}-V_{b\bar b}-V_{\bar b b}\Big].\end{aligned}\tag{31}$$

and integration is performed over the $4D$ Euclidean spacetime coordinate frame $x_b=(\bar x_b, x_{0b})$, $x_{\bar b}=(\bar x_{\bar b}, x_{0\bar b})$. Because the trajectories of the bottom–antibottom quarks are considered in the $4D$ spacetime with the imaginary time $x_0=it$, where the particle point is (x,y,z,x_0), this allows us to define the interaction potential that contains corrections associated with nonperturbative, relativistic, and nonlocal characteristics of the correlations and scattering processes. The reason for the $4D$ spacetime choice is that the particle location in the $4D$ Euclidean spacetime frame is $(x,y,z,x_0)\longrightarrow(x,y,z,it)$, and using this coordinate, the vacuum expectation values of time-ordered products of field operators and Green's functions exhibit covariant behavior in nonperturbative regimes. Considering the Wick rotation method of finding a solution in (x,y,z,it) from a solution to a related problem in (x,y,z,x_0), the FPIs appear in the action under the function e^{iS}; with the transformation $x_0\longrightarrow it$, the action S becomes real and the FPI transforms as $\int\mathcal{D}\varphi\,e^{iS}\longrightarrow\int\mathcal{D}\varphi\,e^{-S}$, i.e. the FPI functional becomes exponentially damped, allowing for convergent calculations. Therefore, if integration over the proper times τ_1 and τ_2 in the FPI formalism is neglected, bottomonium bound states reduce to nonrelativistic systems and are described by the Schrödinger equation $\hat H\Psi=E(\mu)\Psi$ represented by Eq. (49).

As described in Eq. (12) and Eq. (30), the desired term $E(\mu_b,\mu_{\bar b})=E(\mu)$ is the energy eigenvalue of the Schrödinger equation [26]. It is widely recognized that QCD is formulated in $4D$ spacetime, and by nonrelativistic conditions we mean that one can expand the relativistic Lagrangian in powers of v/c or p/m, integrate over high-energy modes, and consider effective theories to describe hadronic bound states. These conditions in $4D$ spacetime describe the behavior of bottom–antibottom quarks with slow velocity ($v/c\sim 0.1-0.3$) under the nonrelativistic limit, where relativistic effects such as time dilation, length contraction, and mass–energy equivalence become negligible. In contrast, due to the heavy mass of bottom–antibottom quarks and their small relative velocity compared to the speed of light, HRSB states display relativistic and nonperturbative effects arising from the larger spatial separation between the bottom–antibottom quarks compared to ground states, such that the bound state extends to the long-distance asymptotic regime of QCD, where the strong coupling constant g becomes large and perturbation theory ceases to apply. Moreover, topological fluctuation effects cannot be described by Feynman diagrams or perturbative expansions. Considering this explanation of HRSB, we now start to derive the nonperturbative relativistic potential from Eq. (31). In QFT and particle physics, nonperturbative relativistic corrections to the interaction Hamiltonian are important and determined using an approximate correction to the lowest order of v/c. In this section, we extract an additional nonperturbative relativistic approach using some practical suggestions from the interaction process and the behavior of the $4D$ spacetime term based on integrating over the proper times τ_b and $\tau_{\bar b}$ of the bottom–antibottom charged quarks. In Eq. (31), we divide the fourth spacetime coordinates x_{0b} and $x_{0\bar b}$ (where the proper times are τ_b and $\tau_{\bar b}$) and define potential terms in three separated parts of the vacuum interaction: (1) a potential term (the nonrelativistic potential of interaction between particles with the gauge field), (2) a nonperturbative term, and (3) a nonperturbative relativistic term, i.e.

$$-V_{b\bar b}, -V_{\bar b b} = V_{\text{nonrel}}+V_{\text{nonpert}}+V_{\text{rel}}.\tag{32}$$

To define the nonperturbative relativistic part of the interaction, we have to integrate over proper time in Eq. (31); hence, we consider the constant of interaction to be small based on the perturbative interaction formalism, and this allows us to integrate over proper time. We consider this form of interaction potential because the standard and useful solution of the functional $V(\mu_b,\mu_{\bar b})$ in QFT is absent. Now, we start the representation of the nonperturbative relativistic interaction potential of HRSB. The functional of the total interaction $V(\mu_b,\mu_{\bar b})$ contains the components $V_{bb}+V_{\bar b\bar b}-V_{b\bar b}-V_{\bar b b}$ that read

$$\begin{aligned}V_{bb} = &\frac{g^2}{2}\int_0^t\int_0^t d\tau_b\,d\tau_{\bar b}\\ &\times \dot z^{(b)}(\tau_b)\,\mathcal{D}\Big(z^{(b)}(\tau_b)-z^{(b)}(\tau_{\bar b})\Big)\,\dot z^{(b)}(\tau_{\bar b}).\end{aligned}\tag{33}$$

$$V_{\bar{b}\bar{b}} = \frac{g^2}{2}\int_0^t\int_0^t d\tau_b d\tau_{\bar{b}} \\ \times \dot{z}^{(\bar{b})}(\tau_b)\,\mathcal{D}\Big(z^{(\bar{b})}(\tau_b) - z^{(\bar{b})}(\tau_{\bar{b}})\Big)\,\dot{z}^{(\bar{b})}(\tau_{\bar{b}}). \tag{34}$$

$$V_{b\bar{b}} = V_{\bar{b}b} = \frac{g^2}{2}\int_0^t\int_0^t d\tau_b d\tau_{\bar{b}} \\ \times \dot{z}^{(b)}(\tau_b)\,\mathcal{D}\Big(z^{(b)}(\tau_b) - z^{(\bar{b})}(\tau_b)\Big)\,\dot{z}^{(\bar{b})}(\tau_{\bar{b}}). \tag{35}$$

where function $z^{(b)}(\tau_b)$ and $z^{(\bar{b})}(\tau_{\bar{b}})$ describe how the trajectory contributes to the propagator structure under relativistic corrections and are defined by $z^{(b)}(\tau_b) = (x_b - x_{\bar{b}})\tau_b + x_{\bar{b}} - 2B(\tau_b)\sqrt{s}$ and $z^{(\bar{b})}(\tau_{\bar{b}}) = (x_b - x_{\bar{b}})\tau_{\bar{b}} + x_{\bar{b}} - 2B(\tau_{\bar{b}})\sqrt{s}$, where parameter s is an additional relativistic correction term, and $B(\tau_b)$, $B(\tau_{\bar{b}})$ are normalization constants (for details, see equations in Section 2). By comparing the functional $V(\mu_1, \mu_2)$ obtained from the relativistic Green's function, Eq. (12) with the nonrelativistic formulation of the Feynman path integral in $4D$ nonrelativistic QM (NQM), we establish the definition of key parameters μ_1, μ_2 that are introduced in Section 3 as the constituent masses of bottom–antibottom quarks in the bottomonium highly resonant state. Next, we determine the NRC structure of the interaction potential in the Hamiltonian. The interaction between the constituent bottom–antibottom quarks with masses $\mu_b, \mu_{\bar{b}}$ is mediated by the exchange of gauge fields, where particles do not interact directly but rather exchange strong–field gauge bosons, resulting in the high–energy physics limit. Hence, the Green's function of the two–point correlation function can be written in momentum space in the form of

$$\widetilde{D}(q^2 + s^2) = \int d\eta\, \exp\big[-\eta\,(q^2 + s^2)\big]\,. \tag{36}$$

and using $\mathcal{D}(x)$ together with (4), then after integrating over dq, the functional of interaction terms with $x_0 \sim (\tau_b - \tau_{\bar{b}}) \rightarrow x_0 = \alpha(\tau_b - \tau_{\bar{b}})$ reads

$$V_{bb} = V'_{bb} + V''_{bb} = \frac{g^2}{2}\int_0^t\int_0^t d\tau_b d\tau_{\bar{b}} \\ \times \int_{-\infty}^{\infty}\frac{ds}{2\pi}\int_{-\infty}^{\infty}\frac{dq}{(2\pi)^3}\int_0^{\infty} d\eta\; e^{-\eta(q^2+s)} \\ \times \exp\Big[-i\,q\cdot\big(\bar{x}_b(\tau_b) - \bar{x}_b(\tau_{\bar{b}})\big)\Big] \\ \times \exp\Big[-is\,(\bar{x}_{0b}(\tau_b) - \bar{x}_{0b}(\tau_{\bar{b}})) + is\tau\Big]\,\Theta_{bb} \\ = \frac{g^2}{2}\int_0^t\int_0^t d\tau_b d\tau_{\bar{b}}\int_{-\infty}^{\infty}\frac{ds}{2\pi}\int_0^{\infty}\frac{d\eta}{8(\sqrt{\pi}\,\eta)^3}\; e^{-\frac{\bar{x}}{4\eta}+is\tau} \\ \times \sum_{k=0}^{\infty}\sum_{n=0}^{k}\frac{(-1)^{n+k}}{n!\,(k-n)!}\,\eta^n\,(x_0)^{k-n}\,(is)^{n+k}\,\Theta_{bb}, \tag{37}$$

$$V_{\bar{b}\bar{b}} = V'_{\bar{b}\bar{b}} + V''_{\bar{b}\bar{b}} = \frac{g^2}{2}\int_0^t\int_0^t d\tau_b d\tau_{\bar{b}} \\ \times \int_{-\infty}^{\infty}\frac{ds}{2\pi}\int_{-\infty}^{\infty}\frac{dq}{(2\pi)^3}\int_0^{\infty} d\eta\; e^{-\eta(q^2+s)} \\ \times \exp\Big[-i\,q\cdot\big(\bar{x}_{\bar{b}}(\tau_b) - \bar{x}_{\bar{b}}(\tau_{\bar{b}})\big)\Big] \\ \times \exp\Big[-is\,(\bar{x}_{0\bar{b}}(\tau_b) - \bar{x}_{0\bar{b}}(\tau_{\bar{b}})) + is\tau\Big]\,\Theta_{\bar{b}\bar{b}} \\ = \frac{g^2}{2}\int_0^t\int_0^t d\tau_b d\tau_{\bar{b}}\int_{-\infty}^{\infty}\frac{ds}{2\pi}\int_0^{\infty}\frac{d\eta}{8(\sqrt{\pi}\,\eta)^3}\; e^{-\frac{\bar{x}}{4\eta}+is\tau} \\ \times \sum_{k=0}^{\infty}\sum_{n=0}^{k}\frac{(-1)^{n+k}}{n!\,(k-n)!}\,\eta^n\,(x_0)^{k-n}\,(is)^{n+k}\,\Theta_{\bar{b}\bar{b}}, \tag{38}$$

$$V_{b\bar{b}} = V'_{b\bar{b}} + V''_{b\bar{b}} = \frac{g^2}{2}\int_0^t\int_0^t d\tau_b d\tau_{\bar{b}} \\ \times \int_{-\infty}^{\infty}\frac{ds}{2\pi}\int_{-\infty}^{\infty}\frac{dq}{(2\pi)^3}\int_0^{\infty} d\eta\; e^{-\eta(q^2+s)} \\ \times \exp\Big[-i\,q\cdot\big(\bar{x}_b(\tau_b) - \bar{x}_{\bar{b}}(\tau_{\bar{b}})\big)\Big] \\ \times \exp\Big[-is\,(\bar{x}_{0b}(\tau_b) - \bar{x}_{0\bar{b}}(\tau_{\bar{b}})) + is\tau\Big]\,\Theta_{\bar{b}\bar{b}} \\ = \frac{g^2}{2}\int_0^t\int_0^t d\tau_b d\tau_{\bar{b}}\int_{-\infty}^{\infty}\frac{ds}{2\pi}\int_0^{\infty}\frac{d\eta}{8(\sqrt{\pi}\,\eta)^3}\; e^{-\frac{\bar{x}}{4\eta}+is\tau} \\ \times \sum_{k=0}^{\infty}\sum_{n=0}^{k}\frac{(-1)^{n+k}}{n!\,(k-n)!}\,\eta^n\,(x_0)^{k-n}\,(is)^{n+k}\,\Theta_{b\bar{b}}, \tag{39}$$

where

$$\Theta_{bb} = 1 + n\big(\dot{\bar{x}}_b(\tau_b) - \dot{\bar{x}}_b(\tau'_b)\big) + \dot{\bar{x}}_b(\tau_b)\,\dot{\bar{x}}_b(\tau'_b), \tag{40}$$

$$\Theta_{\bar{b}\bar{b}} = 1 + n\big(\dot{\bar{x}}_{\bar{b}}(\tau_b) - \dot{\bar{x}}_{\bar{b}}(\tau'_b)\big) + \dot{\bar{x}}_{\bar{b}}(\tau_b)\,\dot{\bar{x}}_{\bar{b}}(\tau'_b), \tag{41}$$

$$\Theta_{b\bar{b}} = 1 + n\big(\dot{\bar{x}}_b(\tau_b) - \dot{\bar{x}}_{\bar{b}}(\tau'_b)\big) + \dot{\bar{x}}_b(\tau_b)\,\dot{\bar{x}}_{\bar{b}}(\tau'_b). \tag{42}$$

where $\tau = \tau_1 - \tau_2$ is the proper time of the relative motion of the constituent particles and includes velocity-dependent terms, which are common in relativistic treatments of interactions. Now, integrating over ds and $d\eta$ from Eqs (37)-(39) within the QCD formalism in the study of bottom–antibottom quarks, we define the diagonal interaction component V'_B as the one–gluon exchange effect that determines the mass renormalization coefficient arising from self–energy corrections $(V'_{bb} + V'_{\bar{b}\bar{b}})$ and the interaction term $(V'_{b\bar{b}})$ as follows

$$\begin{aligned}
V'_B &= V'_{bb} + V'_{\bar{b}\bar{b}} + V'_{b\bar{b}} \\
&= \left[\frac{g^2}{8\pi}\int_0^t\int_0^t d\tau_b d\tau'_b \, \frac{\delta(\tau_b - \tau_{\bar{b}})}{\left|\bar{x}_b(\tau_b) - \bar{x}_b(\tau_b)\right|}\right] \\
&\quad + \left[\frac{g^2}{8\pi}\int_0^t\int_0^t d\tau_{\bar{b}} d\tau_{\bar{b}} \, \frac{\delta(\tau_{\bar{b}} - \tau_{\bar{b}})}{\left|\bar{x}_{\bar{b}}(\tau_b) - \bar{x}_{\bar{b}}(\tau_{\bar{b}})\right|}\right] \\
&\quad + \left[-\frac{g^2}{4\pi}\int_0^t\int_0^t d\tau_b d\tau_{\bar{b}} \, \frac{\delta(\tau_b - \tau_{\bar{b}})}{\left|\bar{x}_b(\tau_b) - \bar{x}_{\bar{b}}(\tau_{\bar{b}})\right|}\right] \\
&= -\frac{g^2}{4\pi}\int_0^t d\tau \left[\frac{1}{\left|\bar{x}_b(\tau) - \bar{x}_{\bar{b}}(\tau)\right|} - \int \frac{dq}{q^2}\right]. \qquad (43)
\end{aligned}$$

and the second term of the functional interaction potential is $V''_B = V''_{bb} + V''_{\bar{b}\bar{b}} + V''_{b\bar{b}}$. To integrate this functional, we first consider the following conditions: (1) introduce an auxiliary variable ε, which is a mathematical tool to describe the motion of bottom–antibottom quarks in the center–of–mass coordinate frame $R(\tau)$, assumed to be at rest such that $\frac{dR(\tau)}{d\tau} = 0$, and (2) the speeds of relative motion of the bottom–antibottom quarks are

$$\begin{cases} v_b(\tau) = \dfrac{d\bar{x}_b}{d\tau} = \text{const}, \\ v_{\bar{b}}(\tau) = \dfrac{d\bar{x}_{\bar{b}}}{d\tau} = \text{const}, \end{cases} \qquad (44)$$

and the auxiliary variable ε shows the evolution of proper time $\tau \to \tau + \varepsilon$. By setting the auxiliary variable ε to $\varepsilon = 0$, and after integrating over the functionals V''_{bb}, $V''_{\bar{b}\bar{b}}$, and $V''_{b\bar{b}}$ while considering the center of mass in the form of

$$\begin{cases} R(\tau+\varepsilon) = \dfrac{\mu_{\bar{b}}}{\mu_b + \mu_{\bar{b}}} - \bar{x}_b(\tau+\varepsilon), \\ R(\tau) = \dfrac{\mu_b}{\mu_b + \mu_{\bar{b}}} - \bar{x}_{\bar{b}}(\tau). \end{cases} \qquad (45)$$

then, the second term of functional interactions potential is as follows

$$\begin{aligned}
V''_{bb} &= \frac{g^2}{8\pi}\int d\tau \sum_{k=1}^{\infty} \frac{(-1)^k}{k!} \\
&\quad \times \sum_{n=0}^{k} \frac{(-1)^n\, k!}{n!\,(k-n)!} \, \frac{1}{2^{2n}\sqrt{\pi}} \\
&\quad \times \int_0^{\infty} u\, du^{z-1} e^{-u} \, \frac{d^{\,k+n}}{d\tau^{\,k+n}} \Big[\left|\bar{x}_b(\tau+\varepsilon) - \bar{x}_b(\tau)\right|^{2n-1} \\
&\qquad \times \left(\bar{x}_{0b}(\tau+\varepsilon) - \bar{x}_{0b}(\tau)\right)^{k-n}\Big], \qquad (46)
\end{aligned}$$

$$\begin{aligned}
V''_{\bar{b}\bar{b}} &= \frac{g^2}{8\pi}\int d\tau \sum_{k=1}^{\infty} \frac{(-1)^k}{k!} \\
&\quad \times \sum_{n=0}^{k} \frac{(-1)^n\, k!}{n!\,(k-n)!} \, \frac{1}{2^{2n}\sqrt{\pi}} \\
&\quad \times \int_0^{\infty} u\, du^{z-1} e^{-u} \, \frac{d^{\,k+n}}{d\tau^{\,k+n}} \Big[\left|\bar{x}_{\bar{b}}(\tau+\varepsilon) - \bar{x}_{\bar{b}}(\tau)\right|^{2n-1} \\
&\qquad \times \left(\bar{x}_{0\bar{b}}(\tau+\varepsilon) - \bar{x}_{0\bar{b}}(\tau)\right)^{k-n}\Big], \qquad (47)
\end{aligned}$$

$$\begin{aligned}
V''_{b\bar{b}} &= \frac{g^2}{8\pi}\int d\tau \sum_{k=1}^{\infty} \frac{(-1)^k}{k!} \\
&\quad \times \sum_{n=0}^{k} \frac{(-1)^n\, k!}{n!\,(k-n)!} \, \frac{1}{2^{2n}\sqrt{\pi}} \\
&\quad \times \int_0^{\infty} u\, du^{z-1} e^{-u} \, \frac{d^{\,k+n}}{d\tau^{\,k+n}} \Big[\left|\bar{x}_b(\tau+\varepsilon) - \bar{x}_{\bar{b}}(\tau)\right|^{2n-1} \\
&\qquad \times \left(\bar{x}_{0b}(\tau+\varepsilon) - \bar{x}_{0\bar{b}}(\tau)\right)^{k-n}\Big]. \qquad (48)
\end{aligned}$$

In the context of mathematical physics in the series expansion matching formalism, when the Green's function (GF) is defined as a double sum over n and k, it is useful to consider the case $k = n$ to define only diagonal terms in the expansion. This technique is often applied in theoretical physics to simplify expressions. By focusing on the order $k = n$ and choosing the asymptotic behavior of the bottom–antibottom bound state at distance $|x| \to \infty$, and setting $\varepsilon = 0$, Eqs (46)-(48) are obtained, which show that the diagonal terms vanish, $V''_{bb} = V''_{\bar{b}\bar{b}} = 0$, while the cross term $V''_{b\bar{b}}$ of the second part of the interaction potential of bottom–antibottom quarks in the center–of–mass coordinate frame $R(\tau)$ has the following form

$$\begin{aligned}
V''_B &= -\frac{g^2}{4\pi} \sum_{k=1}^{\infty} \frac{(-1)^k}{k!} \, \frac{\Gamma\left(\frac{1}{2} - k\right)}{\pi^{1/2}\, 2^{2k}} \\
&\quad \times \int_0^t d\tau \, \frac{d^{2k}}{d\tau^{2k}} \Big[\left|\bar{x}_b(\tau) - \bar{x}_{\bar{b}}(\tau)\right|^{2k-1}\Big]. \qquad (49)
\end{aligned}$$

After integrating Eq. (49) over the parameter τ, which represents the proper–time relative motion of the constituent bottom–antibottom quarks in the bound state of the HRSB, we define

$$V''_B = -\frac{g^2}{4\pi} \sum_{k=1}^{\infty} \frac{(-1)^k}{\pi^{1/2}\,(2k)!} \, \frac{d^{2k}}{d\tau^{2k}} \left(|\bar{x}(\tau)|^{2k-1}\right), \qquad (50)$$

and then

$$V_B'' = -\frac{g^2}{4\pi}\,\mathcal{L}(\tau). \tag{51}$$

Now, to determine the standard form of the nonperturbative relativistic correction term $\mathcal{L}(\tau)$ of bottom–antibottom quarks in the HRSB, we define

$$\bar{\partial}_\mu(\tau) \;=\; \frac{d^{\,2k}}{d\tau^{\,2k}}\Big(|\bar{x}(\tau)|^{\,2k-1}\Big), \tag{52}$$

and consider that the relative velocity of particles is constant, namely $v(\tau) = \frac{|\dot{\bar{x}}(\tau)|}{d\tau}$ = const so that $\dot{v} = \frac{dv(\tau)}{d\tau} = 0$, and represent the velocity by the unit vector $n = \frac{\bar{x}(\tau)}{|\bar{x}(\tau)|}$ in the form of

$$v(\tau) = \frac{d\bar{x}(\tau)}{d\tau} \quad\longrightarrow\quad \frac{d|\bar{x}(\tau)|}{d\tau} = \frac{\bar{x}(\tau)}{|\bar{x}(\tau)|}\cdot\frac{d\bar{x}(\tau)}{d\tau} = n\,v. \tag{53}$$

On the other hand, we can use one of the canonical noncommutative relations in QM, which reflects the Heisenberg uncertainty principle of position and momentum, $[\bar{x}, p] = i$, and within this expression define a noncommutative relation $[\bar{x}, v]^2 = \hat{L}^2/|\bar{x}(\tau)|^3$. This notation is particularly interesting and useful in central potential problems under relativistic conditions, where the angular momentum $\hat{L}$ plays an important role. Now, one can define $\mathcal{L}(\tau)$ for the values $k = 1, 2, 3, \ldots$ as follows:

$$\begin{aligned}
k = 1 :&\quad \frac{d^2|\bar{x}(\tau)|}{d\tau^2} = \frac{[\bar{x}(\tau), v(\tau)]^2}{|\bar{x}(\tau)|^3} = \frac{\hat{L}^2}{|\bar{x}(\tau)|^3},\\
k = 2 :&\quad \frac{d^4|\bar{x}(\tau)|^3}{d\tau^4} = \frac{[\bar{x}(\tau), v(\tau)]^4}{|\bar{x}(\tau)|^5} = \frac{9\hat{L}^2}{|\bar{x}(\tau)|^5},\\
k = 3 :&\quad \frac{d^6|\bar{x}(\tau)|^5}{d\tau^6} = \frac{[\bar{x}(\tau), v(\tau)]^6}{|\bar{x}(\tau)|^7} = \frac{9.25\,\hat{L}^2}{|\bar{x}(\tau)|^5}. \quad \ldots
\end{aligned} \tag{54}$$

Then, for $k = n$, it reads

$$\begin{aligned}
\bar{\partial}(\tau)\Big|_{k=n} &= \frac{d^{\,2k}|\bar{x}(\tau)|^{\,2k-1}}{dk} = \frac{[\bar{x}(\tau), v(\tau)]^{2k}}{|\bar{x}(\tau)|^{2k+1}}\\
&= \frac{\left[\frac{(2k-1)!}{2^k(k-1)!}\right]^2\hat{L}^{2k}}{|\bar{x}(\tau)|^{2k+1}}.
\end{aligned} \tag{55}$$

To define the standard form of the NRC, some calculations and mathematical substitutions in Eq. (55) are required, and using

$$\begin{aligned}
\left[\frac{(2k-1)!}{2^{(k-1)}(k-1)!}\right]^2 &= \left[\frac{\Gamma(2k)}{2^{(k-1)}\Gamma(k)}\right]^2\\
&= \left[\frac{2^{(2k-1)}\,\Gamma(k+0.5)}{\pi^{1/2}\,2^{k-1}}\right]^2.
\end{aligned} \tag{56}$$

Then, we represent the new commutator form based on momentum and mass

$$m[\bar{x}, v] = [\bar{x}, p], \tag{57}$$

and consider the angular momentum operator's eigenvalue $\hat{L}^2 = \ell(\ell+1)$, then the canonical noncommutative relation $[\bar{x}, v]^2 = \hat{L}^2$ becomes

$$[\bar{x}, v]^2 \;=\; \frac{\ell(\ell+1)}{m^2\,|\bar{x}(\tau)|^3}. \tag{58}$$

Now, the standard form of the nonperturbative relativistic correction of the interaction potential in the HRSB as follows

$$\begin{aligned}
V_B'' &= -\frac{g^2}{4\pi}\,\mathcal{L}(\tau)\\
&= -\frac{g^2}{4\pi}\sum_{k=1}^{\infty}\frac{(-1)^k}{\pi^{1/2}(2k)!}\left[\frac{\Gamma(2k)}{2^k(k-1)\Gamma(k)}\right]^2\frac{\hat{L}^{2k}}{|\bar{x}(\tau)|^{2k+1}}\\
&= -\frac{g^2}{4\pi}\sum_{k=1}^{\infty}\frac{(-1)^k}{(2k)!}\left[\frac{2(2k-1)\Gamma(k+0.5)}{\pi^{1/2}\,2^k(k-1)!}\right]^2\frac{\hat{L}^{2k}}{|\bar{x}(\tau)|^{2k+1}}\\
&= -\frac{g^2}{4\pi}\sum_{k=1}^{\infty}\frac{(-1)^k}{k!}\,\frac{\Gamma(k+0.5)}{\pi^{1/2}|\bar{x}(\tau)|}\left(\frac{\hat{L}}{4\mu\,|\bar{x}(\tau)|}\right)^{2k}\\
&= -\frac{g^2}{4\pi}\sum_{k=1}^{\infty}\frac{(-1)^k}{k!}\,\frac{1}{\pi^{1/2}|\bar{x}(\tau)|}\left(\int_0^\infty du\,u^{k-1/2}e^{-u}\right)\\
&\qquad\times\left(\frac{\hat{L}}{4\mu\,|\bar{x}(\tau)|}\right)^{2k}.
\end{aligned} \tag{59}$$

After some mathematical simplification of the gamma integral function under $\left(\frac{\hat{L}}{4\mu|\bar{x}(\tau)|}\right)^{2k}$, Eq. (59) reads

$$
\begin{aligned}
V_B'' &= -\frac{g^2}{4\pi}\sum_{k=1}^{\infty}\frac{(-1)^k}{k!\,\pi^{1/2}\,|\bar{x}(\tau)|} \\
&\quad \times \left(\int_0^{\infty} du\, u^{k-1/2}e^{-u}\right)\left(\frac{\hat{L}}{4\mu|\bar{x}(\tau)|}\right)^{2k} \\
&= -\frac{g^2}{4\pi}\int_0^{\infty}\frac{1}{\pi^{1/2}\,|\bar{x}(\tau)|}\,u^{-1/2}e^{-u} \\
&\quad \times \left[\exp\left(-\frac{\hat{L}}{(4\mu|\bar{x}(\tau)|)}\right)^2 - 1\right]du. \qquad (60)
\end{aligned}
$$

using the exponential function, Taylor series, and properties under the operator formalism of the gamma integral function

$$
e^{-x\left(\frac{\hat{L}}{4\mu|\bar{x}(\tau)|}\right)^2} = \sum_{k=0}^{\infty}\frac{x^k}{k!}\left(\frac{\hat{L}}{4\mu|\bar{x}(\tau)|}\right)^{2k}, \qquad (61)
$$

and integral evaluation of the gamma function

$$
\int_0^{\infty} e^{-u}\,u^{1/2}\left(\frac{\hat{L}}{4\mu|\bar{x}(\tau)|}\right)^2 du = \frac{\pi^{1/2}}{\sqrt{\left(\frac{\hat{L}}{4\mu|\bar{x}(\tau)|}\right)^2}}. \qquad (62)
$$

we define

$$
V_B'' = -\frac{g^2}{4\pi^{\frac{3}{2}}|\bar{x}(\tau)|}\left(\frac{\pi^{1/2}}{\sqrt{1+\left(\frac{\hat{L}}{4\mu|\bar{x}(\tau)|}\right)^2}} - \pi^{1/2}\right). \qquad (63)
$$

and then, the nonperturbative relativistic correction term of the interaction is defined in the standard form

$$
V_B'' = -\frac{g^2}{4\pi|\bar{x}(\tau)|}\left(\frac{1}{\sqrt{1+\left(\frac{\hat{L}}{4\mu|\bar{x}(\tau)|}\right)^2}} - 1\right). \qquad (64)
$$

This term can be called the nonperturbative relativistic Hamiltonian of interaction, i.e., $H_{\text{nonpert.}} = V_B''$. At the end of the theoretical calculations presented above and the final result of Eq. (64), we derived NRC to the interaction potential of bottom–antibottom quarks in the HRSB bound state based on the relativistic nature of bottomonium behaviors when the bottom–antibottom quarks move relative to each other at $v(\tau) = \text{const}$. The NRC (V_B'') term to the Hamiltonian of interaction can be neglected in the nonrelativistic limit [27], and all spin interactions can be added to the total Hamiltonian [28, 29]. We present the asymptotic properties of the interaction of two scalar charged particles through PF using a variational technique.

4 Conclusion

In this theoretical research, the polarization correlation function of the highly resonant bound state of the bottom–antibottom quarks (bottomonium) was investigated, focusing on QFT and QM theories and the functional path integral formalism to define the relativistic correction on mass and on the interaction potential, which is considered a nonperturbative term of the total Hamiltonian. To characterize these corrections, we introduced a two-point polarization correlation function in the $4D$ Euclidean spacetime coordinate frame within the bottom–antibottom bound state. This formalism analytically describes the mass spectrum of the highly resonant bound state. The creation mechanism of the constituent mass of bottom–antibottom quarks forming the bound state was explained. The constituent masses of bottom–antibottom quarks differ from those of their free state masses. As is known, in the interaction gauge field the gluon acquires mass when it becomes part of a bound-state formation during the interaction of bottom–antibottom quarks with the background and external fields. Then, using the concept of proper time in $4D$ Euclidean spacetime coordinates, the relative motion of the constituent bottom–antibottom quarks was defined. Assuming that bottom–antibottom quarks move relative to each other, corrections to the interaction Hamiltonian associated with relativistic interaction were extracted from the functional integral part of the polarization correlation function. Both approaches consistently yield the relativistic corrections and behaviors that allow us to use the Schrödinger equation to determine the mass spectrum and energy eigenvalue of the highly resonant bound state. The calculation of relativistic corrections can be generalized for all hadronic and non-hadronic bound states. According to the approach presented in this paper, the computational results of the mass spectrum and constituent mass of the bottomonium highly resonant states, such as $\Upsilon(11020)$ with $m_b = 4.823$ GeV under the relativistic correction on mass [31], are defined as follows:

Table 1 Comparison of theoretical and experimental results for the highly resonant bottomonium state.

$M_{\text{cl.}}$	$M_{\text{rel.}}$	μ_b	M_{Th} [30]	M_{Exp} [31]
10.829	11.052	5.051	11.021	11.020

The calculation result based on this research includes the nonrelativistic mass ($M_{\mathrm{cl.}}$), the mass with the relativistic correction on mass ($M_{\mathrm{rel.}}$), and the constituent mass (μ_b). The results are acceptable in comparison with the nonrelativistic result, the experimental value, and the theoretical relativistic results obtained from other computational methods.

Acknowledgements The author would like to acknowledge the use of AI-assisted tools to improve the grammar and clarity of this manuscript. All intellectual content, computational results of relativistic corrections on the mass of the HRSB $10s$: $\Upsilon(11020)$ bound state, and conclusions are solely those of the author.

Funding
The theoretical research described here was supported by Foundation grant No. 380900-1404.

References

1. R. Brockmann, R. Machleidt, Phys. Rev. C **42**, (1990)
2. F. Coester, S. Pieper, F. Serduke, Phys. Rev. C **11**, (1975)
3. W. Glöckle, T.-S. H. Lee, Phys. Rev. C **33**, (1986)
4. R. Wiringa, Rev. Mod. Phys. **65**, (1993)
5. R. Brockmann, R. Machleidt, arXiv:nucl-th/9612004 (1996)
6. J. L. Forest, V. R. Pandharipande, A. Arriaga, Phys. Rev. C **60**, (1999)
7. J. L. Forest, V. R. Pandharipande, J. L. Friar, Phys. Rev. C **52**, (1995)
8. Y. L. Yang, P. W. Zhao, Phys. Lett. B **835**, (2022)
9. A. Akmal, V. R. Pandharipande, D. G. Ravenhall, Phys. Rev. C **58**, (1998)
10. Y. L. Yang, P. W. Zhao, arXiv:2405.04203 (2024)
11. J. Yoh, AIP Conf. Proc. **424**, 3 (1998)
12. A. Islam, N. Brambilla et al., arXiv:2503.22507 [hep-ph] (2025)
13. D. Asner, H. Atmacan et al., arXiv:2203.10203 [hep-ex] (2022)
14. N. Brambilla, S. Eidelman et al., Phys. Rep. **873**, (2020)
15. C. Bokade, Bhaghyesh, arXiv:2501.03147 [hep-ph] (2025)
16. Zh. Tang et al., arXiv:2502.09044 [nucl-th] (2025)
17. D. Fujiwara, *Rigorous Time Slicing Approach to Feynman Path Integrals*, 1st Ed. Springer, Berlin, Heidelberg, (2017)
18. J. Struckmeier, arXiv:2406.06530 [quant-ph] (2024)
19. G. Semenoff, *Quantum Field Theory*, 1st Ed. Springer, Berlin, Heidelberg, (2023)
20. M. Dienykhan et al., *Oscillator Representation in Quantum Physics*, 1st Ed. Springer, Berlin, Heidelberg, (1995)
21. W. Greiner, S. Schramm, W. Stein, *Quantum Chromodynamics*, 3rd Ed. Springer, Berlin, Heidelberg, (2007)
22. M. Dineykhan, G. V. Efimov, Kh. Namsrai, Int. J. Theor. Phys. **28**, (1989)
23. R. Gould, *Quantum Electrodynamics. Electromagnetic Processes*, 1st Ed. Springer, Berlin, Heidelberg, (2020)
24. S. Albeverio, R. Høegh-Krohn, S. Mazzucchi, *Mathematical Theory of Feynman Path Integrals*, 1st Ed. Springer, Berlin, Heidelberg, (2008)
25. E. Copson, *Asymptotic Expansions: The Saddle-point Method*, 1st Ed. Cambridge University Press, (2009)
26. K. Barley, J. Vega-Guzm, A. Ruffing, S. Suslov, UFNE Russian Academy of Sc. **65**, (2022)
27. Sabatucci, O. Benhar, A. Lovato, Phys. Rev. C **110**, (2024)
28. W. Lucha, F. Schoberl, Phys. Rep. **200**, (1991)
29. E. Eichten, F. Feinberg, Phys. Rev. D **23**, (1981)
30. A. Ahmadov, K. Abasova, M. Orucova, Adv. High Energy Phys. **2021**, (2021)
31. Particle Data Group, Prog. Theor. Exp. Phys. **2020**, (2020).

TTMP vol 2 (3), 2025
doi: 10.30511/TTMP.2025.2065630.1060

Transactions in Theoretical
and Mathematical Physics

On the coordinate representation in the Dirac bra–ket notation

Mehdi Jafari Matehkolaee[a,1]

[1]Department of Physics and Energy Engineering, Amirkabir University of Technology (Tehran Polytechnic), Hafez Avenue, Tehran, Iran

Received: 12 July 2025 / Accepted: 29 August 2025 / Published: 29 August 2025

Abstract In this paper we discuss some traps which can occur in using Dirac bra–ket notation in the coordinate (or momentum) representation. Furthermore, we demonstrate that in order to avoid some misconceptions, it is necessary to distinguish the two operators. First, the ordinary derivative d/dx, is just the usual partial differentiation which acts on the scalar function; and should not be considered as an operator which can act on the vectors in the Hilbert space. Second, the unbounded operator D_x, which is usually mixed up with the former. Our discussion indicates that the action of these two operators is the same on the bra $\langle x|$, but on the ket $|x\rangle$ it really leads to different results.

1 Introduction

Today, Dirac bra-ket notation is widely used in the literature of quantum mechanics. Anyone who ponders this notation will find that this mathematical formulation of quantum mechanics should not be thought of as being merely notation but, instead, as a major conceptual revolution [1]. However, using this notation can sometimes become confusing. For example, when dealing with antilinear operators, we must be careful in their use. As emphasized by Sakurai, Dirac bra–ket notation was invented to handle linear operators, not antilinear operators [2]. This subject is discussed in detail in Ref. [3]. In general, there are debates in Ref. [4]. Furthermore, challenges of this notation are pursued in pedagogical papers [5–7].

The eigenkets $|x\rangle$ of the position operator X satisfy

$$X|x\rangle = x\,|x\rangle, \tag{1}$$

where the value of x runs over all possible values of the position of the particle, that is, from $-\infty$ to $+\infty$. It should be noted that $|x\rangle$ is not in the Hilbert space because its norm is infinite. However, the vectors of the Hilbert space can be expanded in terms of the generalized kets $|x\rangle$.

The main problem starts when we want to know the action of the position operator on the derivative of $|x\rangle$, namely

$$X\,\frac{d}{dx}\,|x\rangle = \,? \tag{2}$$

First, we should emphasize that $\frac{d}{dx}$ is not a good designation for an operator acting on vectors in the Hilbert space. Instead, we can assign D_x as an operator in Hilbert space, defined by $(D_x f)(x) = f'(x)$, where $f'(x)$ denotes the derivative of the function $f(x)$. We endeavor to show that the distinction between these two operators is necessary, and that with this mathematical accuracy, some misconceptions and misleading notations will be eliminated.

In some quantum mechanics literature, misleading notations are seen, such as $\left[x,\, \frac{d}{dx}\right] f(x)$ and $\left[x,\, \frac{d}{dx}\right] |x\rangle$. We make a distinction between the position operator X and the real number x. Also, $f(x)$ is a number; in fact, f is a smooth and differentiable function and $f(x)$ is the value of the function f at the point x, so that $f(x)$ is a point (like x) itself. We begin with the following postulate, which plays a fundamental role in this paper.

Postulate 1. The action of the ordinary derivative d/dx on something independent of x is zero. It can be a function, vector, covector, etc.

From Ref. [2], in position space the wave function is represented by the action of the bra position on the ket state, that is, $\psi(x) = \langle x|\psi\rangle$. Obviously, $\psi(x)$ depends on x, while the abstract state $|\psi\rangle$ itself does not depend on x. Otherwise,

---

[a] e-mail: m.matehkolaee@aut.ac.ir

one could ask what is the value of $|\psi\rangle$ when x is, say, 8 or any other numbers?

Let $\psi(x) = N\exp\left[-a(x-b)^2\right]$, where a, b, and N are constants with $a > 0$. Obviously, the function $\psi(x)$ is not a constant function of x, but the abstract state $|\psi\rangle$ itself does not depend on x. In fact,

$$|\psi\rangle = \int_{-\infty}^{\infty} dy\, |y\rangle\langle y|\psi\rangle = \int_{-\infty}^{\infty} dy\, \psi(y)\, |y\rangle, \tag{3}$$

In Eq. (3), $|y\rangle$ is the normalized eigenvector of the position operator X with eigenvalue y, and there is no x appearing in this expression. Note that if $a \to \infty$, the wave function ψ tends to an eigenvector of the position operator X with eigenvalue b, i.e. $\lim_{a\to\infty}\psi = N'|b\rangle$, where N' is another normalization factor. Clearly, b does not depend on x either; therefore, $\frac{da}{dx} = \frac{db}{dx} = \frac{dN}{dx} = \cdots = \frac{d\psi}{dx} = 0$.

Postulate 2. The action of the ordinary derivative $\frac{d}{dx}$ on a ket vector such as $|x\rangle$ can be defined as

$$\frac{d}{dx}|x\rangle \equiv \lim_{h\to 0}\frac{|x+h\rangle - |x\rangle}{h}, \tag{4}$$

and for the bra position vector,

$$\frac{d}{dx}\langle x| \equiv \lim_{h\to 0}\frac{\langle x+h| - \langle x|}{h}, \tag{5}$$

where h is a constant number.

Now we can clarify the assignment in Eq. (2):

$$\begin{aligned} X\frac{d}{dx}|x\rangle &= X\lim_{h\to 0}\frac{|x+h\rangle - |x\rangle}{h} \\ &= \lim_{h\to 0}\frac{(x+h)|x+h\rangle - x|x\rangle}{h} \\ &= \frac{d}{dx}\left(X\,|x\rangle\right) = |x\rangle + x\,\frac{d}{dx}|x\rangle. \end{aligned} \tag{6}$$

It is obvious from Eq. (6) that $\left[\frac{d}{dx}, X\right]|x\rangle = |x\rangle \neq 0$. On the other hand, the last of the equations of (6) can also be obtained in an alternative way, as described in Appendix A.

Also, we can write

$$\begin{aligned} \frac{d}{dx}[f(x)] &= \left(\frac{d}{dx}\langle x|f\rangle\right) f(x) \\ &= \left(\frac{d}{dx}\langle x|\right)|f\rangle + \langle x|\left(\frac{d}{dx}|f\rangle\right). \end{aligned} \tag{7}$$

We should not simply move $\frac{d}{dx}$ through $\langle x|$, as $\langle x|$ depends on x and the first term in above relation is not zero. Clearly, in Eq. (7), the second term vanishes. So

$$f'(x) = \left(\frac{d}{dx}\langle x|\right)|f\rangle, \tag{8}$$

and this can be seen directly with respect to the postulate

$$\begin{aligned} \left\langle \frac{d}{dx}x \middle| f\right\rangle &= \lim_{h\to 0}\frac{\langle x+h|f\rangle - \langle x|f\rangle}{h} \\ &= \lim_{h\to 0}\frac{f(x+h) - f(x)}{h} = f'(x). \end{aligned} \tag{9}$$

Now, with the help of this postulate, we identify the distinction between two operators in a precise way.

2 Difference between D_x and d/dx

In this section, we indicate that $\frac{d}{dx}$ is only the usual partial differentiation which acts on functions, and not an operator on the vectors of the Hilbert space. A discussion about this distinction between the two operators can be found in Ref. [8].

At first, we can indicate the distinction between the two operators by the statement $\langle x|\hat{A}|\psi\rangle = A\langle x|\psi\rangle$, where $|\psi\rangle$ is an arbitrary state. In this relation $\hat{A}$ acts on kets while A acts on functions [9]. We do not use the hat symbol for operators in this paper.

For simplicity, we use the symbol d_x instead of $\frac{d}{dx}$. Assume that another operator D_x is defined by

$$\langle x|D_x|u\rangle = (d_x u)(x). \tag{10}$$

Eq. (10) represents the action of the operator D_x on the function u, and d_x means differentiation with respect to the variable x. To any vector $|u\rangle$ in the Hilbert space corresponds a function $u(x) = \langle x|u\rangle$, so one can write

$$\begin{aligned} \langle x|D_x|u\rangle &= \lim_{h\to 0}\frac{u(x+h) - u(x)}{h} \\ &= \lim_{h\to 0}\frac{\langle x+h|u\rangle - \langle x|u\rangle}{h} \\ &= \left(\lim_{h\to 0}\frac{\langle x+h\,| - \langle x|}{h}\right)|u\rangle. \end{aligned} \tag{11}$$

From the above equation we can conclude

$$\langle x|D_x = \lim_{h\to 0}\frac{\langle x{+}h| - \langle x|}{h}. \tag{12}$$

Therefore Eq. (12) gives the result

$$\langle x|D_x = \frac{d}{dx}\langle x|. \tag{13}$$

Now, one might be tempted to write this result as

$$D_x = \frac{d}{dx}. \tag{14}$$

We do not like this! And we think this is one of the misleading notations that happen in quantum mechanics literatures. Indeed, consider

$$\langle x|y\rangle = \delta(x-y), \tag{15}$$

then, using Eq. (10), it is shown that

$$\langle x|D_x|y\rangle = (d_{x1}\delta)(x-y). \tag{16}$$

where d_1 means differentiation with respect to the first variable, i.e. x. The reason we have used $dx1$ instead of d_x is that now there are two variables, x and y. The relation $\langle x|y\rangle = \delta(x-y)$ confirms Eq. (16), which can be written as follows:

$$\langle x|D_x|y\rangle = -(d_{x2}\delta)(x-y). \tag{17}$$

where d_{x2} denotes differentiation with respect to the second variable, i.e. y. So,

$$\begin{aligned}\langle x|D_x|y\rangle &= \lim_{h\to 0}\frac{\Delta(x, y-h) - \Delta(x, y)}{h}\\ &= \lim_{h\to 0}\frac{\langle x|y-h\rangle - \langle x|y\rangle}{h}\\ &= \langle x|\lim_{h\to 0}\frac{|y-h\rangle - |y\rangle}{h}.\end{aligned} \tag{18}$$

In the equation above, Δ is a two-variable function.

Now, we can conclude

$$D_x|x\rangle = -\frac{d}{dx}|x\rangle. \tag{19}$$

It is shown that Eq. (19) is not the same as Eq. (13). Also, it is simple to show that $\left[X, D_x\right]|x\rangle = -|x\rangle$. From Eq. (19), we immediately infer that, on the basis position vector $|x\rangle$, the action of the momentum operator becomes

$$P|x\rangle = -i\hbar D_x|x\rangle = i\hbar\frac{d|x\rangle}{dx}. \tag{20}$$

We can use the function notation

$$(Pf)(x) = -i\hbar f'(x), \tag{21}$$

where $f'(x)$ designates differentiation of $f(x)$. For the position operator X, with eigenvalue x, and using the definition Eq. (1), we obtain $[X, P]\,|x\rangle = i\hbar\,|x\rangle$, that is, the canonical commutation relation $[X, P] = i\hbar$.

In Ref. [2], considering the momentum operator as the generator of translations, the action of the momentum operator on an arbitrary vector independent of x, such as $|\alpha\rangle$, gives $P|\alpha\rangle = -i\hbar\int dx'\,|x'\rangle\,\frac{\partial}{\partial x'}\langle x'|\alpha\rangle$, and obviously choosing $|\alpha\rangle \equiv |x\rangle$ we immediately arrive at Eq. (20). From the formula for $P|\alpha\rangle$ we can write $\langle x'|P|\alpha\rangle = -i\hbar\frac{\partial}{\partial x'}\langle x'|\alpha\rangle$, so $\langle x'|P = -i\hbar\frac{\partial}{\partial x'}\langle x'|$. It is simple to show that $\left(\frac{\partial}{\partial x'}\langle x'|\right)^{\dagger} = \frac{\partial}{\partial x'}|x'\rangle$, and then the matrix elements of the momentum in the position representation are $\langle x'|P|x''\rangle = -i\hbar\frac{\partial}{\partial x'}\langle x'|x''\rangle = i\hbar\frac{\partial}{\partial x''}\langle x'|x''\rangle = i\hbar\left(\frac{\partial}{\partial x''}\langle x'\right)|x''\rangle = i\hbar\langle x'|\frac{\partial}{\partial x'}|x''\rangle$, since $\frac{\partial}{\partial x''}\langle x'| = 0$. Thus, we again arrive at the same Eq. (20), i.e. $P|x''\rangle = i\hbar\frac{\partial}{\partial x''}|x''\rangle$. Employing the operator D_x, we can deduce generalized momentum operators, and there is a detailed discussion of these operators in Ref. [10] and the references therein.

A generalized delta function can be defined as $\langle x|y\rangle = \dfrac{\delta(x-y)}{\sqrt{g(y)}}$ [11]. For brevity, we choose $f(y) = \dfrac{1}{\sqrt{g(y)}}$. Thus, with respect to our discussion, we can write

$$\begin{aligned}\langle x|D_x|y\rangle &= -f(y)\frac{\partial}{\partial y}\delta(x-y)\\ &= \langle x|\left[-f(y)\frac{\partial}{\partial y}\left(\tfrac{|y\rangle}{f(y)}\right)\right].\end{aligned} \tag{22}$$

As shown in Ref. [11], using $f(x)$ or $f(y)$ has no effect on the result. Applying D_x on the position state we obtain

$$|D_x|x\rangle = -f(x)\,\frac{d}{dy}\left(\tfrac{|x\rangle}{f(x)}\right). \tag{23}$$

Obviously, D_x is not an anti-Hermitian operator. According to Eq. (23), the adjoint of D_x takes the form

$$\langle x|D_x^\dagger = -\frac{d\langle x|}{dx} + \left(\frac{f'(x)}{f(x)}\right)\langle x|. \tag{24}$$

In this equation, we have used exactly the definition of the adjoint of a linear operator [12]. From Eq. (13), we know that $\langle x|D_x = \frac{d\langle x|}{dx}$, and hence we can write

$$D_x^\dagger = -D_x + \frac{f'(x)}{f(x)},. \tag{25}$$

where X is the position operator. Now, we can build an anti-Hermitian operator from D_x, which is obviously not anti-Hermitian. Suppose an operator O in which

$$O = \tfrac{1}{2}\left(D_x - D_x^\dagger\right). \tag{26}$$

Using Eq. (23) and taking into account the anti-Hermiticity of O, we obtain

$$\langle x|O = \frac{d\langle x|}{dx} - \frac{f'(x)}{2f(x)}\langle x|. \tag{27}$$

Now, by considering $f = \frac{1}{\sqrt{g}}$, Eq. (27) takes the form

$$\langle x|O = \frac{1}{\sqrt[4]{g(x)}}\frac{d}{dx}\left(\langle x|\sqrt[4]{g(x)}\right). \tag{28}$$

Therefore, the generalized momentum operator P is related to O via $P = -i\hbar O$. In Eq. (28), $g(x)$ is the metric of the generalized space under consideration.

Finally, we intend to examine the distinction between the two operators on the integral operator. Let us consider I as the integral operator, $I|x\rangle = \int_{-\infty}^{x}|y\rangle\,dy$, which is reminiscent of the inverse momentum operator (see Ref. [13] and references therein).

Now, we need to use the fundamental theorem of calculus. So we have

$$\frac{d}{dx}\left(\int_{-\infty}^{x}|y\rangle\,dy\right) = |x\rangle,. \tag{29}$$

and, by inserting D_x into the integral operator and using Eq. (19), we can obtain

$$D_x\left(\int_{-\infty}^{x}|y\rangle\,dy\right) = \int_{-\infty}^{x}D_x|y\rangle\,dy = -|x\rangle\,. \tag{30}$$

As can be seen, the results of the two cases are not the same. Note that Eq. (19) was used to obtain Eq. (30).

Here, in order to show the distinction more thoroughly, suppose $F(x) = \int_b^x |y\rangle\,dy$. Again, the fundamental theorem of calculus implies that $\frac{d}{dx}F(x) = |x\rangle$, but in the latter case we have $D_xF(x) = -(|x\rangle - |b\rangle)$. Thus, as can be seen, apart from the minus sign in Eq. (19), an additional term arises as well.

3 Conclusion

Eq. (19) shows a correct representation of the action of a differential operator in Hilbert space on the vector $|x\rangle$. From this result, the correct form of the action of the momentum operator on $|x\rangle$ is also obtained, $P|x\rangle = -i\hbar\frac{d}{dx}|x\rangle$.

We should stress the difference between the two operators. The operator $\frac{d}{dx}$ acts on anything that depends on x, whether it is a scalar, vector, etc., whereas D_x is an unbounded operator which acts on vectors and covectors in Hilbert space. Furthermore, statements such as $[x, \frac{d}{dx}]\,f(x)$ and $[x, \frac{d}{dx}]\,|x\rangle$ are misleading and should be avoided when dealing with Hilbert-space operators. It should also be noted that $[X, \frac{d}{dx}] = 0$, but $[X, D_x] = -1$, and in general $\frac{d}{dx}\left(x|x\rangle\right) = |x\rangle + x\frac{d}{dx}|x\rangle$, while $D_x(x|x\rangle) = xD_x|x\rangle = -x\frac{d|x\rangle}{dx}$, since D_x is a linear operator and Eq. (19) is used.

As an application of the discussion in this paper, and according to the distinction between these two operators, the generalized translation operator in curved space is obtained [14].

Appendix A

Another way to obtain Eq. (2) is by using the translation operator. Suppose

$$|x\rangle = e^{\frac{-iPx}{\hbar}}|x\rangle, \tag{A.1}$$

where P is the momentum operator and 0 is related to the position $x = 0$. Differentiating both sides of the above equation, we get

$$\frac{d}{dx}|x\rangle = -\frac{iP}{\hbar}\,|x\rangle, \tag{A.2}$$

that immediately implies Eq. (20).

Now one can write

$$X\frac{d}{dx}|x\rangle = -\frac{i}{\hbar}XP\,|x\rangle. \tag{A.3}$$

From the canonical commutation relation $[X, P] = i\hbar$, we have

$$X\frac{d}{dx}|x\rangle = -\frac{i}{\hbar}\left(i\hbar|x\rangle + PX|x\rangle\right) = -\frac{i}{\hbar}PX|x\rangle. \tag{A.4}$$

For the last term, we should note that P is a linear operator and we can write

$$PX|x\rangle = P\,x|x\rangle = x\,P|x\rangle = i\hbar x\frac{d|x\rangle}{dx}. \tag{A.5}$$

Therefore

$$X\frac{d}{dx}|x\rangle = |x\rangle + x\frac{d}{dx}|x\rangle. \tag{A.6}$$

For the commutation relations, consider in general $|\alpha\rangle$, so that $|\alpha\rangle = \int dy\, f(x, y)|y\rangle$, then it is clear that $X|\alpha\rangle = \int dy\, f(x, y)\, y|y\rangle$ and $\frac{d}{dx}|\alpha\rangle = \int dy\, \left[\frac{\partial}{\partial x} f(x, y)\right] |y\rangle$, so one can write

$$X\frac{d}{dx}|\alpha\rangle = \int dy\, \frac{\partial f(x, y)}{\partial x}\, y|y\rangle, \tag{A.7}$$

and

$$\frac{d}{dx}X|\alpha\rangle = \int dy\, \frac{\partial f(x, y)}{\partial x}\, y|y\rangle. \tag{A.8}$$

Obviously, the result is

$$\left[X, \tfrac{d}{dx}\right] = 0. \tag{A.9}$$

Again, using Ref. [2], we have $P|\alpha\rangle = \int dy\, \left(-i\hbar\frac{\partial}{\partial y}\langle y|\alpha\rangle\right) |y\rangle$. So

$$\begin{aligned} XP|\alpha\rangle &= \int dy\, \left(-i\hbar\tfrac{\partial}{\partial y}\langle y|\alpha\rangle\right) y|y\rangle \\ &= i\hbar \int dy\, \frac{\partial}{\partial y}\left(y\,|y\rangle\right)\langle\alpha|y\rangle, \end{aligned} \tag{A.10}$$

and

$$\begin{aligned} PX|\alpha\rangle &= \int P\,y|y\rangle\langle\alpha|y\rangle dy = \int yP|y\rangle\langle\alpha|y\rangle dy \\ &= \int y\langle\alpha|y\rangle dy(-i\hbar) \int \left[\frac{\partial}{\partial z}\langle z|y\rangle\right] |z\rangle dz \\ &= \int y\langle\alpha|y\rangle dy(\,i\hbar) \int \left[\frac{\partial}{\partial y}\langle z|y\rangle\right] |z\rangle dz \\ &= i\hbar \int \left[\frac{\partial}{\partial y}|y\rangle\right] y\langle\alpha|y\rangle dy. \end{aligned} \tag{A.11}$$

Therfore

$$[X, P]|\alpha\rangle = i\hbar\,|\alpha\rangle, \tag{A.12}$$

or

$$[X, P] = i\hbar, \tag{A.13}$$

References

1. B. E. Baaquie, *The Theoretical Foundations of Quantum Mechanics*, Springer, Berlin (2013)
2. J. J. Sakurai, *Modern Quantum Mechanics*, edited by San Fu Tuan, Benjamin/Cummings, Menlo Park, CA (1985)
3. A. Royer, Am. J. Phys. **62**, (1994)
4. F. Gieres, Rep. Prog. Phys. **63**, 2001
5. C. Singh and E. Marshman, Physics Education Research Conference (2013)
6. E. Marshman, C. Singh,Eur. J. Phys. **39**, (2018)
7. E. Marshman, C. Singh, Physics Education Research Conference (2020)
8. M. Jafari Matehkolaee, Tran. Theor. Math. Phys. **2**, (2025)
9. S. Konstantogiannis, Eur. J. Phys. Edu. **11**, (2020)
10. M. Jafari Matehkolaee, G. Rastegarzadeh,Pramana J. Phys. **95**, (2021)
11. B. S. DeWitt, T. Stanev, Phys. Rev. **85**, (1952)
12. M. Jafari Matehkolaee, Tran. Theor. Math. Phys. **1**, (2024)
13. M. Jafari Matehkolaee, Pramana J. Phys. **93** (2019)
14. M. Jafari Matehkolaee, Advances in Math. Phys., ID 2024, 1 (2024)